Analysis of pediatric corpulence and knee osteoarthritis using ultrawide-band (UWB) radar system

by

Kapil Gangwar

A thesis submitted in partial fulfillment of the requirements for the degree of

Master of Science

in

Electromagnetics and Microwaves

Department of Electrical and Computer Engineering
University of Alberta

Abstract

The ultra-wideband (UWB) radar technique has emerged as an efficient way to detect and image objects non-destructively. Widespread biomedical applications have allowed researchers across the globe to use this technique efficiently. Different tissues of the human body have different electrical properties, and UWB radar microwave systems have the potential to identify the tissue type when there is a considerable permittivity difference between them. Microwave tomography (MWT) has become the preferred imaging technique for biomedical applications to analyze functional and pathological of the tissues. Microwave imaging works best for high dielectric contrast regions such as bones and fatty areas. Recent progress in UWB radar technology and computing hardware has opened up unique opportunities for further research and development of MWT for biomedical and clinical applications. Safety is an essential feature of MWT imaging; this modality uses non-ionizing microwave pulses at average power levels comparable to cell phone radiation.

This thesis focuses on analyzing pediatric corpulence (child obesity) and knee osteoarthritis using UWB radar technologies. The first project discusses the UWB radar system and the genetic algorithm to analyze obesity in children by computing both complex permittivity and thickness of adipose tissue. This analysis involves the analytical study of electromagnetic wave interaction with human tissues. The simulation involves the analyses of the proposed technique on human voxel tissue models—including babies, children, and adults—available in CST software. The experimental validation involves the phantom consisting of a pork skin layer followed by pork fat, then ground pork which emulates muscle tissue. When the measured results were compared with

the actual permittivity and thickness, the accuracy of measurement data confirmed the suitability of this technique. Based on the electrical properties of adipose tissue, obesity levels were assessed. This technique is a safe, cost-effective, portable, ex vivo, non-contact method to determine the type of fat tissue in the human body and consequently to determine the level of obesity.

The second project discusses a non-invasive approach to studying knee osteoarthritis. This technique utilizes a combination of synthetic aperture radar (SAR) focused microwave reflection tomography, and genetic algorithm. This approach estimates osteoarthritis in a patient by analyzing three properties around the knee joint: the complex permittivity, the depth from the skin to the bone, and the gap between the thigh bone and shinbone. The technique is also applied to adult human voxel tissue knees and simplified knee models in the CST software. Simulated validation concludes that the technique is feasible as a safe, cost-effective, and non-contact method for estimating knee osteoarthritis in the human body.

Preface

This thesis is an original work by Kapil Gangwar. The Chapter 2 work was submitted to IEEE Transactions on Biomedical Engineering in December 2021, got a major revision in February 2022, and is submitted after thorough revision in April 2022. Ms. Fatemeh assisted me in measurements and collecting data. Chapter 3 work is under preparation and has to be submitted to IEEE Transactions on Medical Imaging. Mr. Robert has assisted me in developing imaging codes, and Ms. Fatemeh has helped me collect measurement data. I am responsible for initiating the works, designing, analyzing, and writing both manuscripts. My supervisor Prof. Rambabu Karumudi and I were involved in concept development and discussions of these projects to produce quality research work.

Acknowledgment

First of all, I thank God for allowing me to achieve one of my most important goals. It has been a long journey with many ups and downs, but I have been really fortunate to have the support and encouragement of those whom I would like to thank and appreciate.

I would like to express my gratitude to my master's thesis supervisor, Prof. Rambabu Karumudi. His boundless support, insight, tremendous knowledge, and guidance are the key to my success. Without his support and inspiration, I would not have completed my thesis on time. Besides his academic support, he has always encouraged me to go through difficult times, for which I will be eternally grateful. I am also thankful to my lab members, Adil, Robert, Fatemeh, Ferhad, and Dr. Feghi, for maintaining friendly support in the lab.

I sincerely thank my parents, Dharamveer Gangwar and Meena Gangwar, for love and care they have given me throughout my life. I also want to thank my brother Kunal Gangwar, my uncle Dr. K. G. Gangwar, other family members, and friends for their valuable support.

I would like to thank Prof. Ravi Kumar Gangwar, my undergraduate supervisor, who has always supported and inspired me in this research field.

Kapil Gangwar

Contents

List of Tables

List of figures

Chapter 1

Introduction

1.1 Motivation

Studying the injuries and causes of health issues through processes and techniques has become essential in medical research. X-ray, computed tomography (CT), magnetic resonance imaging (MRI), positron emission tomography (PET), and ultrasound imaging are some of the imaging tools used by doctors worldwide to diagnose or image various ailments and diseases. Imaging tools help practitioners to study the condition of the biological tissue as a first screening examination. This thesis focuses on analyzing two of the significant biomedical challenges facing the world: obesity and osteoarthritis. This study presents a new, safe, non-invasive, and cost-effective technique to determine a patient's obesity level and diagnose osteoarthritis of the knee.

Leptin and resistin play important roles in glucose metabolism and regulating child weight. The nutritional condition in the body controls their levels increased by feeding and reduced by fasting [1]. Adipose tissue produces a bioactive product known as Adipocytokine that includes

leptin as a metabolic regulator [2]. Leptin and resistin levels show a good correlation with anthropometric parameters of childhood obesity and its comorbidity. Hence, adipocytokines can be considered as a biomarker of childhood obesity [3]. A newborn baby generally has brown fat, which keeps the baby's body warm in cold weather. When the baby's age increases, some of the brown fat changes to white fat, resulting in a change in the electrical properties of the tissue. Recent studies show that in North America, many babies are born overweight, and doctors have become increasingly concerned about childhood obesity [4] [5] [6]. The method to diagnose the type of fat is a biopsy, which is an invasive procedure. Doctors have been looking for a non-invasive method to determine the type of fat underlying the skin tissue of newborn babies and children. Radar methods can measure the permittivity [7] [8] [9] [10] [11] and thickness of unknown adipose tissues, including white and brown fat, skin, and muscle properties. The White adipose tissue (WAT) and Brown adipose tissue (BAT) are present in different parts of the human body, but we are concentrating on the abdomen. The content of WAT and BAT in the abdomen area considerably correlates with the development of obesity [12] , and there is a considerable permittivity difference between these tissue types. The differences in white and brown tissue permittivity enable the microwave system to identify the tissue type.

For decades, osteoarthritis has also been a major cause of disability for many people. Stiffness, swelling, and pain are some of the symptoms of arthritis, leading to inactivity in daily life. Arthritis is caused by several factors: the breakdown of cartilage tissue, obesity, injuries, and overuse. It mainly occurs in people over 50 years old, but can be found in younger people. It happens when articular cartilage in the knee joint wears away and becomes rough and frayed. The gap between the thighbone and shinbone decreases, resulting in bone rubbing and painful bone spurs [13] [14] [15]. Current biomedical imaging tools analyze the tissue properties [16]

and assess their condition. CT scans, X-ray, radiographic testing, and MRIs are some of the present modalities used to examine the functional and pathological condition of knee diseases.

Microwave imaging has emerged as a potential technique for biomedical imaging applications because of its less complex system, lower radiation exposure, and non-invasive approach. These features have attracted researchers to develop microwave techniques to image biological tissues [17] [18] [19] [20] [21] [22] [23] . The measurements in the multi-frequency range offer a better reconstruction image than those in the narrowband systems [24] [25] [26]. Due to the high-water content in organic tissues, electromagnetic waves attenuate when they penetrate deeper into tissue [27], making backscattering (reflection) more viable than forward-scattering(transmission). UWB radar microwave imaging systems have been used effectively for biomedical imaging solutions [28] [29] [30] [31] [32] [33] [34] [35]. The UWB radar system has the advantages of being low cost, non-contact, and providing reasonable image resolution in the order of 5 mm in human tissue [36]. A typical UWB radar operates in the frequency range of 1 to 10 GHz.

Microwave imaging techniques can analyze the gap between the thigh bone and the shinbone. The dielectric profile of tissue around the knee changes when the patient suffers from osteoarthritis; when a ligament rupture occurs, synovial fluid [37] containing blood collects at the rupture site and begins to fill the entire knee joint causing effusion. The fluid has a high dielectric permittivity value of 84 and conductivity of 2.3 S/m [38]compared to the low dielectric permittivity of other knee tissues. This fluid leads to changes in the dielectric properties of the knee joint, and there is a significant permittivity difference that the UWB time-domain radar technique can analyze.

1.2 Ultrawide-band (UWB) Radar

UWB radar sends test signals with a wider spectral range than conventional radars. It requires much less pulse energy and makes the radar transmitter unrecognizable [39]. The transmitted signal is weaker than the allowable interference level of various electronic devices. Typically, pulse generators with very short pulse widths (shorter than one ns) are used. The spectrum of these pulses is more like white noise. However, UWB radar requires more receiver bandwidth than conventional radars.
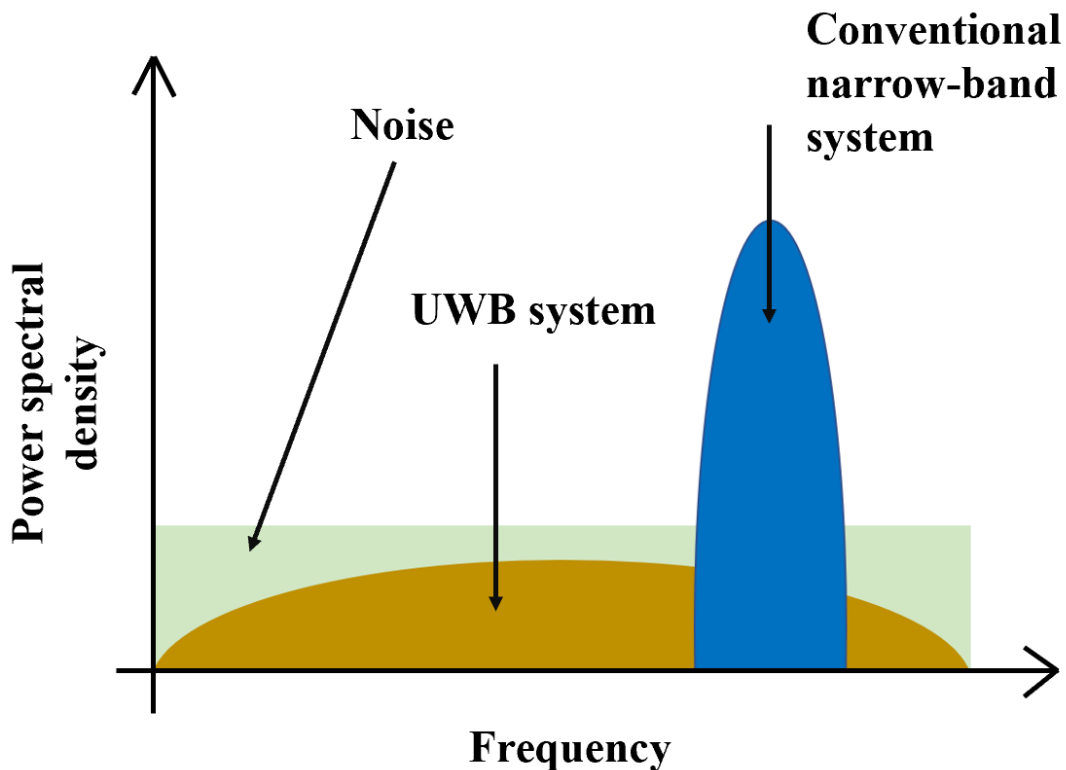
Figure 1. Comparison of power spectral density vs. frequency for the conventional narrow-band system, UWB system, and noise

The bandwidth of the ultra-wideband radar transmission signal is at least 25% of the transmitter's center frequency size. Thus, the minimum bandwidth of an ultra-wideband signal

whose center frequency is 5 GHz is 1.25 GHz. This wide bandwidth requires a broadband radar system, and the antenna used for this purpose must have a wideband characteristic. The typical antenna with wide bandwidth is usually Horn or Vivaldi antennas [40].

The UWB radar system features include low interference with other signals, greater spatial resolution, and lower power consumption. UWB radar has been used to detect humans [41], moving objects [42], imaging through-wall conditions [43], rescue operations [44], indoor positioning [45], and public security [46]. Recently, UWB radar technology has been used for various biomedical applications [47]. UWB radar imaging systems are promising for biomedical applications such as tumor detection [48] due to their decent penetration and high resolution. The principle of microwave detection of tumors is due to discrepancies in dielectric properties.

1.3   Microwave Tomography

Mainstream bio-imaging modalities include X-ray, CT, emission computed tomography (ECT), ultrasound, and MRI. PET uses radioactive material as a tracer for specific living tissue diagnosis by illuminating high concentration areas of a particular marker [49]. 3-T MRI produces the best resolution image in the order of millimetres. It is well suited for soft tissue imaging because of the high concentration of hydrogen molecules in the human body [50]. Although these techniques offer good image resolutions to study the condition of the human tissue, they have some disadvantages as well. The cost of diagnosis through MRI is high, and the patient has to stay for about an hour in the MRI tube for data acquisition [51]. In the ultrasound technique, the patient's body is in physical contact with the imaging probe [52]. PET is the most expensive modality where a tracer is injected into the human body, and after metabolic activity, the location of the disease is identified [53].

Microwave tomography (MWT) is a prominent imaging tool in the field of biomedical engineering. This imaging technique is good for high contrast dielectric regions in the human body, such as bones and dense fatty tissues. The technique can be used to evaluate breast, brain, cardiac, and lung cancer. Unlike continuous and prolonged exposure to X-rays which cause the human cell to ionize, MWT is a safe supplement for detecting pathological conditions of soft tissues. It is also a cost-effective and portable real-time imaging method. In MWT, transmitting antennas illuminate the electromagnetic wave on the subject, and the reflected wave is then measured using the receiving antennas. The received wave is then processed for image reconstruction.

Images received from the microwave tomography techniques provide instantaneous data on tissue properties for biomedical applications. Recently, the early detection of breast cancer using MWT has attracted the attention of researchers. Breast cancer detection, which is primarily based on microwave tomography, relies on significant dielectric characteristics between healthy and malignant tissues. In [54], X-ray mammography has been shown to have some drawbacks in terms of sensitivity and specificity. 5-15% of breast cancers are not visualized on mammography, and the average breast cancer yield per mammogram is 10% to 50%. These factors underscore the importance of additional imaging techniques for early detection of breast cancer.

Brain stroke is the third leading cause of death worldwide, after heart disease and all types of cancer. In case of brain stroke, clinical requests for the use of thrombolytic agents should be made within three hours of symptom onset and require reliable identification of ischemic stroke. This decision is based on imaging strategies similar to CT and MRI. Current CT, PET, and MRI imaging methods provide information about tissue characteristics associated with perfusion, ischemia, and heart attack. In order to convey clinical information, continuous CT scans or MRIs

of the head with perfusion and diffusion imaging are needed that repeatedly expose the patient to radiation and distinction agents [55]. MWT is a promising technique that exceeds traditional imaging modalities by providing non-invasive, real-time, safe, mobile, continuous, and efficient monitoring of human tissue. MWT is also an excellent complement to current imaging modalities for assessing perfusion-related brain injuries.

Since MWT benefits from short frame rates/time resolution, it is predicted that its use may offer a state-of-the-art evaluation of cardiac features and myocardial tissue viability. The best MWT imaging system should be (1) able to provide proper image resolution, (2) capable of locating more subtle less variations in tissue dielectric properties, (3) computationally robust, and (4) efficient in terms of image reconstruction with cost-effectiveness.

1.3.1 Synthetic aperture radar (SAR) focused reflection microwave tomography

Reflection tomography uses the sum of B-mode scan data to form a one-dimensional projection of an imaged object [56]. Fig. 2 shows a scenario for microwave reflection tomography measurements for a subject in the x-y plane. The receiver collects the reflected pulses from the object. The maximum distance between each transmitter and receiver position is controlled by the Nyquist sampling criteria for a particular signal bandwidth which gives the spatial pulse width of the pulsed broadband system. The pulse applied in this study has a pulse width of 100 ps and a normalized amplitude of 1 V, which leads to a spatial pulse width of 3 cm. An inter-spacing distance of 2 cm between the transmitter and receiver is used for the measurement setup. Similarly, the antenna pair is moved by 2 cm to the next location.

The reflections from the subject are collected at each location. After time alignment, all the receiver's data with respect to the reference position are added together to capture a 1D projection of the image scene. Similarly, multiple 1-dimensional projections are measured by rotating the antenna system at a predetermined step angle (in our case, by 20º). Then, as in CT scans, multiple these multiple 1D projection data are used for the reconstruction process.
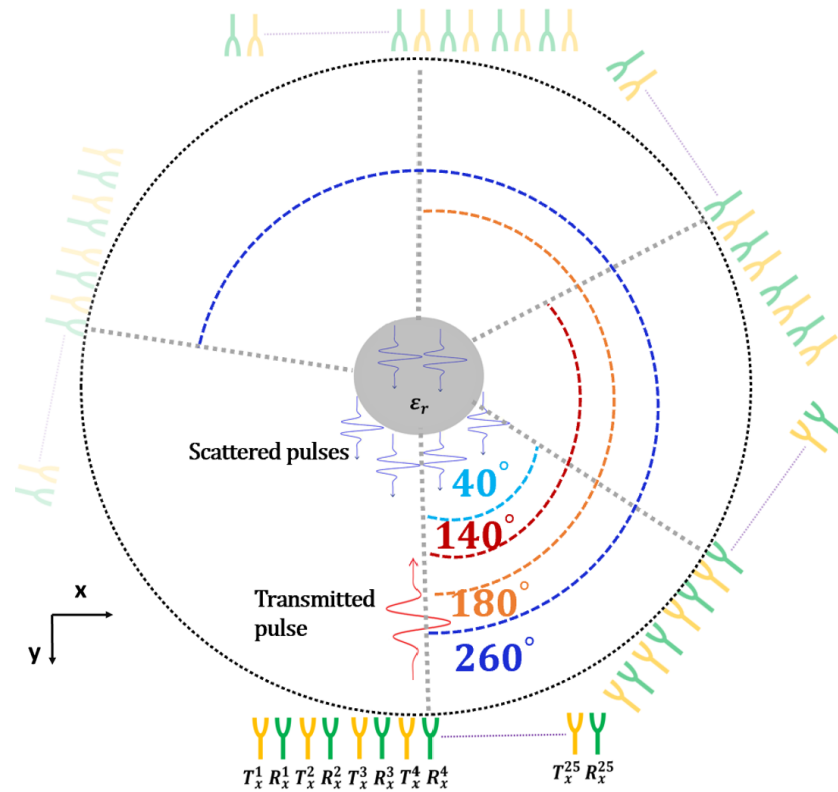
Figure 2. Setup diagram for SAR focused microwave tomography for a subject

The data is collected with a finite step (in our case, 20°) to cover a 360 ° scan space. The Nyquist criterion should also be satisfied for the maximum angle of rotation per step where the length of the circumferential arc due to the step angle must be shorter than the spatial pulse width of the system.
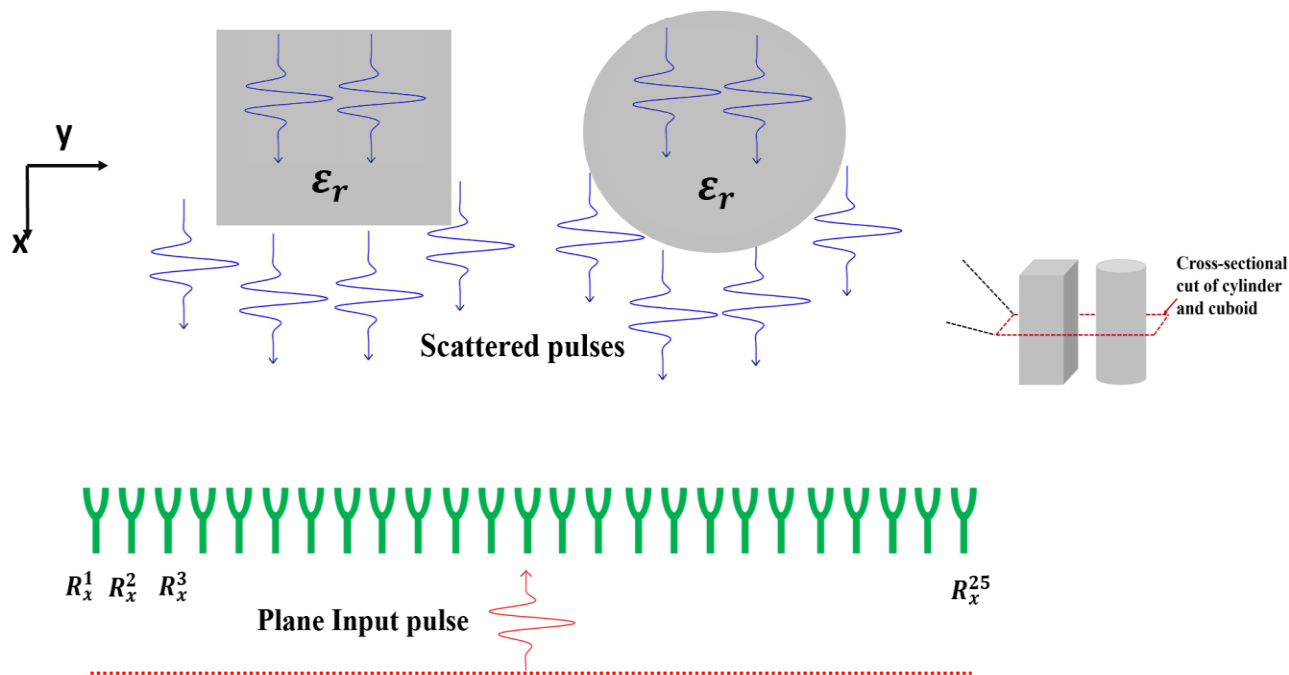
Figure 3. Setup diagram for SAR focused microwave tomography for a solid cylinder and cuboid

Fig.4 shows the reconstructed solid cylinder and cuboid cross-sectional image using SAR-focused reflection microwave tomography as set up in Fig.3. The scanned receiver data contains edge diffractions which are the scattered pulses from dimensional objects in the order of the spatial width of the pulses. The receiver's 1-D linear matrix arrangement (in the x-axis) and data (the relationship between space and time) are in accord with SAR processing. Therefore, we first perform SAR processing on the received data set for each projection angle to suppress the scattered noise.
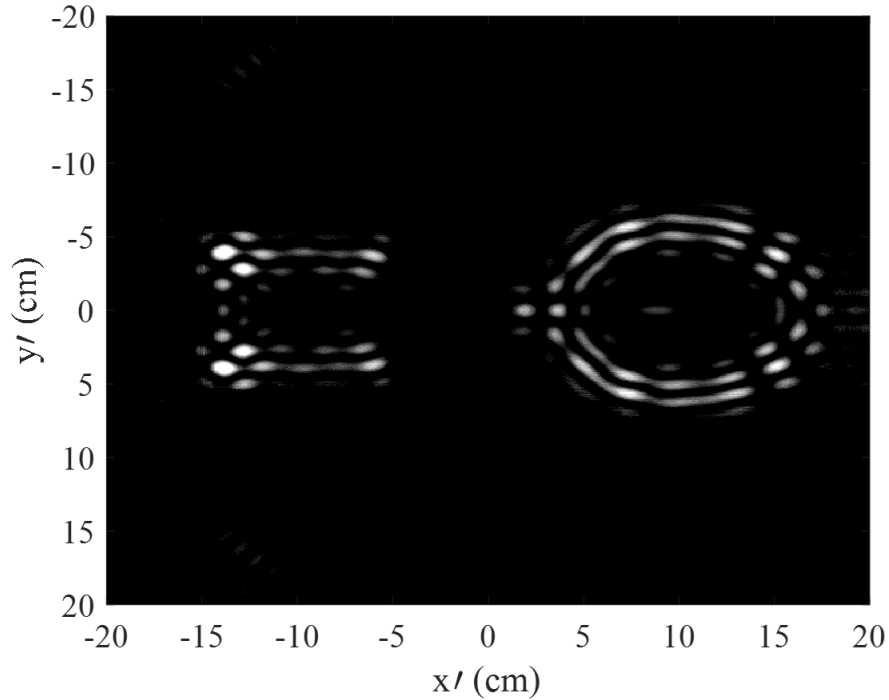
Figure 4. Solid cylinder and cuboid reconstruction using SAR focused reflection microwave tomography

The data collected by each receiver is in the form of a time-domain pulse. Each receiver collects the reflection caused by the incident waves from all 25 transmitter locations. The collected data is then summed up with proper time-shifting along the x-axis. The exact process is repeated for the remaining 24 receivers, and data is collected into a matrix. Finally, the SAR-focused data stored in a matrix is summed up to form a one-dimensional array forming the projection data at a specific angle. The projection angle is changed with the step size of 20° to obtain 18 projections, and for each projection a new receiver data set is recorded. After SAR focusing, the summation process is repeated for all step angles. The object scene is captured with edge diffraction minimized by SAR focusing based on the projection data. Finally, convolutional filtering/back-projection (an inverse radon transform) is performed to reconstruct the subject.

1.4   Contribution of this Thesis

The contributions of this thesis to the study of fat analysis and knee osteoarthritis are summarized as follows:

In Chapter 2:

An ex vivo method to estimate the dielectric properties and thickness of adipose tissue in the human body is presented. Based on the electrical properties of adipose tissue, obesity levels are assessed. This approach consists of two steps: 1) data acquisition by a UWB time-domain radar; and 2) genetic algorithm minimization (optimization) of the goal function, which is the absolute difference between the measured reflection coefficient and its corresponding theoretical value. The radar acquires the transient response of bio tissue. This study considered a three-layered tissue model to mimic the human abdomen's surface. The experimental phantom consisted of a pork skin layer followed by pork fat, then ground pork to emulate the muscle tissue. Three circular apertures of 2 cm, 3 cm, and 5 cm radiuses, respectively, were made on a metal shield to focus the measurements on a small area of interest. The measured results were compared with the actual permittivity and thickness of all animal models considered. The technique was also applied to human voxel tissue models, including babies, children, and adults, available in CST software. The UWB radar system and the genetic algorithm were used to determine both complex permittivity and thickness of adipose tissue to analyze obesity in children. The accuracy of measurement data confirmed the suitability of this technique. This technique is a safe, cost-effective, portable, ex

vivo, non-contact method to determine the type of fat tissue in the human body and determine the level of obesity.

In Chapter 3:

A non-invasive method to study knee osteoarthritis is presented. This technique consists of two steps: 1) a SAR focused microwave reflection tomography to image the knee joint, and 2) a UWB radar technique and genetic algorithm to obtain the muscle permittivity and gap between the thigh bone and shinbone. The osteoarthritis problem was assessed based on the combined results of knee joint images, change in muscle permittivity, and spacing between the thigh bone and shinbone. The technique was validated on simplified knee models followed by adult human voxel knee tissue available in the CST software. Simulated validation concluded that the technique is feasible as a safe and cost-effective method to estimate knee osteoarthritis in the human body.

Chapter 2

Analysis of pediatric corpulence via adipose tissue characterization

2.1 Introduction

A newborn baby has brown fat when they are born. This brown fat keeps the infant's body warm from the cold weather outside. When a child's age increases, brown fat changes its properties to white adipose tissue. Since many newborn babies are obese in Canada, doctors are looking for a device that can determine the obesity in babies to treat them accordingly. Doctors are looking for a non-invasive approach to determine the type of fat underlying the skin tissue of newborn babies as a substitute for costly and harmful biopsy methods. Several methods are proposed to study the properties of adipose tissue in the literature. In [57], mean subcutaneous fat thickness is measured using ultrasound technology. In-vivo and ex-vivo rat muscle and fat tissue in different hydration states were studied using an open-ended coaxial probe in the frequency range of 0.5 GHz-50GHz [58]. The technique estimates fat and muscle properties, but the prototype system should be in

contact with the subject. In [59], dielectric measurements on frozen and defrosted tissue were measured using an open-ended coaxial cable in the frequency range of 0.5GHz-8.5GHz. The technique is used for measuring chicken muscle, bovine liver, and bovine fat complex permittivity estimation using a contact approach. Recently in [60], abdominal fat thickness measurement was done with a high dielectric material-filled horn antenna using a reflection coefficient response. The measurement is performed in the frequency range of 1.7GHz-8GHz using an open-ended contact probe. Table 1 summarizes the available state-of-the-art techniques used for skin, fat, or muscle complex permittivity or thickness measurement. Magnetic resonance imaging (MRI), Ultrasound, and computerized resonance imaging (CTS) are expensive methods to evaluate the properties of skin, fat, and muscle; hence, UWB radar techniques are of growing interest among researchers for non-contact measurements.

The UWB radar technique has emerged as an efficient way to detect and scan objects noninvasively. Different tissues of the human body have different electrical properties [61]. In general, the permittivity of an object can be determined by using various techniques such as the cavity perturbation technique [62] [63], tetrapolar impedance [64] [65], the transmission line method [66] [67], the open-ended probe technique [68] [69] [70] and, the microstrip ring resonator method [71] [72]. The cavity perturbation method is an invasive procedure and ex-vivo technique that measures the sample's complex permittivity due to the change in resonant frequency and quality factor when placed at the center of the cavity. Moreover, the preparation of some samples is quite tricky; this method is not valid for liquids and provides data only at a single frequency [62] [63]. The tetrapolar permittivity measurement technique utilizes a four-electrode system inoculated in the tissue, and a potential difference between the electrodes is measured. Electrode configuration varies according to the tissue [64] [65]. An invasive contact transmission line

technique is unsuitable for in-vivo and ex-vivo measurements for solid biological samples [66] [67].

Table 1. Techniques to measure tissue properties

Reference	Contact/ contactless	Technique	Measurements
[57]	Contact	Ultrasound	Fat thickness
[58]	Contact	Open-ended probe	Fat and muscle properties
[59]	Contact	Open-ended probe	Skin complex permittivity
[60]	Contact	Open-ended probe	Abdominal fat thickness
Present	Contactless	Free space	Skin, fat, and muscle thickness and dielectric properties

The open-ended coaxial probe is a non-invasive contact technique that needs the elimination of air voids between the coaxial probe and the material under test (MUT) for accurate results [68] [69] [70]. Another method to measure permittivity is the microstrip ring resonator, a non-destructive contact and ex-vivo method suitable for low and high dielectrics. This method has limitations in measuring liquids, powders, and very lossy materials [71] [72].

This chapter discusses a free-space technique, non-invasive, contactless, and ex-vivo method to measure the content of white/brown adipose tissue in the abdomen area. The measurements considerably correlate with the development of obesity [73]. The proposed technique uses a multi-transmission line model to represent the human body and the genetic algorithm for measurements. The UWB radar system with two antennas measures the multilayer tissue's transit time response. The methodology for the ideal Gaussian pulse radiation to determine the thickness of the skin layer is mathematically illustrated in the following sections.

The proposed analysis is carried out on pork tissue samples that impersonate the properties of the human tissue. The experimentally generated 100 ps Gaussian pulse is used in the simulation setup for analyzing the pork tissue sample, human abdomen, and human voxel tissues of babies, children, and adults in ideal conditions. The estimation of skin, fat, and muscle properties is discussed with the respective percentage error. The evaluation of the specific absorption ratio (SAR) to examine the safety of radiation exposure on tissue properties is also discussed.

Further, the technique is tested in the laboratory on some animal tissues: pork, beef, chicken, and turkey. As electrical properties of the tissue vary with the temperature and the place [74], the animal tissues' electrical properties are first measured using an E8362B PNA network analyzer and Agilent's 85070E dielectric probe kit for reference purposes. Then, the thickness and complex permittivity of skin, fat, and muscle layers of pork, beef, chicken, and turkey in the frequency range of 5GHz–10GHz are measured using the proposed technique.

This chapter is arranged as follows. Human tissue properties are discussed in section 2.2. The proposed technique and methodology to determine the skin thickness are investigated and presented in section 2.3. Section 2.4 illustrates simulation setups for pork and human babies, children, and adults. Section 2.5 shows the average SAR calculation for all human models, section 2.6 the results, and section 2.7 the conclusions.

2.2 Tissue properties

2.2.1 Skin

The epidermis and dermis are the primary layers of the skin [75]. The thickness of the epidermis was estimated at around 80-100 µm. The water content increases linearly with a depth to a

maximum of 70% at 0.2 mm. The typical thickness of the dermis layer was estimated to be around 1-2 mm [76] [77] [78]. Using various techniques, researchers have measured the skin permittivity in the frequency range of 1 kHz-100 GHz. The properties of pork tissue are discussed in many works that mimic the human tissue properties. The average permittivity, conductivity, and thickness of the combined epidermis and dermis layer of the abdomen for humans and pork tissue in the frequency range of 5-10GHz are summarized in Table 2 [79] [80].

Table 2. Abdomen skin properties of human and pork tissue

Description	Average permittivity	Average conductivity	Thickness(mm)
Human	34.5	0.35	2.22 $\pm$0.34
Pork	33	0.86	2.20 $\pm$0.43

2.2.2 Fat

The layer followed by the skin is adipose tissue [81]. In mammals, adipose tissue plays an essential role in providing day-to-day energy expenditure. White and brown fat are the two adipose tissues mainly found in the human body [82]. White adipose tissue is mainly responsible for energy storage, whereas brown adipose tissue generates heat and metabolizes fat [80] [83] [84] [85] [86]. Table 3 outlines the average permittivity, conductivity, and thickness of brown and white fat of human and pork abdominal tissue (brown fat) in the 5-10GHz range.

Table 3. Abdomen fat tissue properties human and pork tissue

Description	Average permittivity	Average conductivity	Thickness(mm)
Human Brown fat	8.21	0.422	11.16$\pm$04.13

Human White fat	4.8	0.232	11.08±03.11
Pork (brown fat)	8.05	0.25	9.70±03.50

2.2.3 Muscle

The abdomen muscular tissues are comprised of transverse abdominis, external oblique, internal oblique, and rectus abdominis. These muscles together give stability to perpetuate correct posture, which lies beneath abdominal skin, followed by fat tissue.

Table 4. Abdomen muscle properties of human and pork tissue

Description	Average permittivity	Average conductivity	Thickness(mm)
Human	39.15	0.454	7.08±03.34
Pork	41.3	1.2	2.20 ±0.43

In [87], the real-time ultrasound imaging method is used to determine the thickness of the right and left sides of the internal oblique, external oblique, transverse abdominis, and rectus abdominis muscles. The average permittivity, average conductivity, and thickness of abdomen muscle for human and pork tissue in the frequency range of 5-10GHz are discussed in Table 4 [87] [88].

2.3 Tissue dielectric and thickness measurement technique

Before testing the proposed technique on different tissues, the complex permittivity of each sample is first measured in the lab using a coaxial probe connected to a vector network analyzer. Each sample permittivity is recorded in the frequency range of 1GHz-10 GHz and is used to compare the result obtained by the proposed technique.
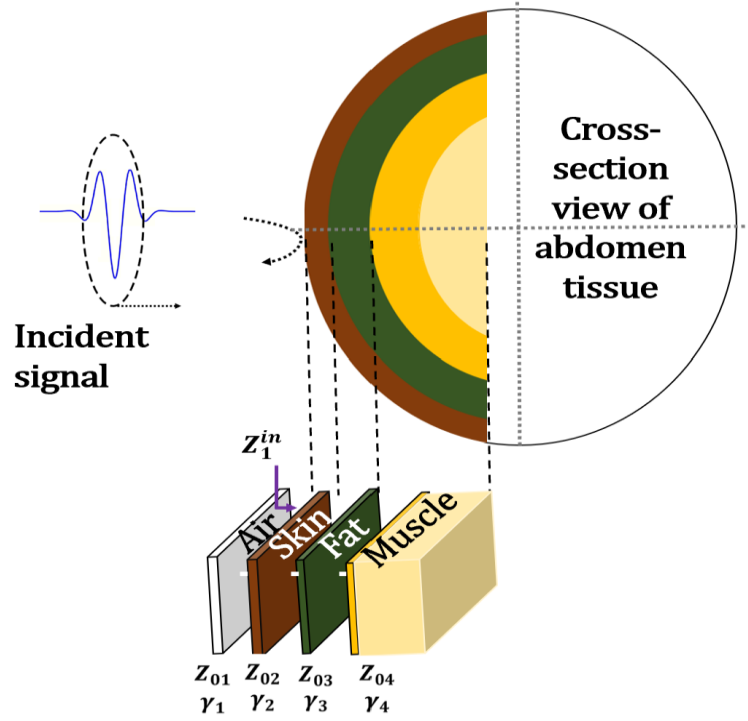
Figure 5. Abdomen tissue as a multi-section transmission line

The abdomen tissue can be considered as a multi-section transmission line, as shown in Fig.5. The theoretical input impedance of the n-layer tissue can be calculated as follows:

$$Z_n^{in} = Z_{0n+1} \frac{Z_{n+1}^{in} + Z_{0n+1}.tanh(\gamma_{n+1} d_{n+1})}{Z_{0n+1} + Z_{n+1}^{in}.tanh(\gamma_{n+1} d_{n+1})} \tag{2.1}$$

$$\gamma_n = j \frac{2\pi f \sqrt{\varepsilon_{rn}}}{c} \tag{2.2}$$

$$Z_{0n} = \frac{\eta_0}{\sqrt{\varepsilon_{rn}}} = \frac{377}{\sqrt{\varepsilon_{rn}}} \tag{2.3}$$

where Z_{n-1}^{in} is the input impedance of the nth layer of the transmission line. γ_n, d, Z_{0n} and ε_{ri} are the propagation constant, length, characteristic impedance, and the complex permittivity of the layer n, respectively, whereas c, and η_0 are the speed of light in a vacuum and the intrinsic

wave impedance of free space, respectively. The complex reflection coefficient of the three-layer tissue is a function of the input impedance, i.e., Z_1^{in}:

$$\Gamma_t = \frac{Z_1^{in} - Z_{01}}{Z_1^{in} + Z_{01}} \qquad (2.4)$$

where Z_{01} is the characteristic impedance of the air. The input impedance can be calculated as follows:

$$Z_1^{in} = Z_{02} \frac{Z_2^{in} + Z_{02} \tanh(\gamma_2 d_2)}{Z_{02} + Z_2^{in} \tanh(\gamma_2 d_2)} \qquad (2.5)$$

$$Z_2^{in} = Z_{03} \frac{Z_3^{in} + Z_{03} \tanh(\gamma_3 d_3)}{Z_{03} + Z_3^{in} \tanh(\gamma_3 d_3)} \qquad (2.6)$$

$$Z_3^{in} = Z_{04} = \frac{377}{\sqrt{\varepsilon_{r4}}} \qquad (2.7)$$

The objective is to minimize the absolute difference between the measured frequency-dependent reflection coefficient and its corresponding theoretical value [89]. The minimization problem is defined as follows:

$$M_0 = min\{||\Gamma_t(X)| - |\Gamma_m||\} \qquad (2.8)$$

From Eq. (2.4), the complex reflection coefficient is a function of Z_1^{in}, which is a function of $d_2, \varepsilon_2, d_3, \varepsilon_3, \varepsilon_4$. Here, d_2 and d_3 are the thickness of skin and fat tissue layer, respectively whereas $\varepsilon_2, \varepsilon_3$ and ε_4 are the complex permittivity of skin, fat, and muscle tissue layer, respectively. Hence, unknown vector X consists of the following unknowns to be found:

$$X = [d_2, \varepsilon_2, d_3, \varepsilon_3, \varepsilon_4] \qquad (2.9)$$

where three signals are measured, and two calibrations extract the measured reflection coefficient. One signal is the reflected signal by the multi-layer tissue, while another is the

reflection from the metal sheet placed on the same multi-layer tissue. The third signal is the ambient signal due to the antenna coupling and outside environment recorded without any target. Then the measured signals are calibrated by subtracting the ambient signals from them.

After the measured and theoretical reflection coefficients are achieved, a genetic algorithm is applied to minimize their difference. A genetic algorithm with a maximum generation of 8000, a migration rate of 10%, a cross-over rate of 50%, and a population size of 300 is applied to minimize possible solutions. This minimization problem is performed for all the valid frequency data (5-10 GHz). Binary encoding of all the five unknowns is accounted for during the process. The set of all the combinations of five unknowns makes the generation 0. Then, natural selection and simulation of the survival of fitness function X are made to determine the solution. This process is repeated till M_0 is minimized. In order to calculate the thickness and complex permittivity, the extracted values over the frequency span are averaged, and the results are summarized in the tables discussed in later sections.

2.4 Simulation setups

2.4.1 Methodology to determine tissue thickness

A mathematical analysis is carried out in this section to obtain the permittivity and thickness of the skin in the human body. First, a cuboidal box of dimension 300 x 300 x 20 mm^3 is assigned with the skin permittivity value of 37. Another cuboidal box is placed adjacent to the skin layer with the same length and width but with a thickness of 300 mm and permittivity of 8 to mimic brown fat. A Gaussian pulse of 100 ps pulse width is radiated onto the combined layers of skin

and fat, as shown in Fig.6. The reflection from the skin-air interface is recorded by voltage probe 1, as shown in Fig.6, and probe 2 records the reflected pulse coming from the skin-fat layer interface. However, the same pulse traveled into the air through the skin layer and was recorded again by probe 1. Fig.7 shows the merged recorded pulse from the air-skin layer interface $S_1(t)$ and skin-fat layer interface reflection $S_2(t)$ when the skin thickness is 20 mm. In the graph, the red signal enclosed in light brown color space corresponds to $S_1(t)$, while the signal, which appears after 1.5 ns, enclosed in the light green color space, is designated as $S_2(t)$.
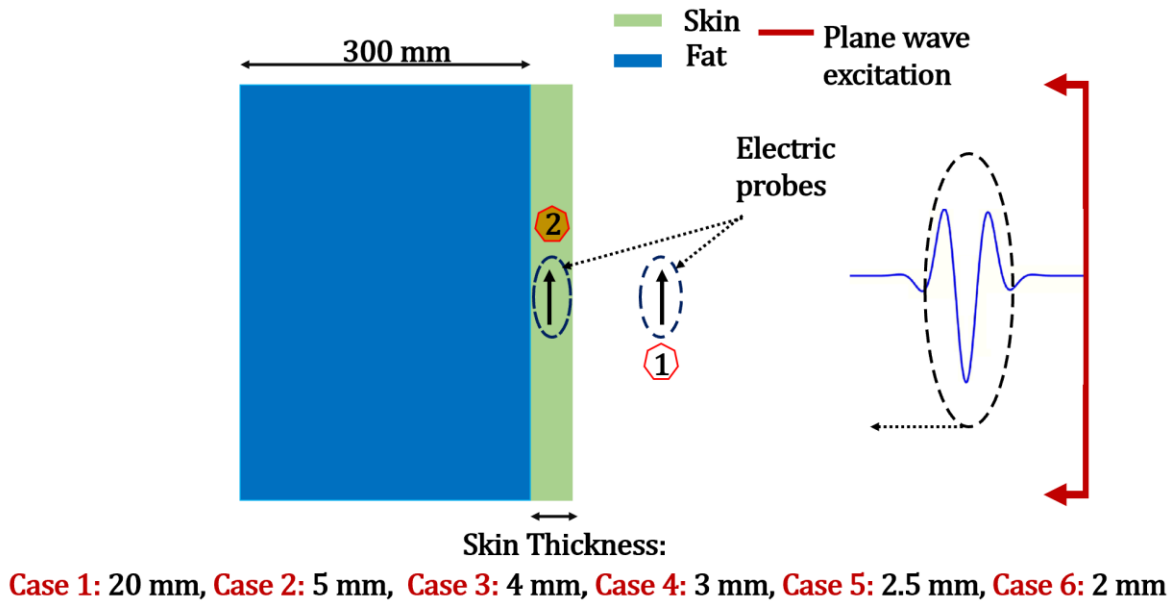
Figure 6. Simulation setup of a skin-fat layer with plane wave excitation
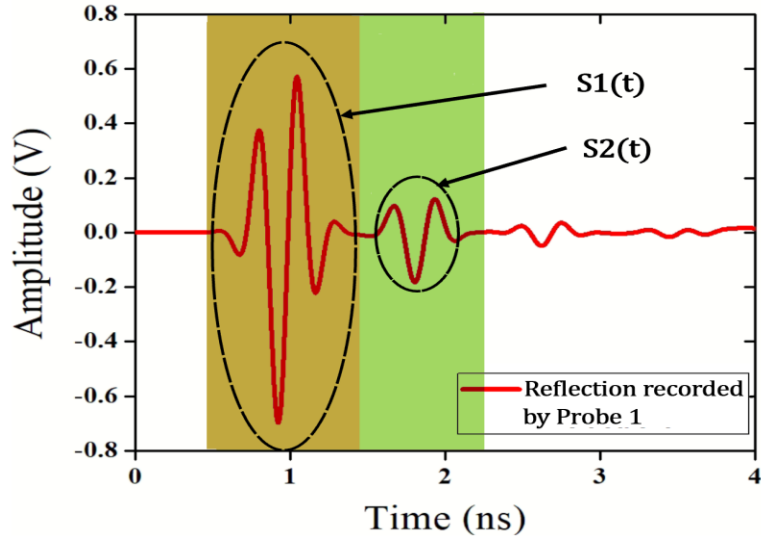
Figure 7. Recorded pulse by voltage probe 1 after reflection from air-skin layer and skin-fat layer interface (skin thickness 20 mm)

Other setups, as shown in Fig.6 with various thicknesses of the skin layer (i.e., 5mm, 4mm, 3mm, 2.5mm, 2mm), are simulated, and in each case, the pulse was recorded by probe 1. Since the thickness of the skin was very small, it was observed that the reflection from the air-skin interface and skin-fat interface merged up to a single pulse.
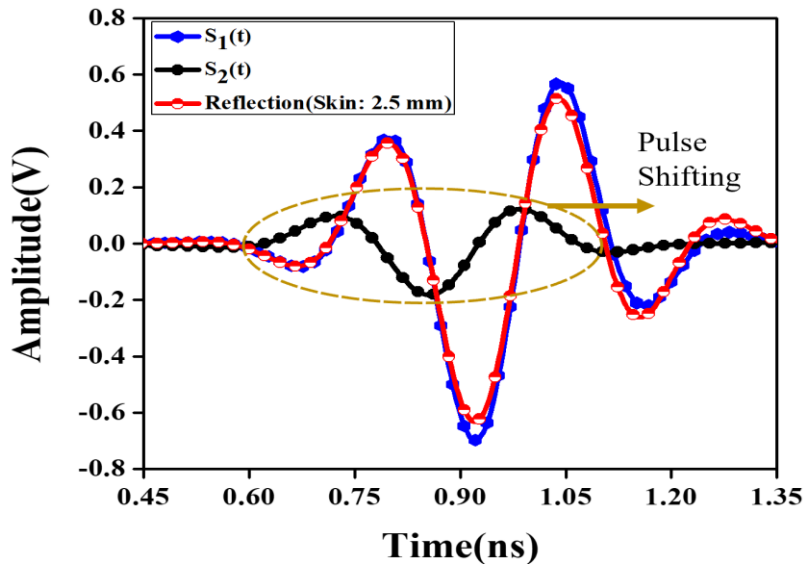
Figure 8. Pulse S1(t) (solid blue line), S2(t) (solid black line), and merged pulse y1(t) (solid red line) recorded by probe 1 in case of 2.5 mm skin layer thickness

For separating the merged pulses, intrinsic pulses $S_1(t)$ and $S_2(t)$ are recorded from the 20 mm skin thickness experiment. Fig.8 shows the $S_1(t)$ (solid blue line) and $S_2(t)$ (solid black line) obtained from the 20 mm skin thickness case, and the merged recorded pulse $y_1(t)$ (solid red line) for the case of 2.5 mm skin thickness. It is known that $y_1(t)$ is a combination of $S_1(t)$ and $S_2(t)$ with an unknown time interval that depends on the skin layer thickness (d).

$$\tau = d/c \tag{2.10}$$

$$c = c_o/\sqrt{\varepsilon} \tag{2.11}$$

where τ is defined as the total time the signal takes to pass through the skin layer into the air, d is the estimated skin thickness, and c is the speed of light in the skin medium.
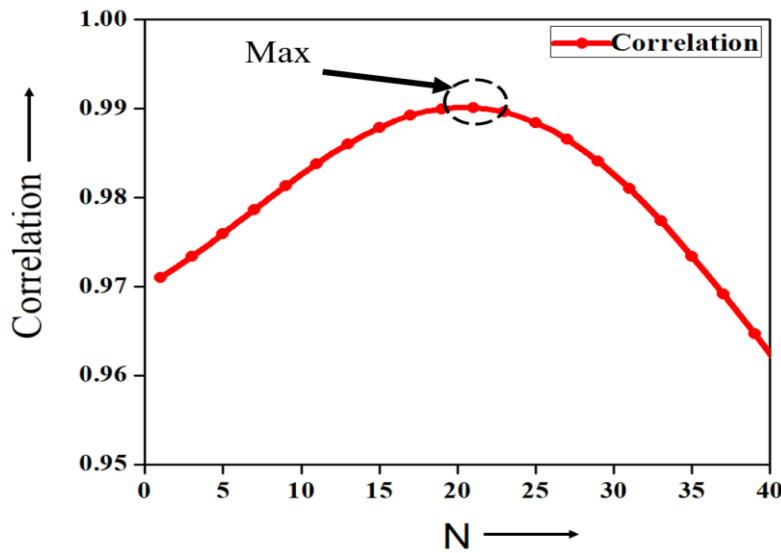
Figure 9. Correlation curve with respect to 'n' time intervals (2.5 mm skin layer thickness)

c_o is the speed of light in air, and ε is the dielectric permittivity of skin. To estimate the skin thickness, first, we need to write $y_1(t)$ as a sum of $S_1(t)$ and time-shifted $S_2(t)$. Now, the $S_2(t)$ is

shifted by n times in the right direction, as shown in Fig.8 with the time interval $\partial\tau$, equivalent to 2.727 picoseconds derived from the recorded signal. The $\partial\tau$ is the same for all three signals obtained from the simulation setups. The resultant signals $y(t)$ attained after shifting $S_2(t)$ can be given as follows:

$$y(t) = S_1(t) + S_2(t-\tau) \tag{2.12}$$

$$\tau = n\,\partial\tau \tag{2.13}$$
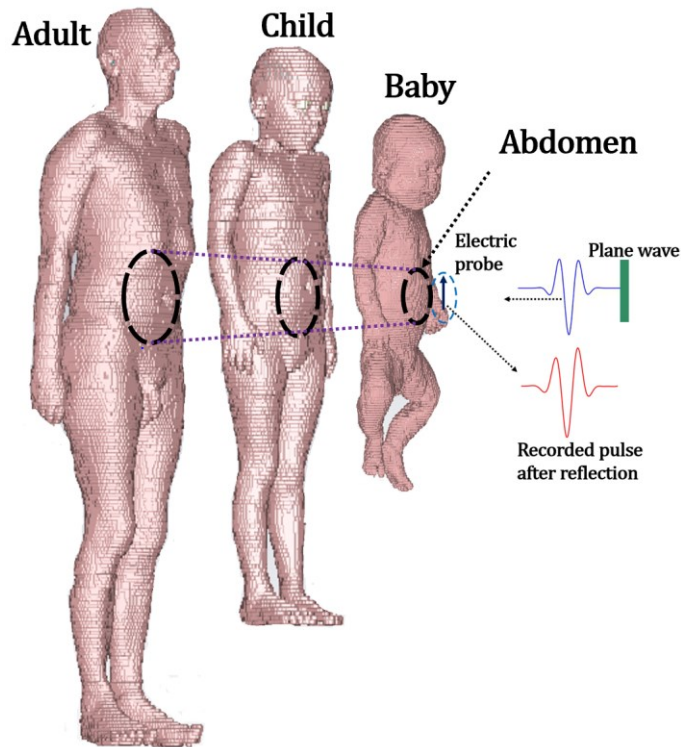
Figure 10. The voxel tissue model view of baby, child, and adult individually simulated in CST

Now, the correlation between the actual signal $y_1(t)$ and the estimated signal $y(t)$ is evaluated. The value of n is chosen where the correlation value is maximum, as shown in Fig.9 (2.5 mm skin

thickness), and the corresponding τ value is calculated using (2.13). This value is used in (2.10) to calculate the estimated thickness of the skin. The same analysis is carried out for different skin layer thicknesses and compared with the estimated value in Table 5. This methodology is then tested for the voxel tissue family consisting of adult, child, and baby tissue, which is available in the library of the CST microwave studio. Fig.10 shows the voxel tissue model of baby, child, and adult individually simulated in CST. The actual value of skin thickness varies according to the person's age [87]. From the comparison table of these voxel models, it can be shown that the proposed technique works efficiently to estimate skin thickness and the dielectric properties of humans of different age groups.

Table 5. Comparison of Skin true and estimated thickness value with error calculations

Case	True value(mm)	Estimated value(mm)	Error
1	20.0	19.8	1%
2	5.0	5.2	4%
3	4.0	3.9	2.5%
4	3.0	3.0	0%
5	2.5	2.7	8%
6	2.0	2.3	15%
Baby[43]	1.64±0.44	2.0	18%
Child[43]	2.17±0.48	2.2	1.38%
Adult[43]	2.39 ±0.15	2.3	3.7%

2.4.2 Setup for measurement using the proposed technique on a planar structure tissue model

The proposed technique is investigated using a planar structure of the pork tissue sample. As shown in Fig.11, the simulation setup is proposed in the CST microwave studio. Three metal
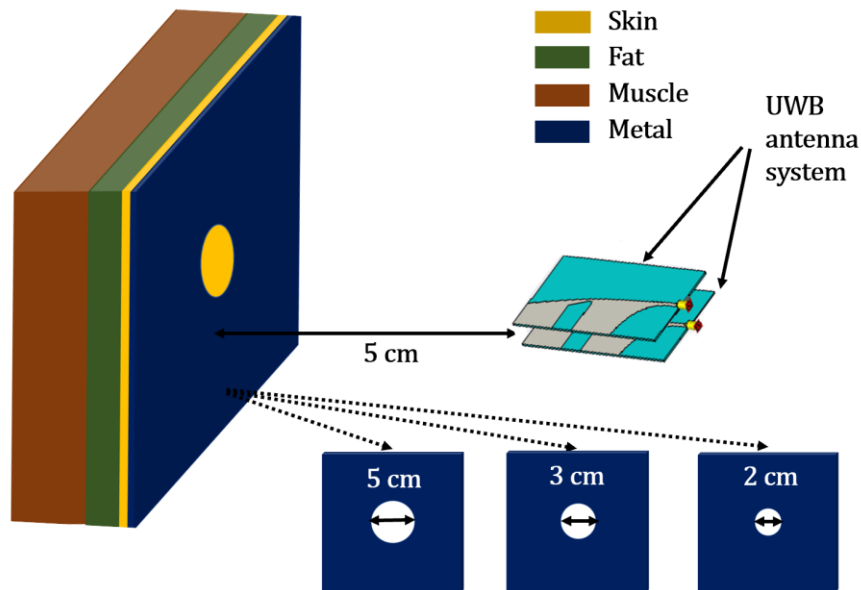
Figure 11. Measurement setup for pork tissue layers

plates with a circular aperture of 2 cm, 3 cm, and 5 cm are used for the experiments to precisely identify tissue properties in a specific area. The UWB antenna system consisting of two Vivaldi antennas is placed 5 cm apart from the metal, followed by pork tissue consisting of skin, fat, and muscle layers. The literature presents that these layers have specified permittivity and conductivity properties. The thickness of skin and fat layers are assigned with average values of 2.2 mm and 10.8 mm, respectively. First, three simulations are performed using just metal plates to extract the ambient signal occurring due to the mutual coupling of antennas and the metal plates.

Then, other simulations are conducted by introducing skin, fat, and muscle layers with the metal plate and antenna structures. The time-domain signals are recorded for each case, and genetic optimization is applied to estimate the complex permittivity and thickness. Table 6 summarizes the estimated pork skin, fat, and muscle complex permittivity with the corresponding metal plate.

Table 6. Estimated pork fat, skin, and muscle complex permittivity values using the proposed technique and error calculations

Aperture radius	ε_{r2} (skin) Ref. 35.4	Skin error	ε_{r3} (Fat)	Fat error (Ref. 8.21)	ε_{r4} (Muscle) Ref. 39.15	Muscle error
5 cm	35.66-0.054i	0.8%	8.71-0.195i	5.8%	34.88-0.163i	10.8%
3 cm	34.78-0.120i	1.8%	7.44-0.287i	9.4%	35.61-0.189i	9.1%
2 cm	37.76-0.102i	6.6%	8.2- 0.48i	0.1%	35.98-0.175i	8.1%

Table 7. Estimated pork fat and skin thickness values using the proposed technique and error calculations

Aperture radius	Skin (True) (mm) d_2	Skin (Est) (mm) d_2	Skin error	Fat (True) (mm) d_3	Fat (Est) (mm) d_3	Fat error
5 cm	2.2	2.2	0%	10.8	9.4	12.9%
3 cm	2.2	2.1	4.5%	10.8	11.7	8.3%
2 cm	2.2	2.2	0%	10.8	9.9	8.3%

The error for each layer permittivity is also estimated that lies within 11%, where a 3 cm aperture metal sheet shows the maximum error for fat assessment. Table 7 outlines the estimated pork skin and fat thickness for each case. In the case of 3 cm and 2 cm apertures, the error is around 8.3% for fat, while 0% and 4.5% for skin thickness, respectively. The maximum error for fat thickness is around 12.9% for a 5 cm aperture case.

2.4.2.1 Analysis of the skin thickness and permittivity variation

Analysis of simulation setup with skin thickness and permittivity variation is analyzed as shown in Fig.12. A total of ten cases are considered, involving five cases of skin thickness variation from 2-5 mm with a step of 1 mm and five cases of permittivity variation from 25-45 with the step of value 5.
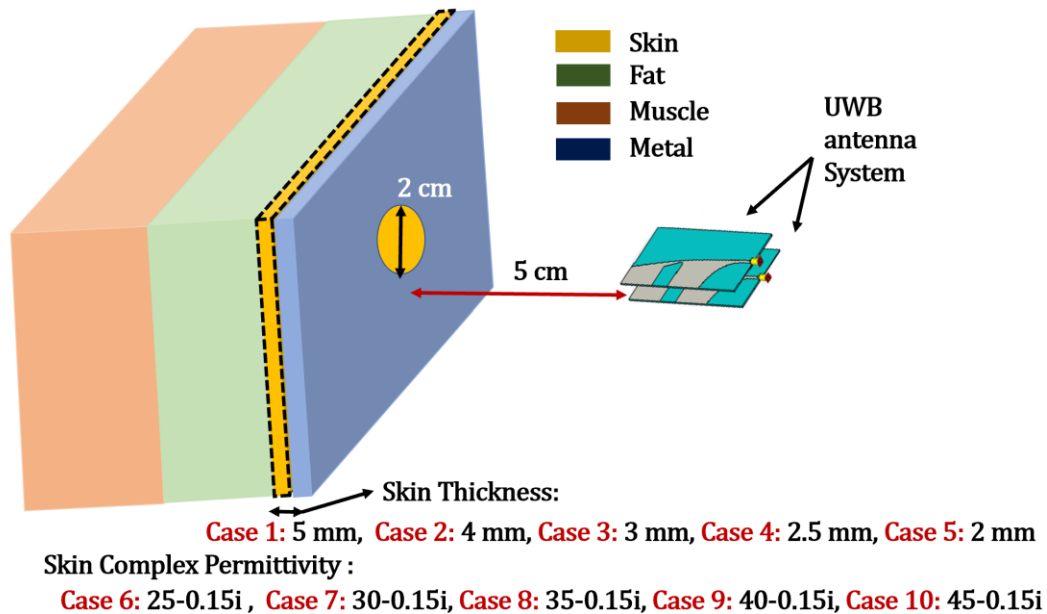
Figure 12. Simulation setup: skin thickness variation (Case 1-5) and skin permittivity variation (Case 6-10)

The fat thickness and permittivity values are 10.8 mm and 8.21-0.25i, respectively, and the same for all cases. A metal plate having an aperture of 2cm is considered for the simulation. Table 8 summarizes the estimated skin thickness and fat properties with error calculation for cases 1-5, whereas Table 9 describes cases 6-10.

Table 8. Estimated skin thickness and fat properties using the proposed technique and error calculations

Case	Skin True value(mm)	Skin Estimated value(mm)	Skin thickness Error	Fat thickness (Ref. 10.8 mm)	Fat thickness Error	ε_{r3} (Fat) Estimated (Ref. 8.21)	ε_{r3} (Fat) Error
1	5.0	4.9	4%	9.4	13%	8.15-0.12i	0.7%
2	4.0	4.2	2.5%	9.8	9.2%	7.99-0.10i	2.7%
3	3.0	3.1	0%	10.1	6.5%	8.5-0.01i	3.5%
4	2.5	2.4	8%	9.8	9.2%	8.3-0.11i	1.1%
5	2.0	2.0	0%	10.5	2.8%	8.8-0.01i	7.2%

Table 9. Estimated skin complex permittivity and fat properties using the proposed technique and error calculations

Case	ε_{r2} (skin) True	ε_{r2} (skin) Estimated	ε_{r2} (skin) Error	Fat thickness (Ref. 10.8 mm)	Fat thickness Error	ε_{r3} (Fat) Estimated (Ref. 8.21)	ε_{r3} (Fat) Error
6	25.0-15i	27.4-0.01i	9.6%	9.7	10%	8.05-0.25i	2%

7	30.0-15i	28.0-0.12i	6.7%	11.7	8.3%	7.8-0.02i	5%
8	35-0.15i	34.8-0.02i	0.58%	9.9	8.3%	9.2-0.2i	12%
9	40.0-15i	38-0.08i	5%	10.2	5.5%	8.1-0.15i	13%
10	45.0-15i	47.4-0.01i	5.3%	12.0	11%	9.3-0.05i	13%

2.4.2.2 Analysis of the fat thickness and permittivity variation
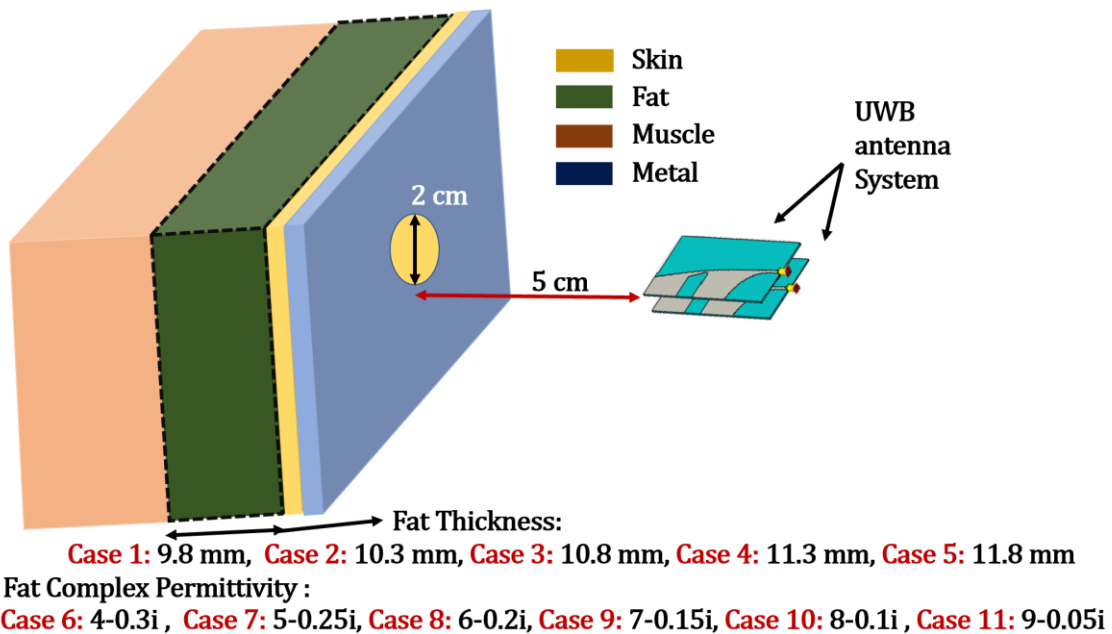
Figure 13. Simulation setup: Fat thickness variation (Case 1-5) and Fat permittivity variation (Case 6-11)

Additionally, analysis is performed when the skin thickness and permittivity values are kept constant, with variation in fat thickness and permittivity values, as shown in Fig.13. Cases (1-5) are a variation of fat thickness from 9.8-11.8 mm with the step of 0.5 mm, whereas Cases (6-11) are for fat permittivity value from 4-9 with the step of 1. The skin thickness and permittivity values

are 2.2 mm and 35.4-0.5i, respectively, and the same for all cases. Estimated fat thickness and skin properties with error calculation are summarized in Table 10, whereas fat complex permittivity and skin properties are shown in Table 11.

Table 10. Estimated fat thickness and skin properties values using the proposed technique and error calculations

Case	Fat True value(mm)	Fat Estimated value(mm)	Fat thickness Error	Skin thickness (Ref. 2.2 mm)	Skin thickness Error	ε_{r2} (skin) Estimated (Ref. 35.4)	ε_{r2} (skin) Error
1	9.8	9.5	3.06%	1.9	13%	36.55-0.04i	3.2%
2	10.3	10.4	0.97%	2.3	4.5%	33.01- 0.10i	6.7%
3	10.8	10.9	0.95%	2.2	0%	34.55- 0.12i	2.4%
4	11.3	11.5	1.76%	2.3	4.5%	34.53-0.02i	2.5%
5	11.8	11.7	0.85%	2.2	0%	38.56-0.03i	8.9%

Table 11. Estimated fat complex permittivity and skin properties values using the proposed technique and error calculations

Case	ε_{r3} (Fat) True	ε_{r3} (Fat) Estimated	ε_{r3} (Fat) Error	Skin thickness (Ref. 2.2 mm)	Skin thickness Error	ε_{r2} (skin) Estimated (Ref. 35.4)	ε_{r2} (skin) Error

6	4-0.3i	4.14-0.155i	3.5%	2.0	5%	35.2-0.04i	0.56%
7	5-0.25i	4.95-0.187i	1%	2.1	4.5%	33.74- 0.12i	4.7%
8	6-0.2i	6.07- 0.21i	1.2%	2.2	0%	34.2- 0.10i	3.4%
9	7-0.15i	6.8-0.20i	2.8%	2.3	4.5%	35.35-0.02i	0.14%
10	8-0.1i	7.55-0.23i	5.6%	2.2	0%	37.5-0.03i	5.9%
11	9-0.05i	8.87-0.11i	1.4%	1.9	13.6%	35.54-0.11i	0.4%

2.4.3 Setup for measurement using the proposed technique on the human voxel tissue model

After successfully determining the planar pork tissue properties, the proposed technique is tested on human voxel tissue models available in the CST microwave studio. Fig.14 shows the graphical representation of a baby tissue model with the UWB system and the 2-D cross-section view of the

baby's abdomen. The distance from the antennas to the surface of the abdomen is 5 cm. An ideal abdomen tissue model with elliptical hollow cylinders is structured to mimic the abdomen tissue characteristics, as shown in Fig.15. The curve metal sheet is placed on the skin, having an aperture of 2 cm. The average skin and fat thicknesses are defined as 2 mm and 5 mm, respectively. The electrical properties of skin and muscle layers are assigned as 34.5-0.5i and 35.4-0.12i, respectively, approximately close to human tissue properties.
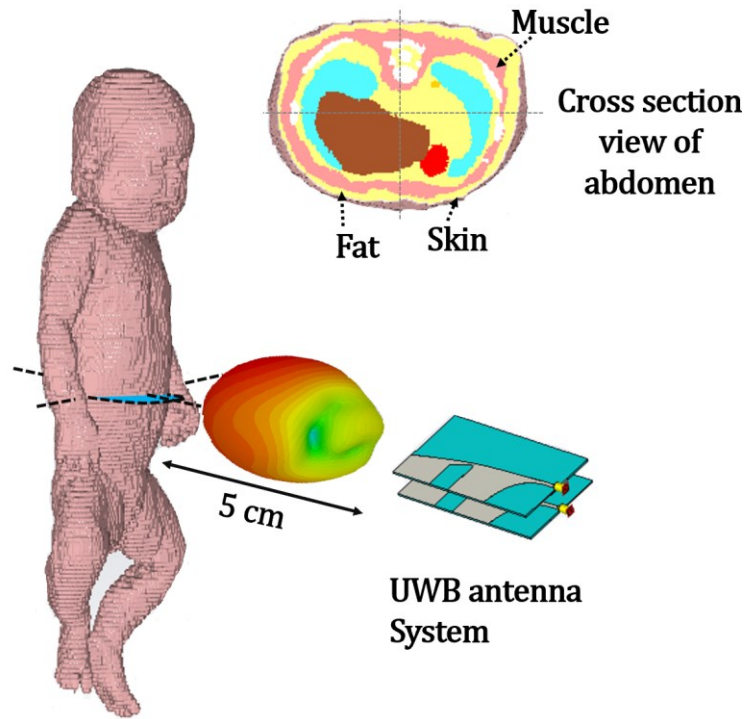
Figure 14. Graphical representation of baby tissue model with the antenna system
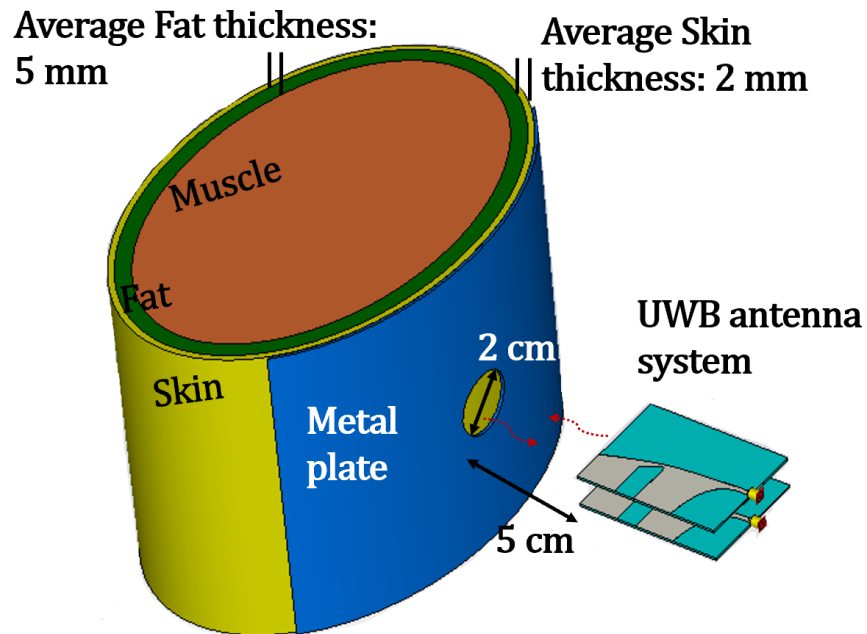
Figure 15. Graphical representation of ideal abdomen tissue model with the antenna system and a metal plate having a 2 cm aperture

The brown and white fat permittivity values are close to 4 and 9, respectively. The fat permittivity value increasing from 4 to 9 corresponds to the decrease in white fat content in the human body. Six simulations in total are performed by varying the fat tissue properties from values 4 to 9. Table 12 summarizes estimated ideal abdomen fat, skin, and muscle complex permittivity and error calculations. The error value for all instances is below 9.5%, which shows a promising result. The estimated fat and skin thickness with error calculation is also shown in Table 13. The maximum error of 15% is attained for skin thickness in the case of fat permittivity values of 5 and 7, whereas the fat thickness error crosses 5% when the fat permittivity values are 5 and 9. The ideal abdomen tissue results are convincing and acceptable.

Table 12. Estimated ideal abdomen fat, skin, and muscle complex permittivity value using the proposed technique and error calculations

Fat (ε_{r3}) True	ε_{r3} (Fat)	Fat error	ε_{r2} (skin) Ref. 34.5-0.5i	Skin error	ε_{r4} (Muscle) Ref. 35.4-0.12i	Muscle error
4-0.3i	4.38- 0.195i	9.5%	34.43-0.054i	0.2%	36.82- 0.163i	4%
5-0.25i	4.65- 0.287i	7%	33.74-0.120i	2.2%	35.18- 0.189i	0.6%
6-0.2i	6.26- 0.48i	3.8%	34.11-0.102i	1.1%	34.88- 0.175i	1.5%
7-0.15i	6.5-0.22i	7.1%	34.53-0.022i	0.8%	35.61-0.13i	0.5%

8-0.1i	7.31-0.13i	8.6%	36.56-0.03i	6%	36.79-.04i	3.9%
9-0.05i	8.14-0.02i	9.5%	35.54-0.122i	3%	34.76-0.05i	1.8%

Table 13. Estimated ideal abdomen fat and skin thickness values using the proposed technique and error calculations

Fat (ε_{r3}) True	Fat (True) (mm) d_3	Fat (Est) (mm) d_3	Fat error	Skin (True) (mm) d_2	Skin (Est) (mm) d_2	Skin error
4-0.3i	5	5.2	4%	2	1.9	5%
5-0.25i	5	4.4	12%	2	2.3	15%
6-0.2i	5	5.0	0%	2	2.2	10%
7-0.15i	5	4.9	2%	2	2.3	15%
8-0.1i	5	4.9	2%	2	2.2	10%
9-0.05i	5	4.7	6%	2	1.9	5%

Further, the baby human voxel tissue model available in CST is examined. Fig.16 shows the graphical representation of the selected abdomen baby tissue model with a metal sheet of 2 cm aperture placed at a distance of 5 cm from the UWB antenna system. The voxel model is 0.85 x 0.85 x 0.8 mm3 in resolution, and all other body parts in the abdomen are present. The abdomen tissue properties are assigned manually to test the proposed technique in the 5-10 GHz frequency range. As discussed in section II, the skin and muscle complex permittivity is assigned with actual average human tissue properties. Here also, six models with fat values from 4 to 9 are proposed.

Table 14 summarizes the estimated baby abdomen fat, skin, and muscle tissue complex permittivity, while Table 15 shows the fat thickness and skin thickness.
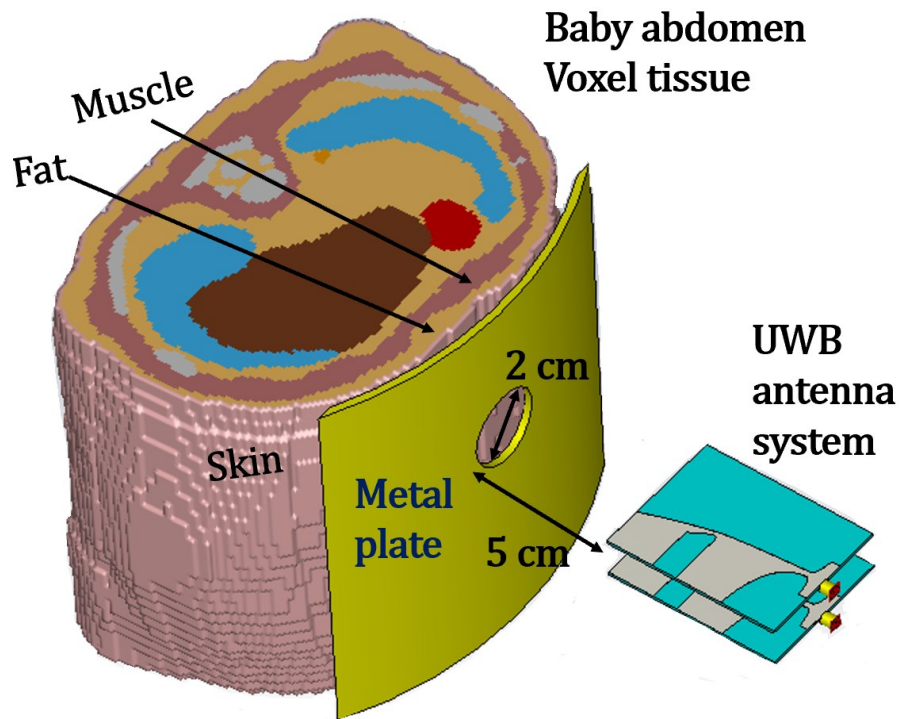
Figure 16. Graphical representation of baby abdomen voxel tissue model with the antenna system and a metal plate having a 2 cm aperture

The error calculated varies from 0.3% to 2% for fat tissue, 3.1% to 7.2% for skin tissue, and 0.2% to 9.5% for muscle tissue. The true thickness of fat for baby voxel tissue is the measured average thickness of 10 locations; states the reason for the maximum acquiring error of 31% in the case of fat dielectric constant is four. The skin thickness error lies below 20% for all cases.

Table 14. Estimated baby abdomen fat, skin, and muscle complex permittivity values using the proposed technique and error calculations

Fat (ε_{r3}) True	ε_{r3} (Fat)	Fat error	ε_{r2} (skin) Ref. 34.5-0.5i	Skin error	ε_{r4} (Muscle) Ref. 35.4-0.12i	Muscle error
4-0.3i	3.92-0.21i	2%	35.57-0.1i	3.1%	35.32-0.22i	0.2%
5-0.25i	4.9-0.12i	2%	36.63-0.02i	6.2%	35.25-0.13i	0.4%
6-0.2i	6.02-0.23i	0.3%	35.99-0.12i	4.3%	32.8-0.09i	7.3%
7-0.15i	7.04-0.10i	0.5%	37.00-0.04i	7.2%	34.28-0.02i	3.2%
8-0.1i	7.94-0.15i	0.8%	37.00-0.02i	7.2%	34.87-0.15i	1.5%
9-0.05i	9.17-0.01i	1.8%	35.82-0.05i	3.8%	32.01-0.08i	9.5%

Table 15. Estimated baby abdomen fat and skin thickness values using the proposed technique and error calculations

Fat (ε_{r3}) True	Fat (True) (mm) d_3	Fat (Est) (mm) d_3	Fat error	Skin (True) (mm) d_2	Skin (Est) (mm) d_2	Skin error
4-0.3i	7	4.7	31%	2.6	2.6	0%
5-0.25i	7	8.7	24%	2.6	3.0	15%
6-0.2i	7	8.9	27%	2.6	3.0	15%
7-0.15i	7	6.6	5.7%	2.6	2.1	19%
8-0.1i	7	4.7	31%	2.6	3.1	18%
9-0.05i	7	8.6	22%	2.6	2.8	7.7%

The proposed technique is also assessed for the child and adult human voxel tissue models. Fig.17 shows the desirable child and adult abdomen tissue models with a complete simulation setup. The child has only one composite layer of muscle and fat on average after the skin layer in the CST

model. The properties of this layer are evaluated with the percentage of fat content in the composite tissue.
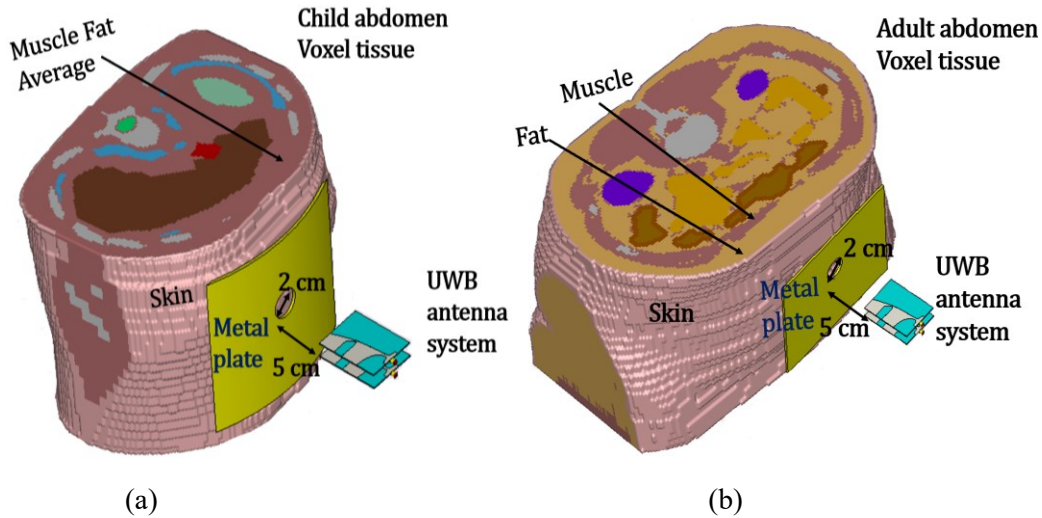
Figure 17. Graphical representation of (a) Child and (b) Adult abdomen voxel tissue model with the antenna system and a metal plate having a 2 cm aperture

A person with 30% fat content in the composite layer is considered obese, and correspondingly, the white fat tissue content is significantly more. A total of five cases are considered for the child abdomen tissue model, with the fat percentage varying from 15-30% in the composite layer. The average thickness for composite muscle fat and skin layers of the CST model is around 17.5 mm and 2 mm. Estimated child abdomen skin, muscle, and fat average tissue properties for all five cases are described in Table 16. The composite and skin layers' error values vary from 0.8-3.7% to 3.9-10%. Table 17 exhibits the estimated skin and muscle fat combined layer thickness with error calculations. The maximum error is around 14% for muscle and fat thickness with permittivity values of 25.28-0.25i and 30.46-0.05i. On the other hand, it is 18% for the voxel tissue of muscle fat with an average permittivity value of 30.46-0.05i. The other errors are equal to or below 20%.

Table 16. Estimated child abdomen fat, skin, and muscle complex permittivity values using the proposed technique and error calculations

Muscle-fat tissue (ε_{r3}) True	Muscle-fat tissue (Est)	Muscle-fat tissue error	ε_{r2} (skin) Ref. 72.93-0.5i	Skin error
24.24-0.3i	25.14-0.011i	3.7%	67.15-0.05i	7.9%
25.48-0.25i	25.08-0.11i	1.6%	65.53-0.1i	10%
26.73-0.2i	26.21-0.13i	2%	68.22-0.13i	6.5%
27.97-0.15i	27.73-0.09i	0.8%	68.44-0.05i	6.2%
30.46-0.05i	31.8-0.03i	4.4%	70.11-0.1i	3.9%

Table 17. Estimated child abdomen fat and skin thickness values using the proposed technique and error calculations

Muscle-fat tissue (ε_{r3})	Muscle-fat tissue (True) (mm) d_3	Muscle-fat tissue(Est) (mm) d_3	Muscle-fat tissue (thick.) error	Skin (True) (mm) d_2	Skin (Est) (mm) d_2	Skin error
24.24-0.3i	17.5	17.3	1.1%	2.1	2.3	9.5%
25.48-0.25i	17.5	20.5	17%	2.1	1.9	9.5%
26.73-0.2i	17.5	16.5	5.7%	2.1	1.9	9.5%
27.97-0.15i	17.5	17.9	2.3%	2.1	2.4	14%
30.46-0.05i	17.5	14.3	18%	2.1	2.4	14%

The adult abdomen voxel model has separate fat, skin, and muscle tissue layers resembling the voxel model for babies. The simulation setup is also the same for all six cases, with fat tissue

permittivity varying from 4 to 9. The skin and muscle properties considered are the actual human tissue properties. Table 18 presents the estimation of adult abdomen fat, skin, and muscle complex permittivity calculations with errors. The error varies from 1.6-10% for fat, 1.62-4.82% for skin, and 0.8-3.7% for muscle tissue. The estimated fat and skin layer thickness is shown in Table 19 with error calculations, and the results are quite convincing.

Table 18. Estimated adult abdomen fat, skin, and muscle complex permittivity values using the proposed technique and error calculations

Fat (ε_{r3}) True	ε_{r3} (Fat)	Fat error	ε_{r2} (skin) Ref. 34.5-0.5i	Skin error	ε_{r4} (Muscle) Ref. 35.4-0.12i	Muscle error
4-0.3i	4.4-0.26i	10%	33.93-0.21i	1.65%	36.25-0.06i	2.4%
5-0.25i	4.84-0.012i	3.2%	35.95-0.45i	4.2%	34.35-0.06i	2.96%
6-0.2i	5.81-0.012i	3.2%	34.93-0.61i	1.24%	35.73-0.053i	0.9%
7-0.15i	6.86-0.007i	2%	35.24-0.52i	2.15%	35.43-0.06i	0.8%
8-0.1i	7.75-0.01i	3.1%	35.06-0.58i	1.62%	36.49-0.04i	3.07%
9-0.05i	9.14-0.01i	1.6%	36.17-0.71i	4.84%	34.76-0.07i	1.8%

Table 19. Estimated adult abdomen fat and skin thickness values using the proposed technique and error calculations

Fat (ε_{r3}) True	Fat (True) (mm) d_3	Fat (Est) (mm) d_3	Fat error	Skin (True) (mm) d_2	Skin (Est) (mm) d_2	Skin error
4-0.3i	25	28.4	13.6%	2.7	2.8	3.7%
5-0.25i	25	22.2	11.2%	2.7	2.8	3.7%
6-0.2i	25	27.2	8.8%	2.7	2.8	3.7%
7-0.15i	25	28.9	15.6%	2.7	2.9	7.4%
8-0.1i	25	28.0	12%	2.7	2.9	7.4%
9-0.05i	25	22.1	11.6%	2.7	2.7	0%

2.5 Specific absorption rate (SAR) calculation of human models

The specific absorption rate (SAR) value measures electromagnetic radiation absorbed by an object. In the case of humans, it is calculated over a specific volume of tissue averaged over 1 g or 10 g of tissue. SAR calculations and analyses are essential to know the effect of continuous exposure to radiation on human health. According to international commission bodies, the safe value of SAR is 1.6 W/kg for an average of 1 g of human tissue. The exposure time, electric field intensity, frequency of operation, placement, and orientation of the antenna are significant factors affecting the value of SAR [90] [91]. The SAR value is defined as follows:

$$SAR = \frac{\sigma |E|^2}{\rho}$$

(2.14)

where E is the induced electric field, and σ and ρ are the electrical conductivity and the mass density of human tissue, respectively.

Average SAR is a critical parameter for assessing the tissue safety of the proposed UWB technique. SAR analysis is carried out over a 3-D model of baby, child, and adult human voxel tissues. The SAR value is evaluated on the abdomen of the baby, child, and adult tissue model when the antenna is placed around 5 mm apart. The model is simulated using CST Microwave Studio, utilizing the finite difference time domain method. The excitation is a Gaussian pulse of 100 ps with a normalized amplitude of 1 V. Fig. 18 shows the maximum value of SAR averaged over 1g of human tissue at 10 GHz for all three tissues, respectively. The area in red for baby, child, and adult tissue models indicates the maximum SAR values of 0.34 W/kg, 0.43 W/kg, and 0.55 W/kg, respectively. The proportion of fat content is associated with the water in the body: more fat, less water. As a result, most adults are fat compared to children and infants. Therefore, the SAR value averaged over 1g tissue is more for adults than children and babies [92]. Supplementary areas of the abdomen, mainly in blue, have a SAR value of 0.01-0.05 W/kg, which means there will be a very subtle effect of electromagnetic waves even over a long exposure time. The value of SAR is calculated considering the thickness and permittivity of the human model's skin, fat, and muscle tissues. The properties of all the tissue are selected from the literature discussed in section 2.2.
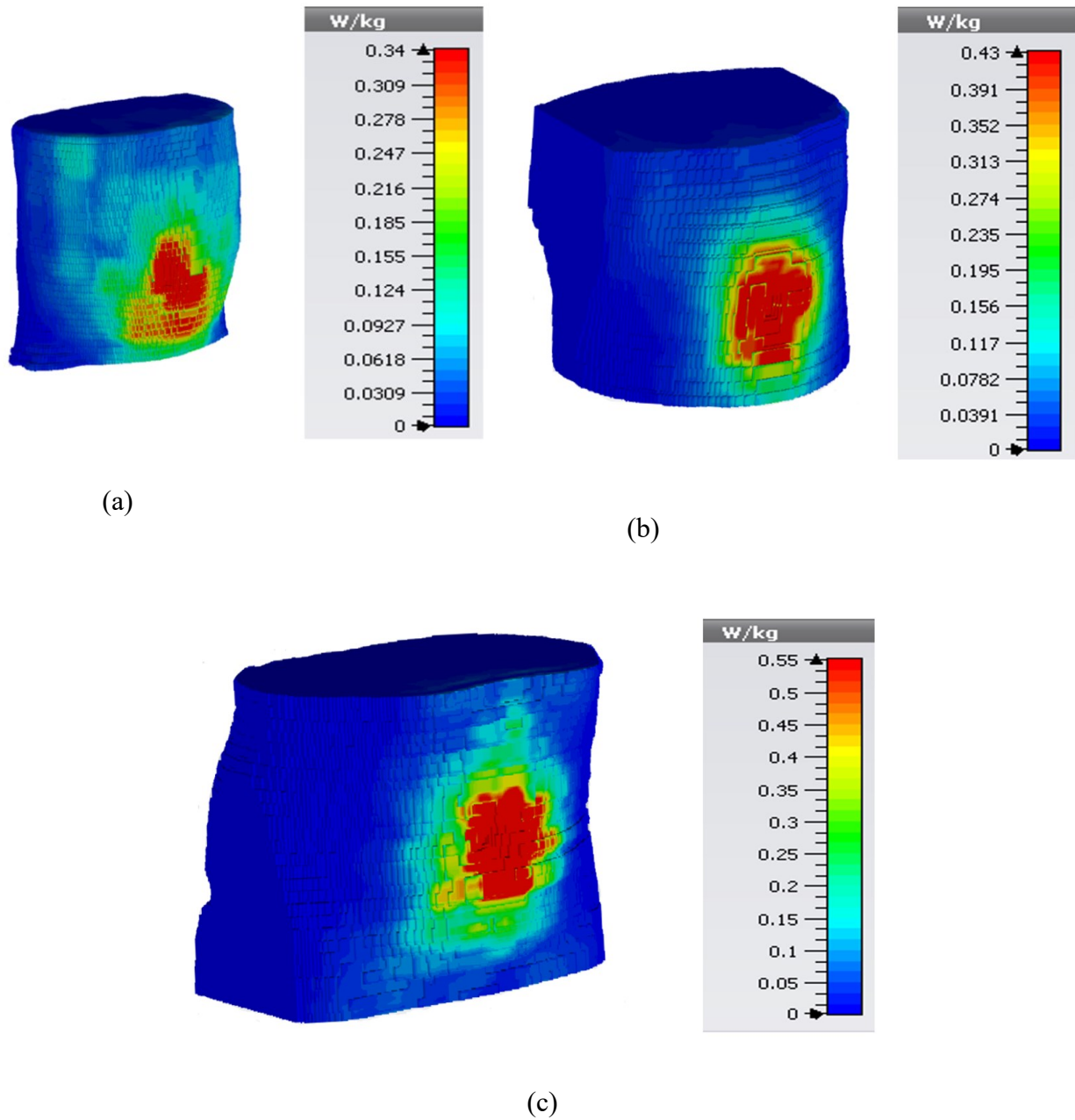
Figure 18. SAR value averaged over 1 g of human tissue at 10 GHz for (a) Baby abdomen, (b) Child abdomen, and (c) Adult abdomen

The SAR calculation is assessed for the frequency range of 5 GHz-10 GHz on all the tissue models.

Fig.19 shows the value of SAR averaged over 1g of human tissue for baby, child, and adult models

in the operating frequency range. The graph is plotted considering the maximum value of SAR at a particular frequency, primarily affecting the red area as shown in Fig.18 for the baby, child, and adult abdomen tissue models. The average value of SAR over the frequency range can be calculated using the following formula:

$$Average\ SAR = \frac{\int_{f_1}^{f_2}|s(f)df|}{f_2 - f_1} \tag{2.15}$$

where integral of $s(f)df$ is the area under the curve, and f_2 and f_1 are the maximum and minimum frequencies in the range of operation. Table 20 shows the average SAR value over the desired frequency range of all three human tissue models.
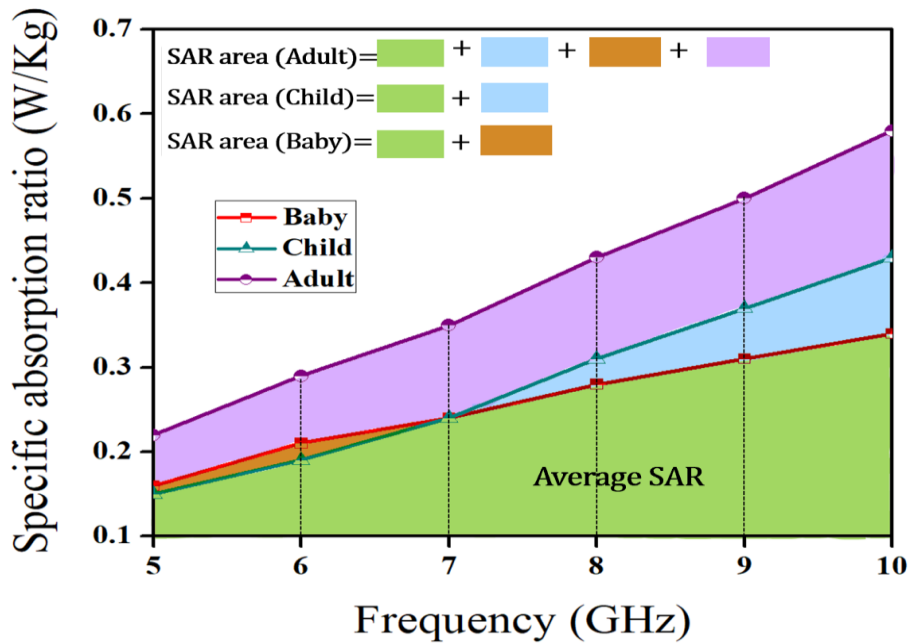
Figure 19. SAR curves as a function of frequency with the area under the curve for calculation of average SAR

The average SAR value obtained for the adult abdomen is 0.394 W/kg.Hz over 1 g of human tissue; it is 0.339 W/kg.Hz for a child, and 0.294 W/kg.Hz for a baby. The above calculation for SAR indicates that the proposed method is safe to use even for long human abdomen exposure to electromagnetic radiation.

Table 20. Average SAR value of human tissue models

S. No	Description	Average SAR(W/kg)
1.	Baby	0.294
2.	Child	0.336
3.	Adult	0.394

2.6 Measurement setup

The pork sample consists of skin, fat, and muscle, as shown in Fig.20. Additionally, ground chicken, ground beef, and ground turkey are substituted in the muscle layer to evaluate the proposed technique further. First, pork is used for evaluation purposes as pig tissue properties are alternative to human tissue properties and almost resemble complex permittivity and thickness [81][68]. Human skin can be substituted by pork skin; human fat corresponds to pork lard, and human muscle analogues with ground pork with 12% fat [62]. For the measurements, the dimension of pork material having skin, fat, and muscle layer is approximately 15 cm in length and 17 cm in breadth.

The simulation setup shows promising results; hence, this setup is used for the experiment in the laboratory on inactive pork sample tissues. Fig. 21 shows the lab experiment setup of metal plates with 5 cm, 3 cm, and 2 cm circular radius cut when placed on the pork tissue sample.
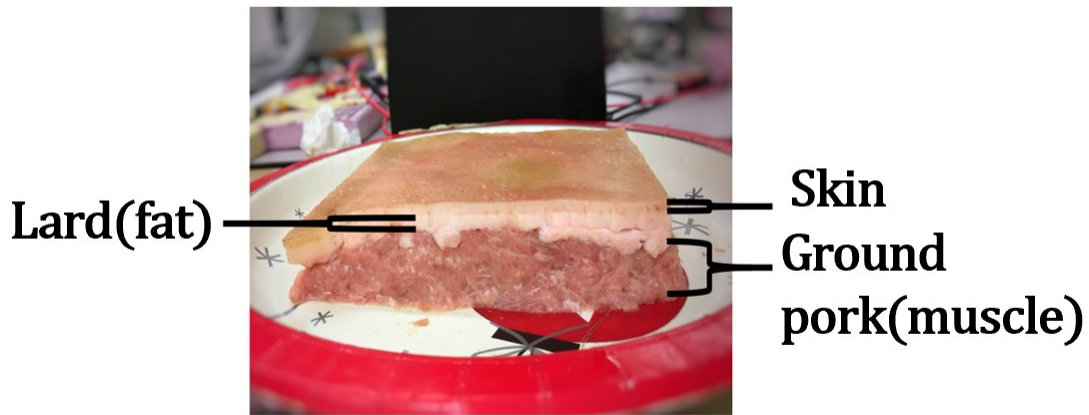
Figure 20. Pork tissue sample with skin, lard, and muscle layer

The transmitter antenna in the UWB system is excited with a 100 picoseconds Gaussian pulse generator circuit while the receiver antenna is connected to the high-frequency sampling oscilloscope. The UWB system is placed at a distance of 15 cm away from the sample surface. Each experiment with different metal plates is performed three times at three different locations to check the accuracy of the proposed technique and measurement setup.
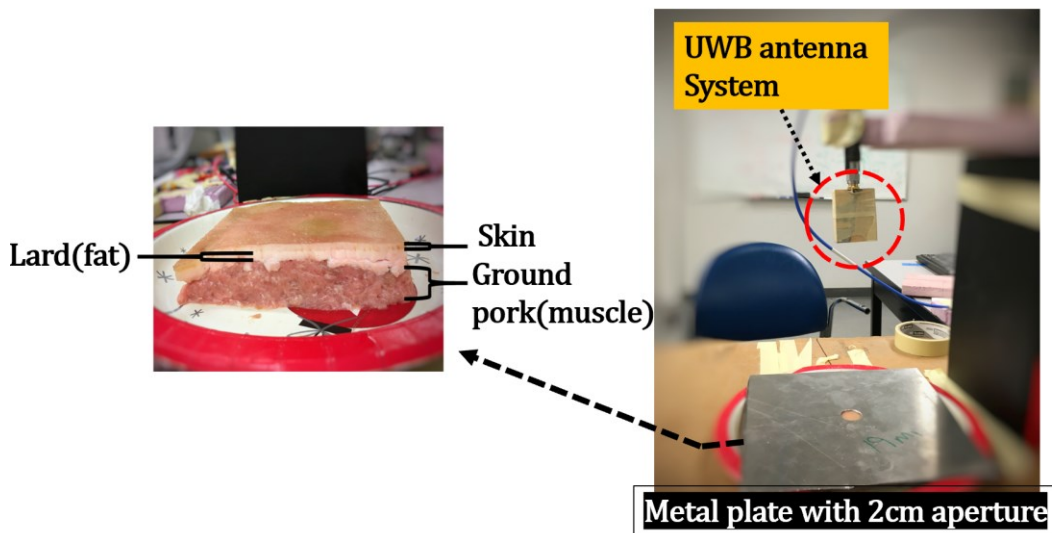
(a)
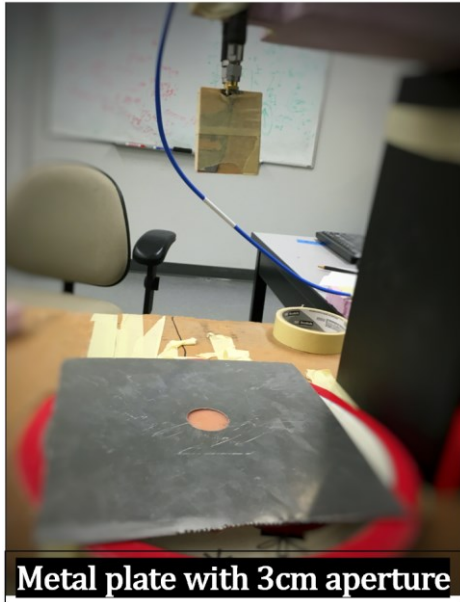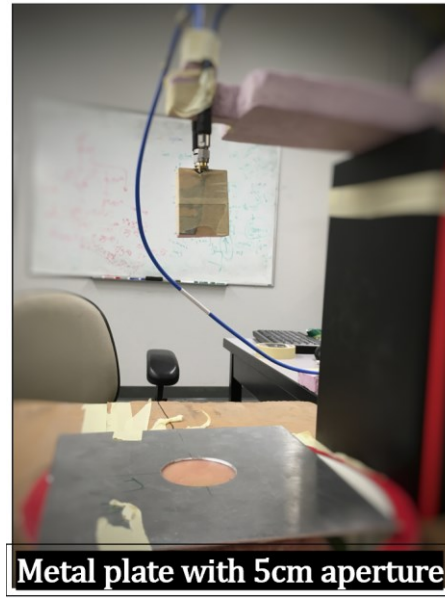
<center>(b)   (c)</center>

<center>Figure 21. Laboratory measurement setup for pork tissue sample (a) 2 cm aperture, (b) 3 cm aperture, and (c) 5 cm aperture metal plate</center>

2.7 Results and discussion

As mentioned earlier, a metal sheet with three different apertures is placed on the sample (see Fig. 18), and the UWB receiver acquires the transient data. The reason for choosing narrow apertures is to identify tissue properties in the specific area precisely. Then, the minimization problem was solved to estimate the complex permittivities and thickness of the tissue. The relative permittivity and loss tangent value of unknown fat tissue as the function of frequency in the range of 5GHz-10.5 GHz is exhibited in Fig.22(a). The graphs show the experimental data for three random locations on the surface of the multilayer sample tissue using a 2 cm, 3 cm, and 5 cm aperture metal plate. Fig. 22 (b) shows the pork muscle complex permittivity over the valid frequency span. The ex-vivo average permittivity value of muscle is calculated to be 35.89, with an average loss tangent value of 0.23.

Table 21. Estimated animal fat, skin, and muscle complex permittivity values using the proposed technique and error calculations

	ε_{r2} (skin)	ε_{r3} (Fat)	Fat Error (Ref. 8.05)	ε_{r4} (Muscle)	Muscle error
Ground Beef (Ref. 37.74)	43.97- 0.18i	7.51– 0.12i	6.7%	34.29- 0.35i	9.1%
Ground chicken (Ref. 38.86)	37.68- 0.03i	7.73- 0.05i	3.9%	37.65- 0.44i	3.1%
Ground Turkey (Ref. 43.23)	35.22- 0.02i	8.37- 0.29i	4.0%	38.93- 0.65i	9.9%
Ground Pork (Ref. 39.97)	34.95- 0.24i	8.60- 0.71i	6.8%	36.25- 0.50i	9.3%

The average permittivity and loss tangent value effectively differ by less than 4% and 2%. The average estimated complex permittivity, the reference values, and the absolute error percentage are reported in Table 21 and hold measurements done in duplicate. The results highlight a considerable agreement in permittivity and loss tangent values in all six cases with minor errors. Table 21 also shows the average value of pork skin complex permittivity over the frequency span. The results approximately resemble the true pork skin properties illustrated in [76].

In addition, the average thickness of the skin and fat pork tissue samples is measured using a ruler. The sample taken was not uniform in terms of skin and fat thickness, so the actual fat thickness value was determined by measuring and averaging ten different cross-sections, while actual skin thickness was varied from 1.5 mm-3 mm.

Table 22. Estimated animal fat and skin thickness values using the proposed technique and error calculations

	Skin (Est) (mm) d_2	Skin (True) (mm) d_2	Fat (Est) (mm) d_3	Fat (True) (mm) d_3	Fat thickness error
Ground Beef	1.6	1.5- 3	10.3	10.8	4.6%
Ground chicken	1.6	1.5- 3	14.1	13.8	2.2%
Ground Turkey	2.9	1.5- 3	10.7	10.8	0.9%
Ground Pork	1.5	1.5- 3	11.1	10.8	2.8%

The estimated skin and fat thickness of pork tissue samples are summarized in Table 22. The average estimated skin and fat thickness were 1.5 mm and 15.4 mm, respectively. These values differ by approximately 5% and 9.5% of actual pork skin and fat (lard) thickness. The estimated properties of pork skin, fat, and muscle showed comparable results with the actual values. Since the pork tissue sample resembles the human tissue property, the proposed technique can be helpful in determining the properties (i.e., relative permittivity and thickness) of fat tissue in the human body efficiently. Other tissue models such as ground chicken, ground turkey, and ground beef are taken as a muscle layer and replaced individually under separate pork skin and lard sample tissues. The permittivity of ground chicken, beef, and turkey is measured beforehand using a coaxial probe method (Agilent 85070E). First, the sample having ground chicken as a muscle layer is experimented with using different aperture metal plates placed on the pork skin layer. Fig.22 (c) shows the permittivity and loss tangent of the ground chicken, which can be considered a muscle layer. Ground chicken tissue permittivity deviates approximately 5% from the true values of ex vivo tissues.
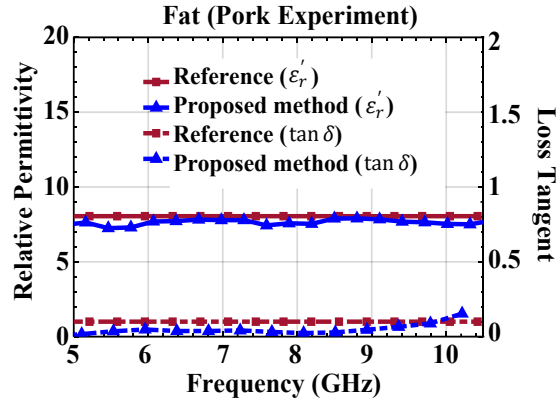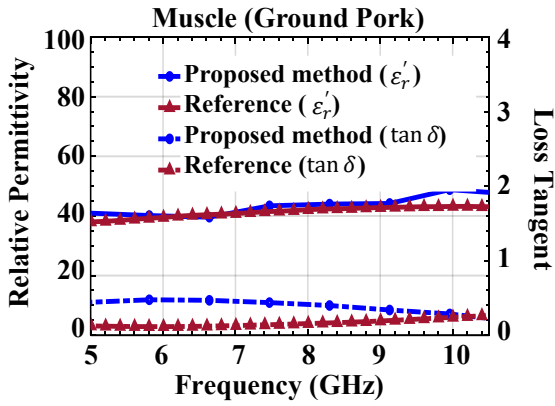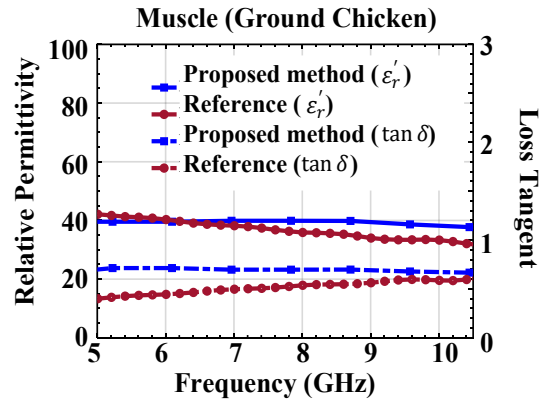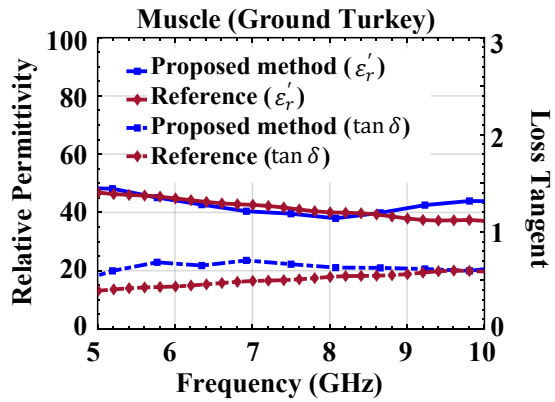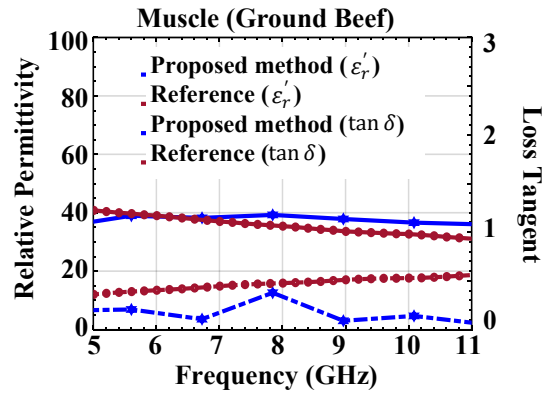
Figure 22. A plot of permittivity and loss tangent value for a) pork fat, b) muscle (ground pork), c) muscle (ground chicken), d) muscle(ground turkey), and e) muscle(ground beef)

In addition, the retrieved thicknesses of the skin and fat layer are summarized in Table 22. The actual thickness for pork skin and fat(lard) is different from the first pork tissue sample and is determined by the same analogy of measuring and averaging for ten different locations. The estimated values are lower by 13% and 5% than actual pork skin and fat thickness. Furthermore, a study for ex vivo pork skin and fat sample tissues with the ground turkey and beef (as muscle layer) is also executed. Quantitative differences are perceived between the overall permittivity and the viable conductivity obtained in this investigation, and values are compared with actual properties.
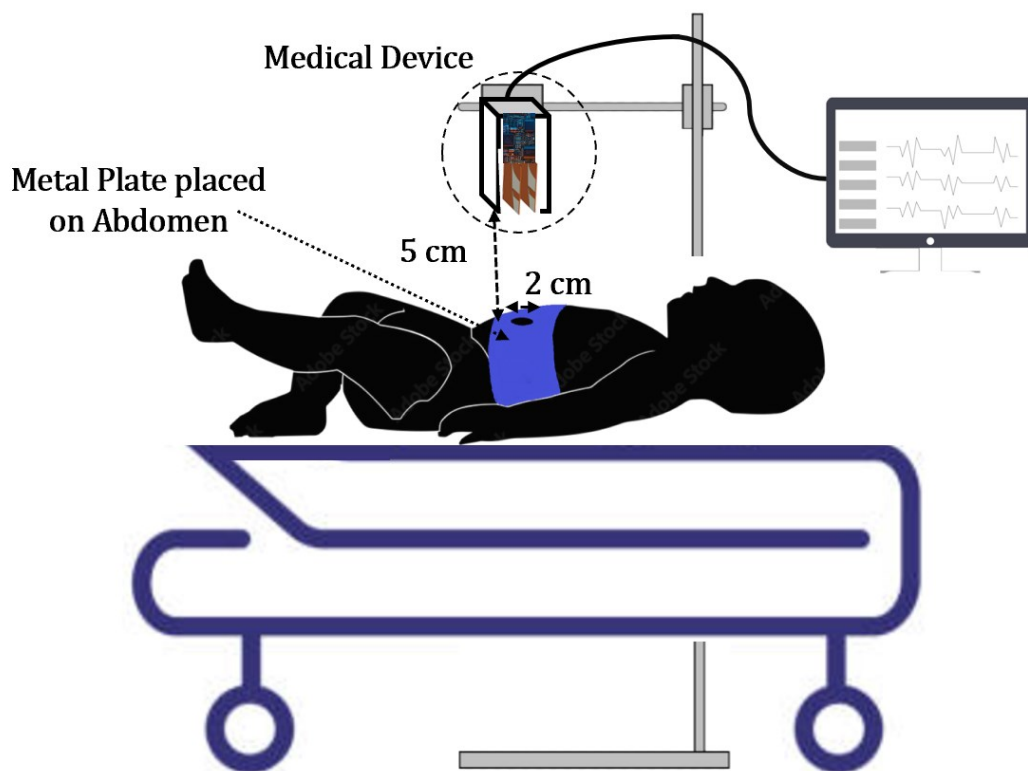
Figure 23. Graphical representation of medical device equipped with antenna system and pulse generator circuit performed on child abdomen with a metal sheet having certain circular aperture cut

Fig. 22 (d) and Fig.22(e) show the plot of permittivities and loss tangents of ground turkey and ground beef, respectively. Table 21 shows the estimated average complex permittivity of pork skin and fat (lard) with ground beef and turkey. It can be discerned that the difference in estimated pork fat value is typically within ± 8% compared to an actual value in the case of sample tissue with ground beef and ground turkey, respectively. The average values obtained using all the experimental cases agree well with the actual value of muscle tissue type. Table 22 shows that the estimated pork fat and skin thickness for these two cases are comparable with the true average values. The complete analysis of pork skin and fat determination with a muscle layer of all animal muscle tissues shows promising results using the proposed technique and methodology. The medical device equipped with the UWB system and the gaussian pulse wave generator circuit can be proposed and utilized to estimate the fat tissue type in humans. Fig. 23 shows the graphical representation of the proposed medical device when operating on the child's abdomen to estimate the content and properties of tissues, mainly in terms of the type of fat tissue, such as brown fat or white fat, and the skin and muscle properties.

2.8 Conclusion

This chapter proposes a non-invasive ultra-wideband radar technology to measure the electrical properties and thickness of human tissue. The proposed method was validated using full-wave simulations and experimental measurements. The experiments are conducted using pork tissue as it mimics the human tissue. First, a similar scenario consisting of the pork tissue sample and antenna system is created in simulation software and studied. Then, the same setup was mounted in the laboratory to determine the dielectric properties of skin, fat, and muscle; and the thickness

of skin and fat. The estimated results were comparable with actual pork tissue's permittivity and thickness values in simulation and laboratory experiments. Subsequently, three other models with different muscle layers (i.e., ground chicken, ground turkey, and ground beef) are evaluated and analyzed. The experiment results agree with the reference values of electrical properties and tissue thickness within 10 % for all the cases. By measuring the dielectric constant and thickness of the fat layer, it is possible to conclude the obesity level of the person. The dielectric constant of fat depends on the percentage of brown and white fat in an individual body. Generally, the dielectric constant is between 4 and 8, depending on their percentage. If the dielectric constant of the fat layer is close to 8, it concludes more brown fat, while if it is close to 4, it indicates more white fat. Specific absorption ratio (SAR) calculation is done to analyze the effect of radiation exposure on human tissue. The average SAR value averaged over 1 g of human tissue analysis shows acceptable results, indicating that this technique is safe to use. Hence, this study showed the feasibility of the proposed technique becoming a clinical solution in the form of a medical device to determine the percentage of brown and white fat in the human body.

Chapter 3

Non-invasive prognosis of knee osteoarthritis using UWB microwave imaging system

3.1 Introduction

Magnetic resonance imaging (MRI) [93], radiographic testing [94], x-ray [95], computed tomography (CT) [96] , and ultrasound [97] are some of the present modalities used to examine the functional and pathological condition of knee diseases. In [93], an automated MRI method is proposed to study knee osteoarthritis. Musculoskeletal disorder in the knee is assessed by radiographic testing, which utilizes x-rays or gamma rays to examine the internal structure of tissue [94]. Early detection of knee Osteoarthritis is performed in [95] using a discriminative regularized autoencoder dealing with x-rays images. In [96], cone beam computed tomography is used to detect one of the characteristics of osteoarthritis. In [97], an ultrasound technique utilizing a knee brace to diagnose osteoarthritis has been proposed. Recently in [98], Fluorodeoxyglucose (FDG)

radiotracer is injected into the human body, and imaging is produced using the positron emission tomography technique for early detection of degenerative osteoarthritis. Cartilage structure, joint effusion, and signs of synovitis are determined to identify the knee problem. Fig. 24 shows the anatomy of a) normal knee and b) knee with osteoarthritis.
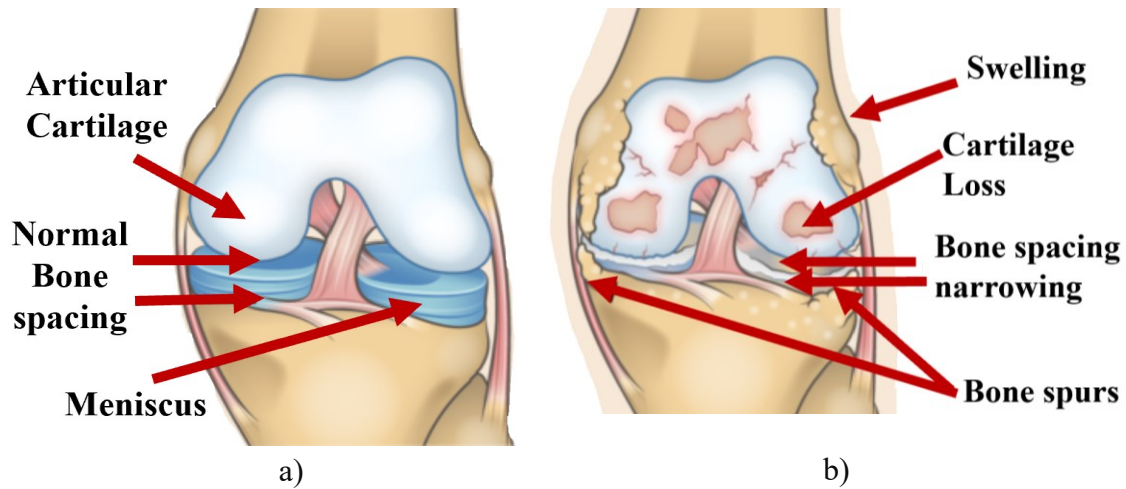
Figure 24. a) Normal Knee b) Knee with Osteoarthritis

Table 23.Techniques to measure Tissue properties

	Technique	Contact/ contactless	Cost	Harmful to tissue
[93]	MRI	Contactless	high	No
[94]	Radiography	Contactless	high	Yes
[95]	X-Ray	Contactless	low	Yes
[96]	CT Scan	Contactless	high	Yes
[97]	Ultrasound	Contact	low	No
[98]	PET Scan	Contactless	high	Yes

Present	Microwave	Contactless	low	No

This chapter illustrates the proposed microwave imaging method used to study knee osteoarthritis in humans. The properties of the knee joint such as permittivity, and the gap between the thigh bone and shinbone, are assessed to estimate the osteoarthritis condition. The simplified knee phantoms and voxel tissue knee model available in CST software are used in this study. The images for all phantoms are first reconstructed using circular synthetic aperture radar (CSAR), followed by the proposed SAR-focused microwave reflection tomography (SMRT) technique for the voxel knee phantom. The comparison of the voxel knee joint obtained by the proposed SMRT technique and CSAR is illustrated and analyzed. It is the first time UWB radar imaging and knee tissue electrical properties are used to analyze osteoarthritis. This paper also develops SAR-focused microwave reflection tomographic imaging for the knee joint. These methods provide a possibility to prognose osteoarthritis conditions in humans with minimal cost and discomfort. The permittivity and gap between the thigh bone and shinbone are estimated using an ultra-wideband (UWB) radar and genetic algorithm. The estimation of muscle properties and depth from the skin surface to bone is discussed.

This chapter is arranged as follows. Knee phantoms and their properties in section 3.2. Experimental setup for knee imaging using SAR-focused microwave reflection tomography analysis in section 3.3. Section 3.4 shows the microwave knee imaging simulation setups and their analysis. The UWB technique and methodology to determine the knee permittivity and depth are investigated and presented in section 3.6 and the conclusion in section 3.7.

3.2 Knee phantoms and their properties

The contrast in electrical properties of tissues causes the electromagnetic signal reflection, so a comprehensive study of the knee structure and its tissue properties is necessary before designing the UWB imaging system. In the human knee, the primary layer is the skin consisting of the epidermis and dermis layer, having a combined thickness of around 2-3 mm and average permittivity of 34.45 in the frequency range of 4-9 GHz. The layer followed by the skin is a fat layer that is around 5-6 mm thick and has an average permittivity of value 4.9 [99] [100]. The knee joint is connected through the femur (thigh bone) and the tibia (shinbone). The smaller bones, which are located next to the shinbone and the kneecap, are other bones that make up the knee joint. The fat layer is not present around the knee joint. Tendons and ligaments are attached to the knee joint, which is surrounded by muscle and skin layers. The tendons connect the knee bones to the knee muscles that move the knee joint, and ligaments are attached to the knee bones, which provides stability [101]. The average permittivity and conductivity values of the human knee in the frequency range of 4-9 GHz are summarized in Table 24 [102].

Table 24. Human knee tissue properties in the frequency range (4-9GHz)

Description	Average permittivity (ε_r)	Average conductivity (S/m)
Skin	34.45	4.62
Fat	4.9	0.35
Muscle	47.45	6.11
Bone	8.54	1.3
Ligament/Tendon	34.5	6.16

Table 24 shows the dielectric constant values of the knee for the healthy patient. The dielectric profile of tissue around the knee changes when the patient suffers from osteoarthritis. When a ligament rupture occurs, synovial fluid [37] containing blood collects at the rupture site and begins to fill the entire knee joint causing effusion. Due to its high dielectric properties: permittivity value of 84 and conductivity of 2.3 S/m [38] compared to the low dielectric properties of other knee tissues, this fluid changes the overall dielectric properties of the knee joint. Due to the ligament rupture and accumulation of synovial fluid, the average permittivity of the injured knee changes close to 82 in the frequency range 4-9GHz.
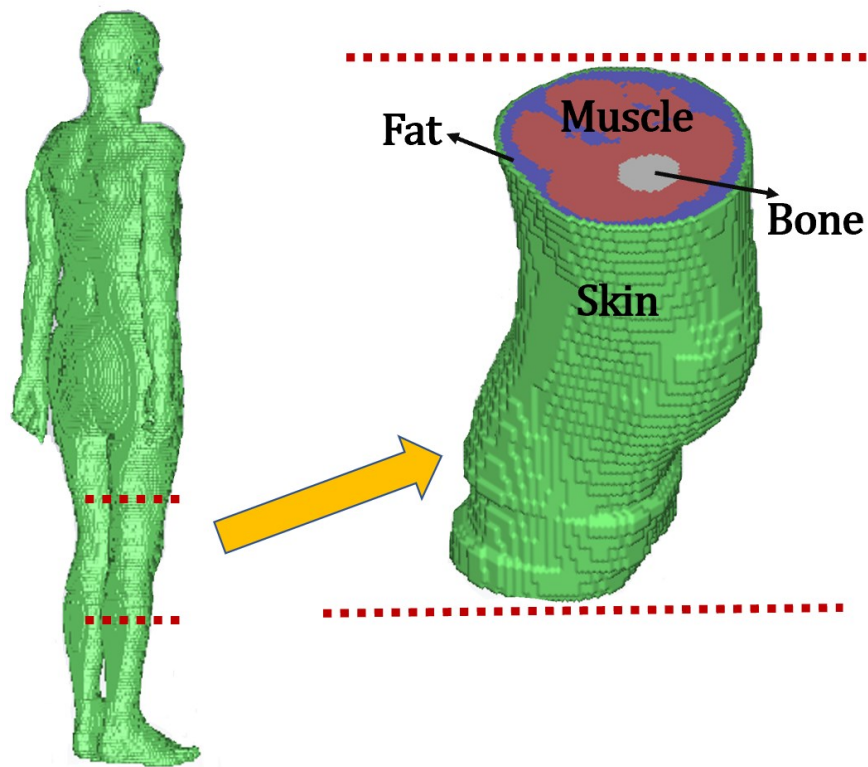
(a)
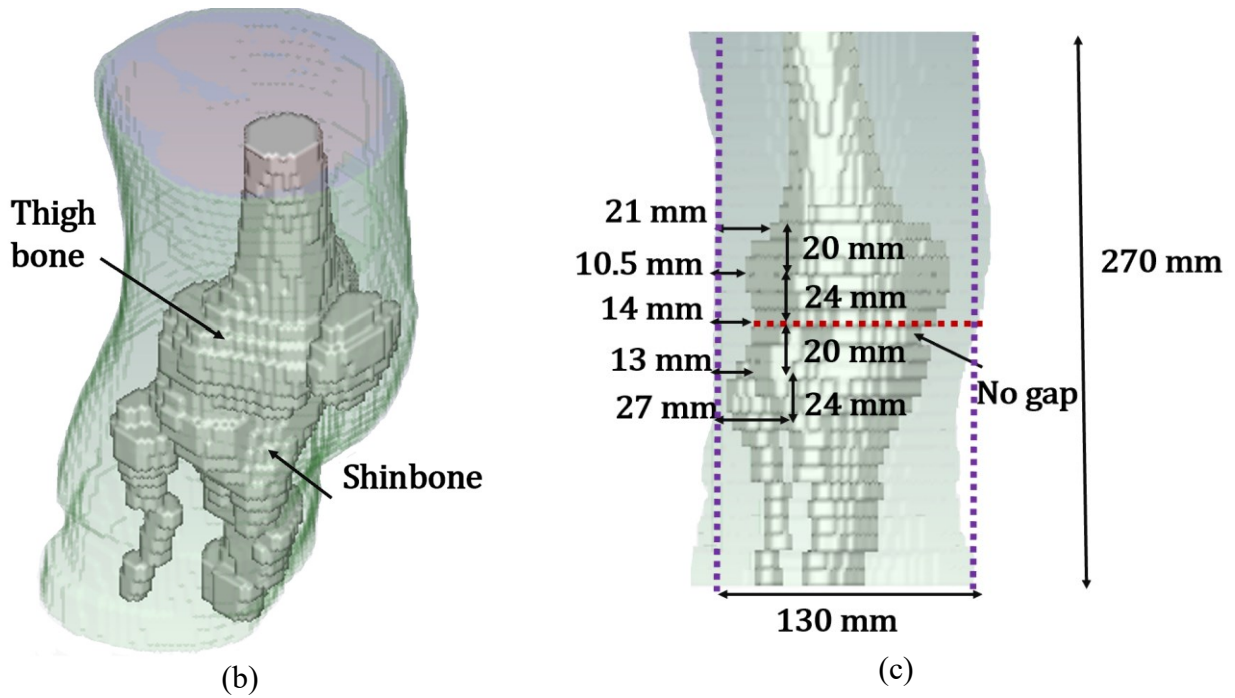
Figure 25. Human voxel knee available in CST software

The Gustav voxel knee model available in the CST microwave studio [103] is studied using the proposed technique. Fig.25(a) shows the knee model extracted from the complete Gustav human model. The voxel model is 0.85 x 0.85 x 0.8 mm^3 in resolution, 270 mm in height, and 130 mm in diameter. The knee model has the outermost skin layer followed by the fat layer. In the knee anatomy, the fat layer is usually not present around the knee joint, and it is the same for the voxel model as well. The layer followed by the fat layer is the muscle layer which includes ligaments/tendons and has the same overall relative permittivity value. Altogether it is considered a single muscle layer in the human voxel model.
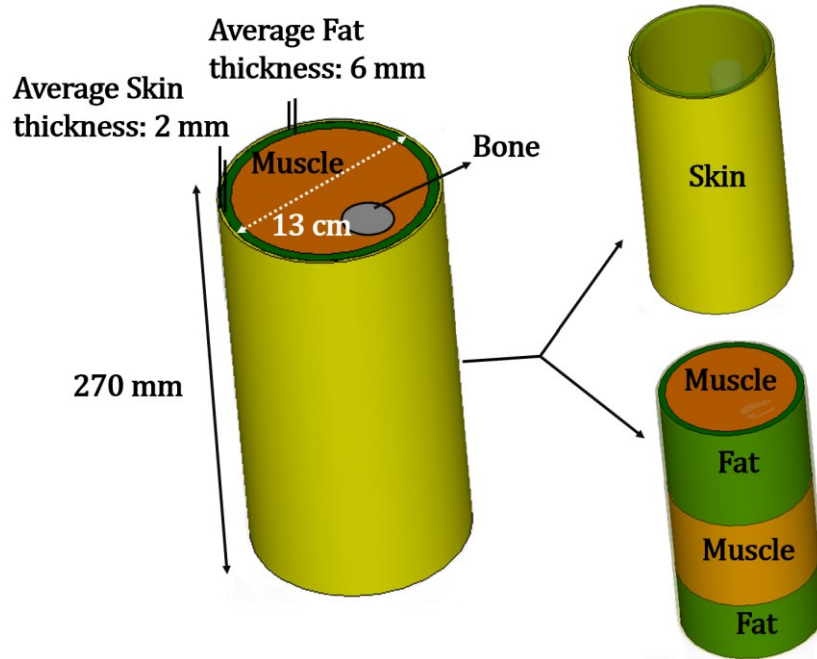
Figure 26. Graphical representation of the simplified human knee model

The last layer is bone, which resembles the same structural anatomy of knee bones having shinbone and thigh bone. There is no gap between the shinbone and thigh bone in the voxel model, as shown in Fig.25 (b), which is the case of osteoarthritis. So, for the proposed technique, this knee voxel model is considered as the case of a patient knee with an osteoarthritis problem. The electrical properties of skin, fat, and bone are assigned as described in Table 24, and muscle with a dielectric permittivity close to 82 considering the case of synovial fluid accumulation for the patient with osteoarthritis. The depth (in mm) at five locations from the skin's outer surface to the bone is also measured and described in Fig. 25(c). This information will be used in the other section to compute the depth from the skin layer to the surface of the bone and the gap between the shinbone and thigh bone.
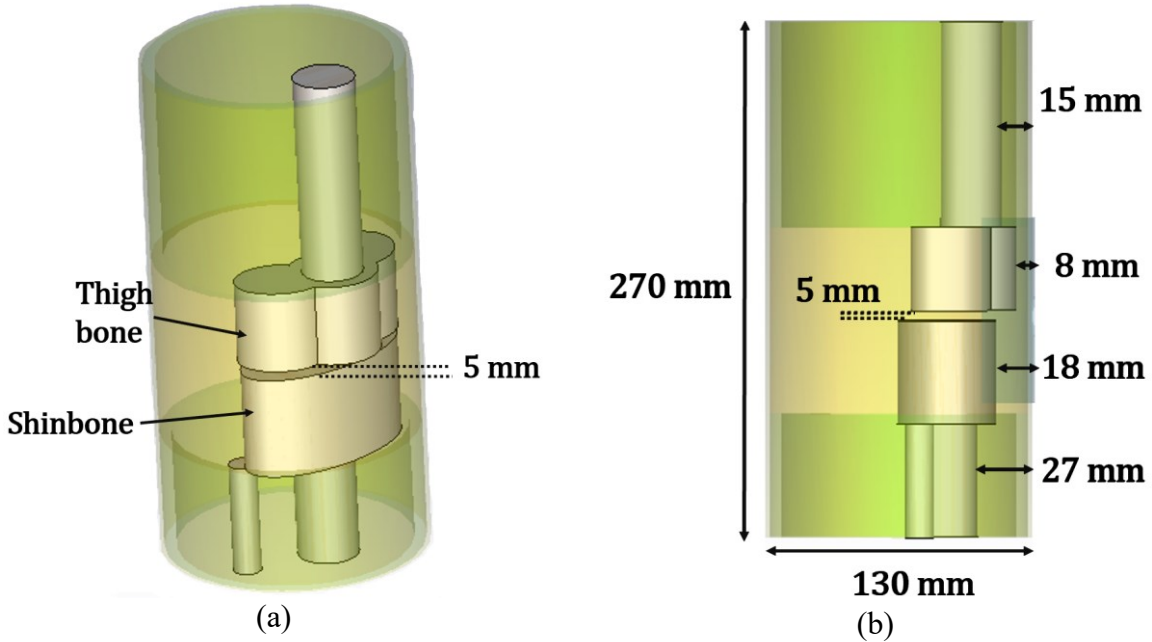
Figure 27. Simplified normal knee characteristics (5 cm gap between the thigh bone and shinbone)
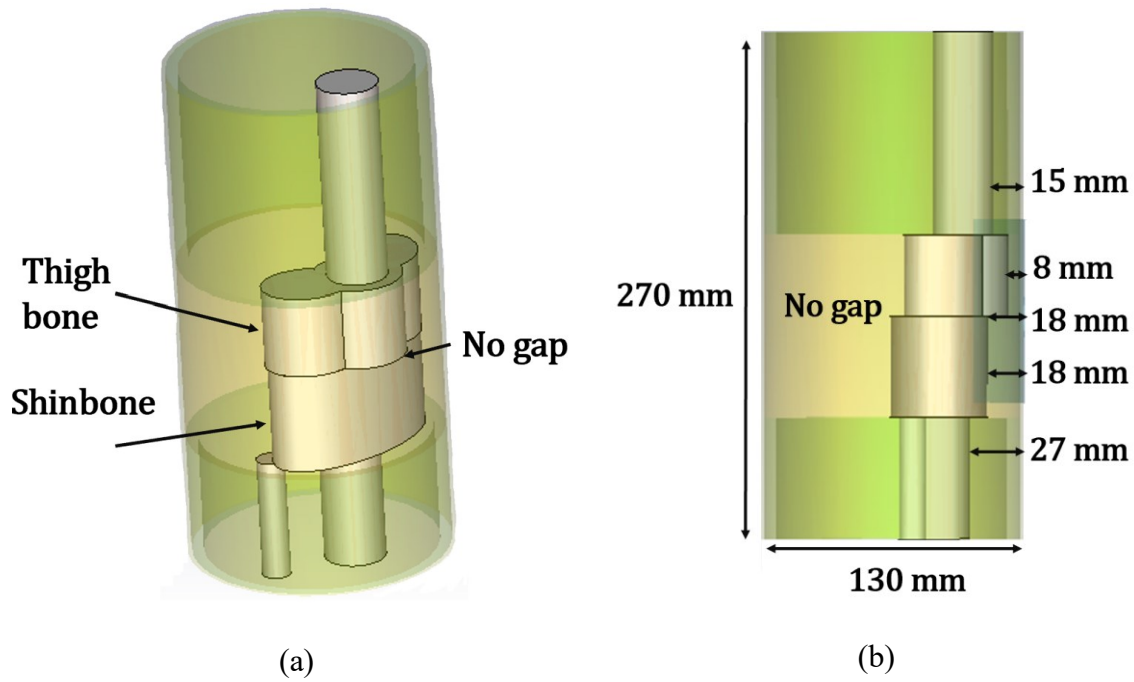
Figure 28. Simplified knee with osteoarthritis characteristics (No Gap between the thigh bone and shinbone)

Further, two simplified knees are modeled in CST to test the methodology more efficiently a) Normal knee and b) Knee with osteoarthritis. Fig.26 shows the graphical representation of the simplified human knee model. The dimensions of the knees are similar to that of the voxel knee model. The average skin and fat layer thickness are assigned as 2 mm and 6 mm, respectively. In the case of the normal knee, as shown in Fig. 27, the electrical properties of skin, fat, bone, and muscle layers are assigned as described in Table 24. Spacing of 5 mm is maintained between the shinbone and thigh bone for the normal knee. There is a gap between these bones for the healthy patient. On the other hand, relative permittivity values for knee with osteoarthritis, as shown in Fig.28, are assigned the same as the human knee voxel model, and there is no gap between the shinbone and thigh bone.

3.3 Experimental setup for knee imaging using SAR-focused microwave reflection tomography

A systemic experimental diagram for microwave knee imaging is shown in Fig.29. A pair of UWB Vivaldi antennas are mounted on the automatic shaft. The antenna pair can move from one end to another at a different position on the shaft. In order to create a linear array of transmitters and receivers, 25 locations are considered on the shaft. The system is cost-effective as only one pair of antennas is used, substituting 25 transmitters and 25 receivers. Moving the antenna's pair from one location to another synchronized with the transmitted and received pulses makes this system cost-effective. Further, the shaft is connected to the supporting bar connected to the motor. The motor is linked with the automatic measurement system that rotates at a step angle of 20º to

complete a full 360° in 18 motions. The motor is installed at the center of the rectangular box. The subject can be placed at the center and on the surface of the rectangular box.
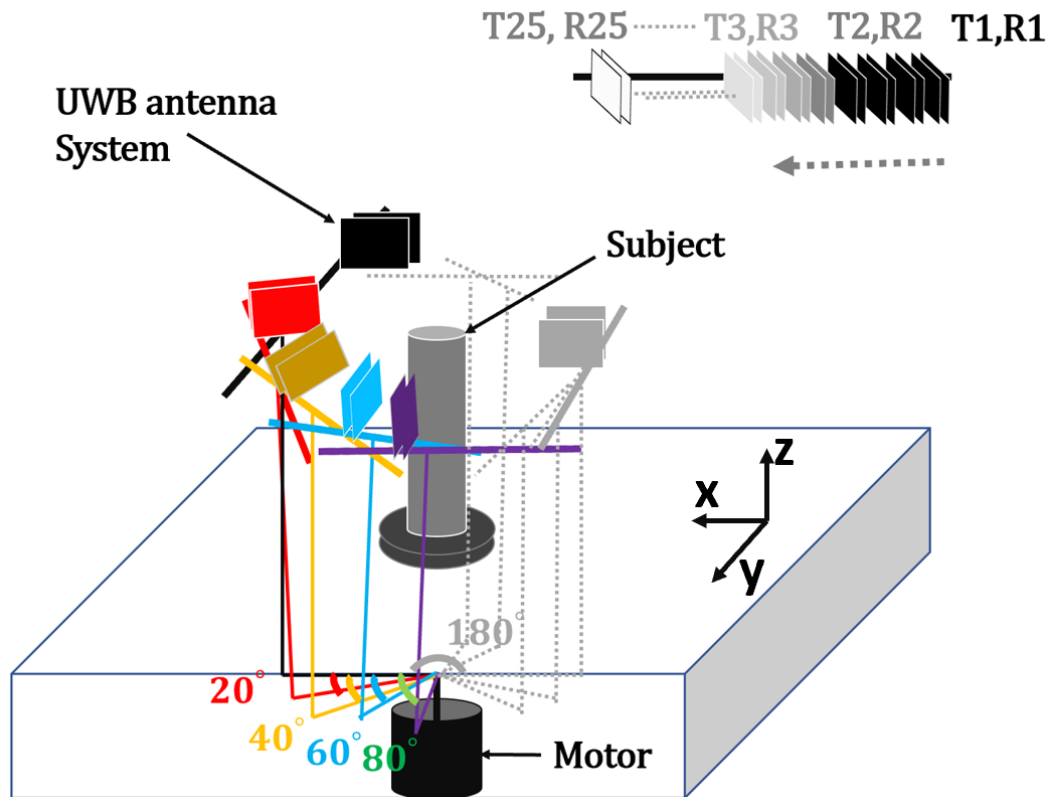
Figure 29. Experimental setup for knee imaging

3.4 Simulation setups for knee imaging

This section illustrates the microwave imaging techniques used to compute the gap between the thigh bone and shinbone. The most popular microwave technique used to image an object is the circular synthetic aperture radar (CSAR) [104]. In the CSAR measurement, the imaging is done by collecting an aperture of a specific slice of the object. The aperture consists of N locations, and at each location, data is collected. Once the data is collected using full-wave simulation, the image is reconstructed. Many algorithms can be used to obtain the reconstructed image. The most basic

algorithm that can be used is the global back-projection technique [105]. In this section, the analysis

(a)

(b)   (c)

Figure 30. (a) Cross-section view at the joint of the normal knee (b) reconstructed image(colored) and (c) reconstructed image (grayscale)

is first done on simplified models to demonstrate the proof of concept for CSAR imaging reconstruction, followed by the analysis of the human voxel model available in CST software. The normal knee and knee with osteoarthritis simplified models, as shown in Fig. 27 and Fig.28, respectively, are developed in CST Microwave Studio. The shapes are extended along the z-axis

in both directions by 13.5 cm. Simulations are used as the proof of concept because all the dimensions of the simplified knee models are very close to the human voxel knee model. The material properties for the simulated structures are assigned as discussed in section II. Fig.30 (a) shows the simplified shape of the normal knee depicting a cross-section of the knee joint. In the case of a normal knee, there is a gap between the thigh bone and shinbone. As a result, the cross-section cut of the knee joint is through a skinny muscle layer, not bone, and the image enclosed in a red rectangular box is used as the reference. The knee joint consisting of bones has an edge-to-edge dimension of 95 mm (in the horizontal direction) and 65 mm (in the vertical direction).

As shown in Fig. 30 (b), the reconstructed image is obtained through the CSAR imaging process. The purple, blue, and gray encircled area represents the curved edge of the thigh bone, and the outlines of the edges are very well obtained in the reconstructed image. Compared with the original bone, the estimated accuracy for the reconstructed edge-to-edge dimension of bone is within 5mm. The data also contain energy from other locations along the z-axis, due to which smearing is observed around the thigh bone in the reconstructed image. Fig.30 (c) represents the reconstructed cross-section image of a normal knee joint in grayscale format.

Further, the image of the knee joint of a simplified knee model with an osteoarthritis problem is reconstructed using the same technique. Fig.31 (a) shows the simplified shape of the knee with osteoarthritis depicting a cross-section of the knee joint. Since, there is no gap between the thigh bone and shinbone. As a result, the cross-section cut of the knee joint is through bone and its surrounding muscle layer. The cross-section image enclosed in a red rectangular box is used as the reference
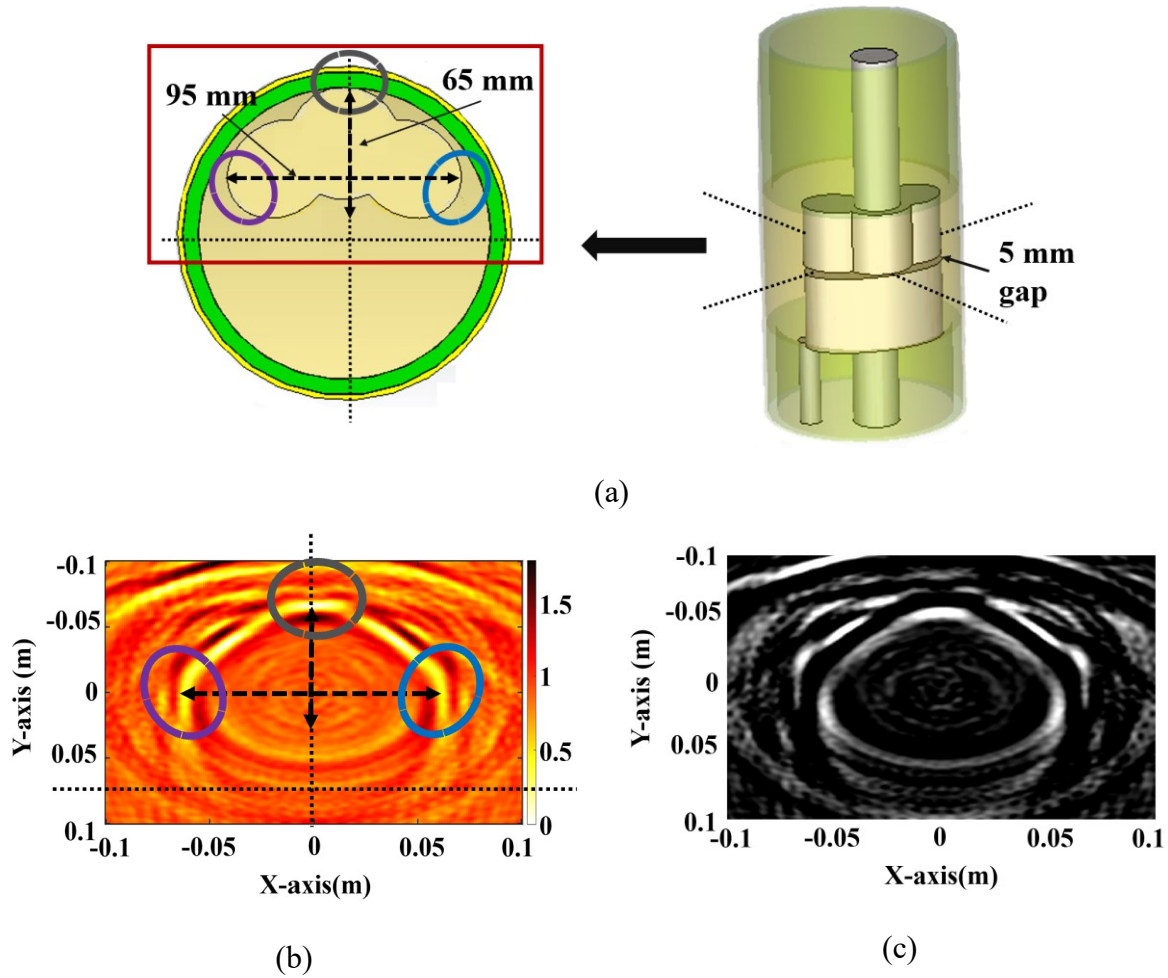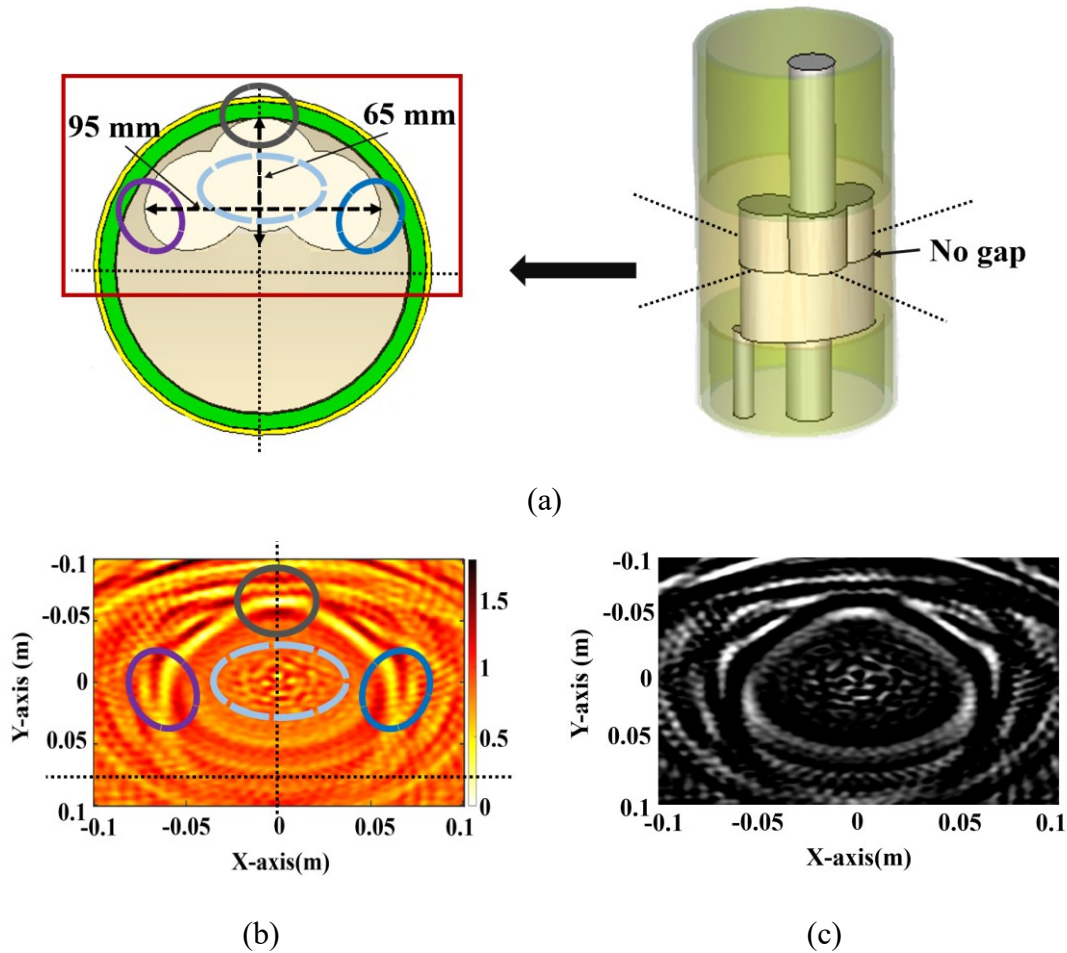
Figure 31. (a) Cross-section view at the joint of the knee with Osteoarthritis (b) reconstructed image(colored) and (c) reconstructed image (grayscale)

In the reconstructed image, as shown in Fig.32 (b), the purple, blue, and gray encircled area represents the outline of the curved edge of the thigh bone, and they are very well obtained in the reconstructed image. The area enclosed in light blue is the central part of the thigh bone and is also obtained in the reconstructed image. Here also, the estimated accuracy for the reconstructed edge-to-edge dimension of bone is within 5mm compared to the original bone. Fig.33 (c) represents the reconstructed cross-section image of a knee joint with osteoarthritis in grayscale format.
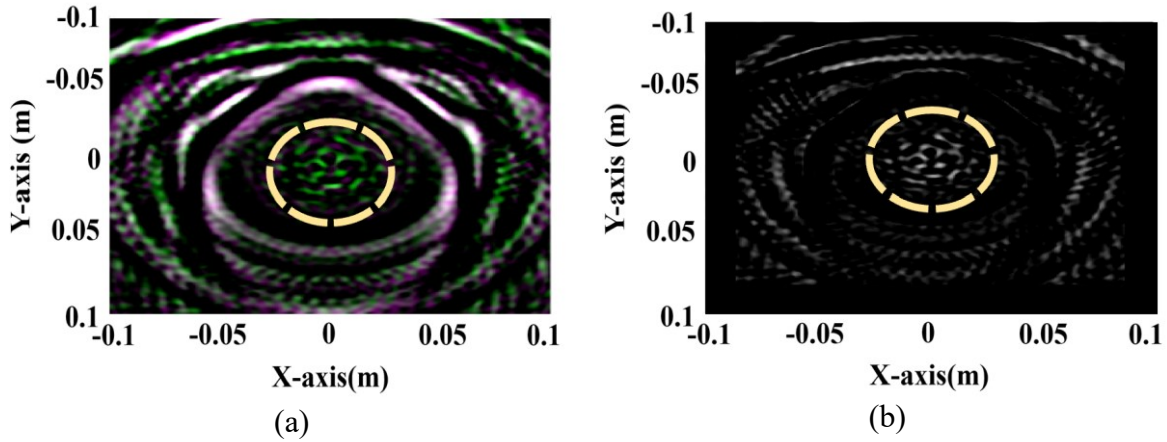
Figure 32. (a) Image registration of knee with osteoarthritis and normal knee (b) Subtracted image (grayscale)

The reconstructed images for the knee with osteoarthritis show similar results to the normal knee. However, the images are not identical, and there are differences. The normal knee and knee with osteoarthritis are registered over each other to prove the differences in the reconstructed grayscale image, as shown in Fig. 32 (a). Further, the subtraction of images is performed pixel-by-pixel along the x-axis and y-axis in MATLAB. It is observed that there are some remaining artifacts at the center of the reconstructed image encircled in a pale-yellow area. These artifacts are due to the knee bone in the osteoarthritis case as there is no gap between the thigh bone and shinbone.

Further, to demonstrate the CSAR technique for a more realistic scenario than the simplified models, we repeat the simulation for an accepted biological model known as Gustav, an adult man from the CST voxel family. The tissues are segmented, and the knee region is selected for imaging. The knee voxel is considered the case for osteoarthritis problems where there is no gap between the thigh bone and shinbone. The knee voxel model includes skin, fat, and bone layers, and their properties are assigned as discussed in Table 24. The muscle dielectric

permittivity is assigned a value of 82, which corresponds to the accumulation of synovial fluid around the knee joint.
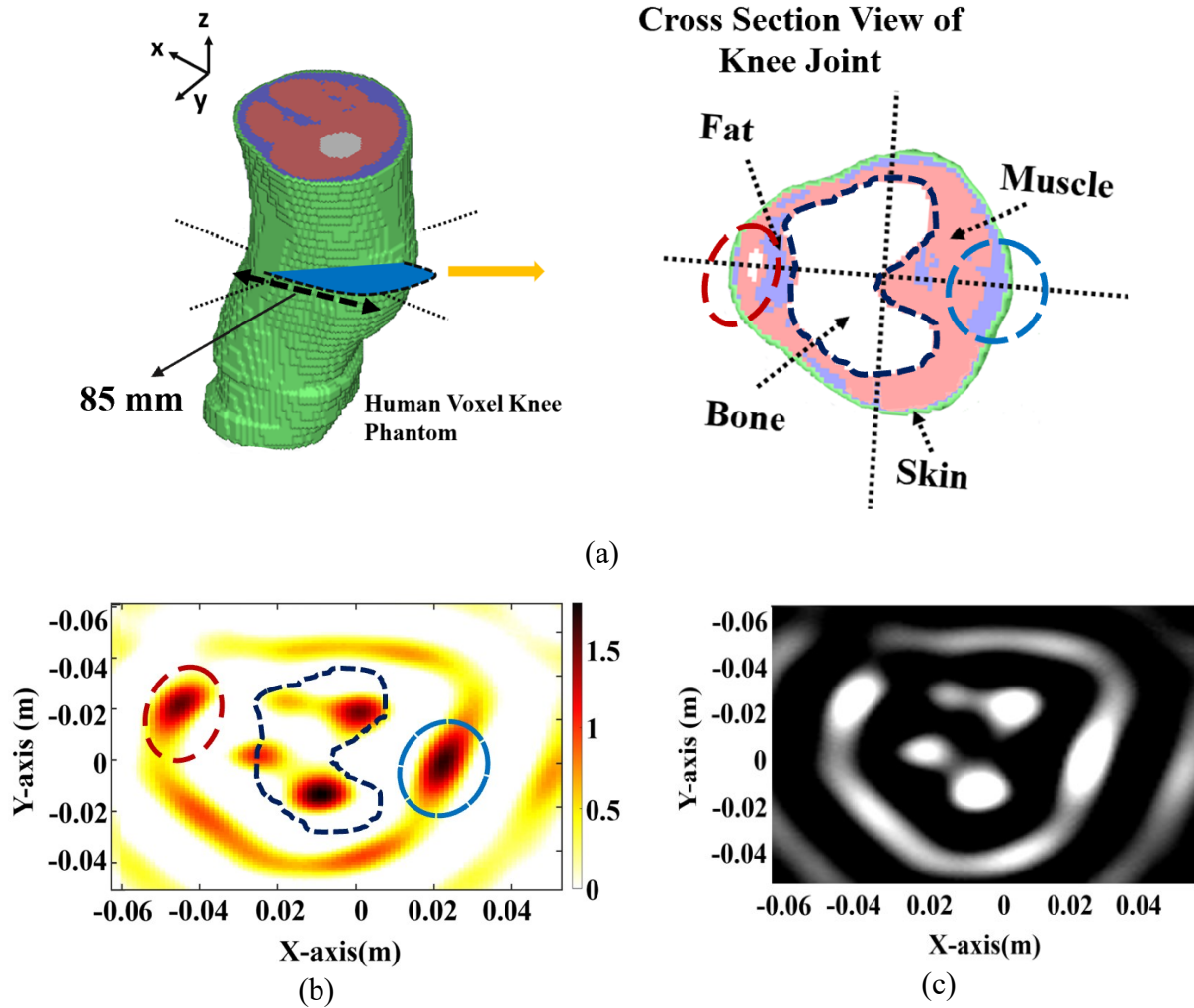
Figure 33. (a) Cross-section view of human voxel knee joint (b) reconstructed image(colored) and (c) reconstructed image (grayscale)

The entire knee is 27 cm in height and is included in the simulation. Fig. 33(a) shows the cross-section view of the knee joint at the height of the probe receiver and is used as the reference. Fig. 33(b) shows the reconstructed knee joint using the CSAR image reconstruction technique. The sky-blue encircled area in the reconstructed image is due to the fat tissue embedded in the

muscle layer. The difference in the permittivity of fat and muscle layer containing synovial fluid is high. As a result, the microwave energy is absorbed by muscle and skin layers but scattered by the low dielectric fat tissue and the bones. The navy blue and red encircled area represent the bones at the knee joint. It is observed that the outline of the knee joint bone structure is not adequately imaged and missing vital information by showing the single bone as two separate elongated bones.
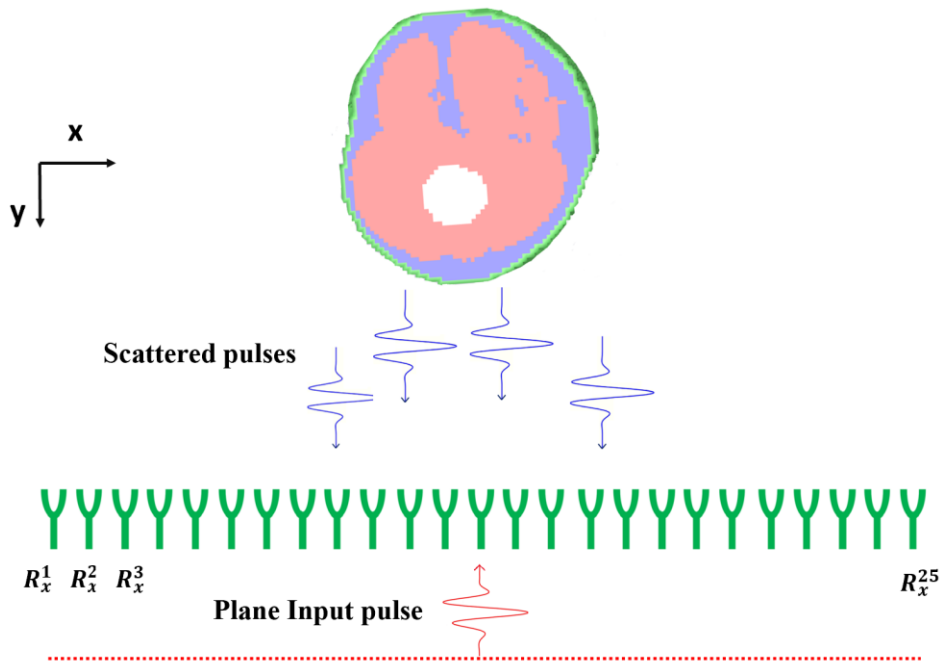
Figure 34. Simulation setup for voxel knee phantom in CST software

In order to obtain more details about the knee joint and image it more adequately, we proposed a new method known as SAR-focused microwave reflection tomography. Fig. 34 shows a scenario for SAR-focused microwave reflection tomography measurements for voxel knee imaging in the x-y plane. The plane wave of 3 cm pulse-spatial width is applied to the simulation with incident direction towards the knee joint. Twenty-five probes acting as receivers are placed

15cm away from the knee model and are spaced apart by 2cm, measuring the reflections for a 48cm span. Fig. 33 (a) shows the cross-section view of the knee joint and is used as the reference.
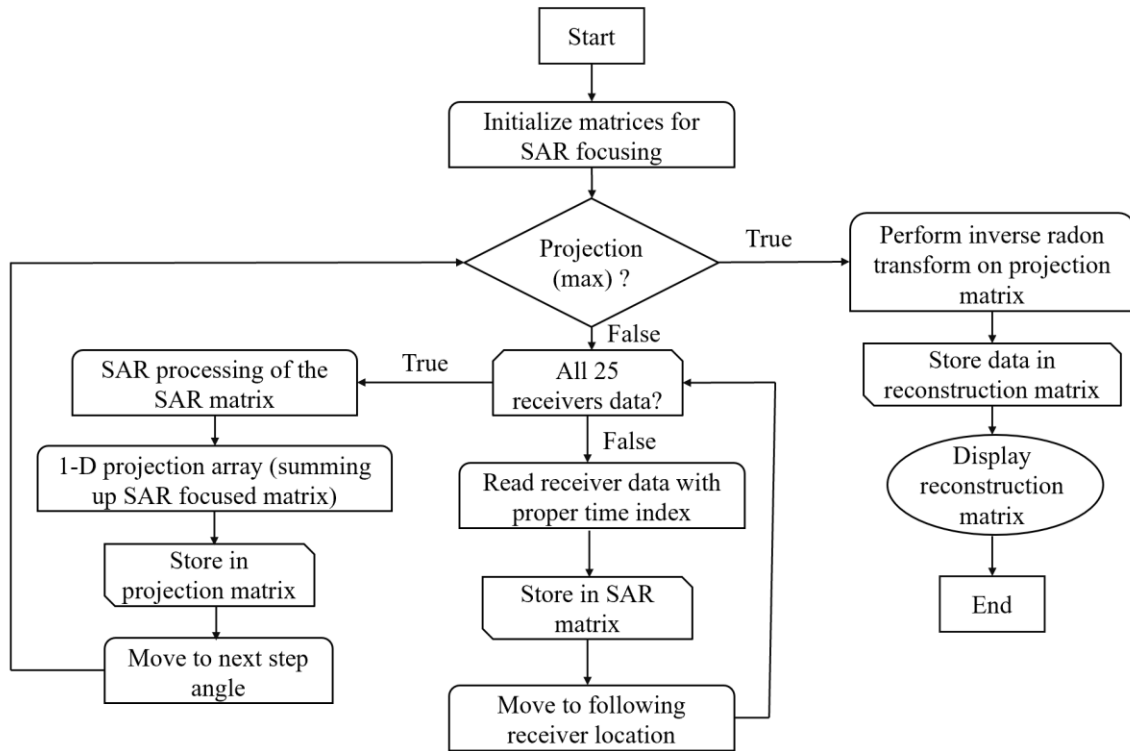
Figure 35. Flowchart of SAR focused microwave reflection tomography algorithm

When the plane wave is incident on the knee joint at a specific angle, it goes through scattering. The data collected by each receiver for each projection is recorded and is used for image reconstruction. Fig.36 (a) shows the reconstructed knee joint using SAR-focused reflection microwave tomography. The navy blue and red encircled area represent the bones at the knee joint. The reconstructed image shows the outlines of the bone structure quite well. The sky-blue encircled area in the reconstructed image is due to the fat tissue embedded in the muscle layer. The voxel knee model is not homogenous along the z-axis, and the SAR technique is only applied for the x-axis, so the reconstructed image also contains scattered energy from other z-axis locations. As a result, there is some smearing of the image around the location of the knee bones. Fig.36 (b)

shows the reconstructed image of the voxel knee with osteoarthritis(grayscale).
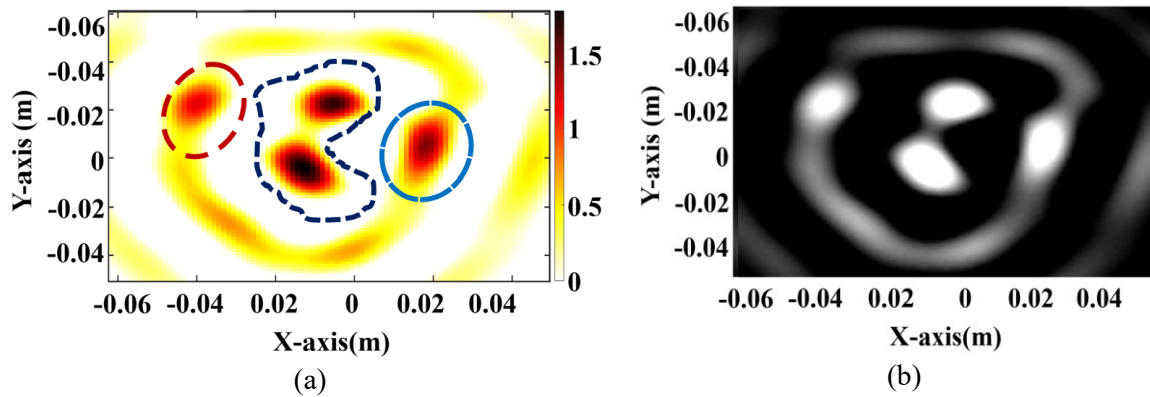
Figure 36. (a) SAR focused microwave reflection tomography reconstructed image(colored) and (b) reconstructed image (grayscale)

Since the image obtained by SAR-focused microwave tomography shows more important details of the knee joint than the CSAR method, the proposed technique can be used to image the main characteristics of the knee joint, and the reconstructed images can then be used to add context to other methods that can uncover the extent of the osteoarthritis.

3.5 Knee permittivity and depth computation using ultrawideband radar technique

UWB radar techniques can measure the properties of tissues such as skin, fat, muscle, ligament/tendon, and bone. The estimation of dielectric permittivity is associated with the reflected electromagnetic waves scattered by an object [106] [107] [108]. This section uses the UWB radar technique with a genetic algorithm to compute the knee muscle permittivity, depth from skin to the bone, and spacing between the thigh bone and shinbone. Fig.37 (a) and Fig.37 (b) show the

simulation setup for measuring knee permittivity and depth. A metal plate with a circular aperture of 2 cm is placed around the knee phantoms to precisely identify tissue properties in a specific area. The antenna system consisting of two Vivaldi antennas is located 5 cm from the metal plate. A Gaussian pulse of 100 ps with a normalized amplitude of 1 V is fed to the antenna system.

(a)   (b)
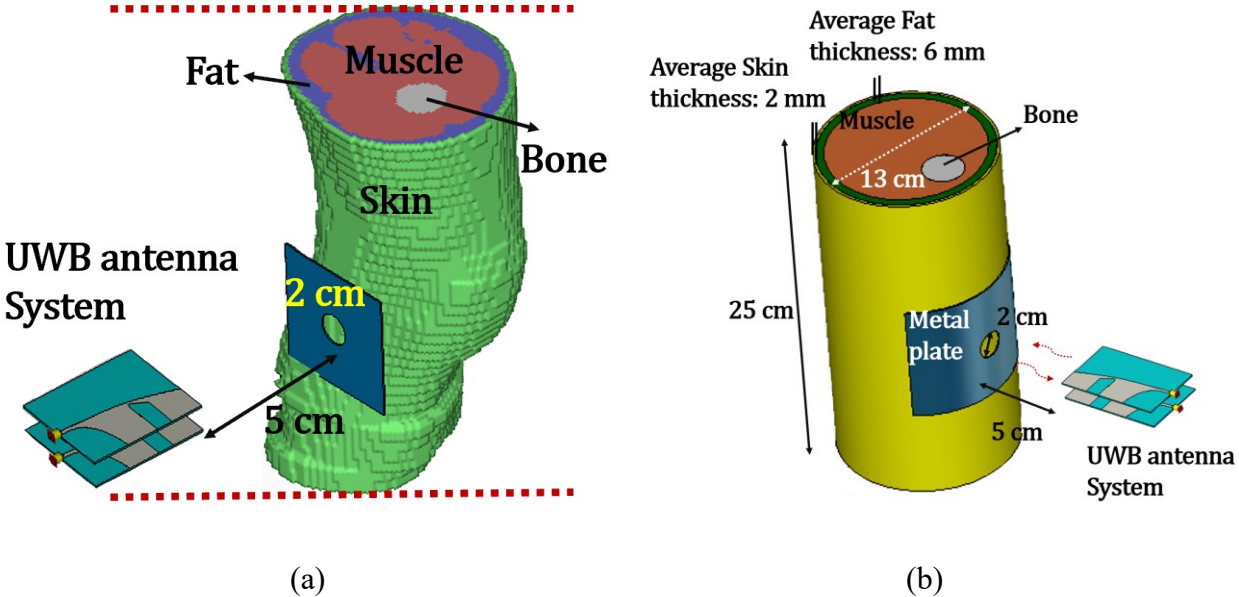
Figure 37. Simulation Setup for permittivity and depth computation for (a) Voxel knee phantom and (b) Simplified knee phantoms

Using the proposed technique, the permittivity of the muscle is analyzed at the knee joint, while to compute the depth from skin to bone and the gap between the thigh bone and shinbone, the antenna system is scanned on the knee at five different positions(P1-P5) as shown in figure 38.
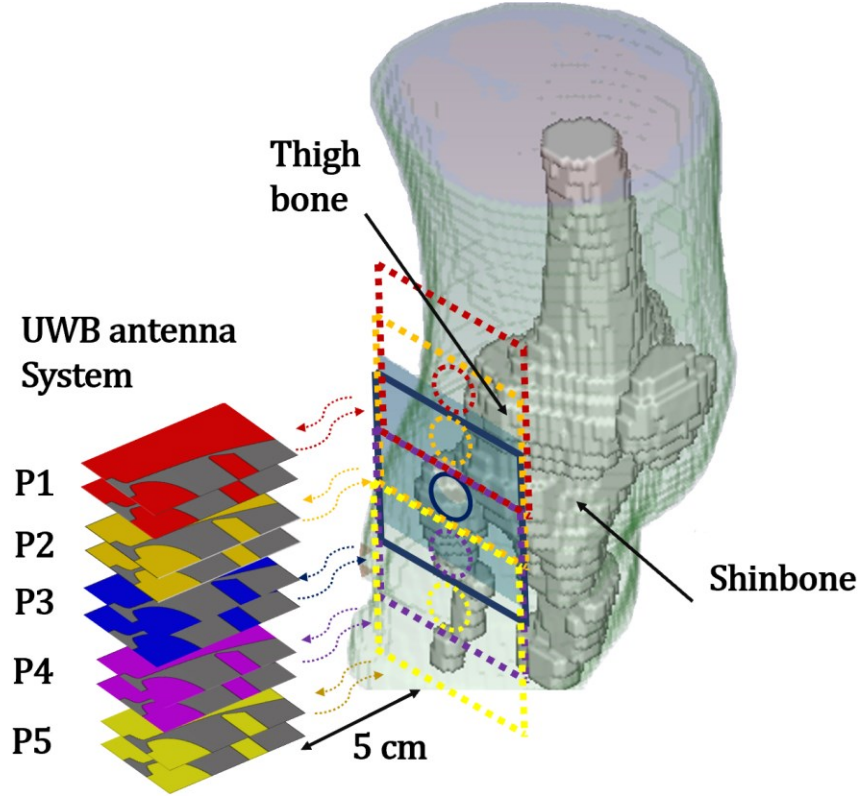
Figure 38. Representation of antenna scanning on human voxel knee from position 1- 5 to compute the permittivity and depth

The knee tissues can be represented as a multi-section transmission line, as shown in Fig.39. Around the knee joint for positions 2, 3, and 4, it can be considered as shown in Fig. 39 (a) as there is no fat layer present, while for positions 1 and 5, it can be shown as in Fig.39 (b). The theoretical input impedance for Positions 2, 3, and 4 can be calculated as follows:

The theoretical input impedance for Positions 2, 3, and 4 can be calculated as follows:

$$\Gamma_R = \frac{Z^{im1} - Z_a}{Z^{im1} + Z_a} \tag{3.1}$$

$$Z^{im1} = Z_S \frac{Z^{im2} + Z_s \tanh(\gamma_s d_s)}{Z_s + Z^{im2} \tanh(\gamma_s d_s)} \tag{3.2}$$
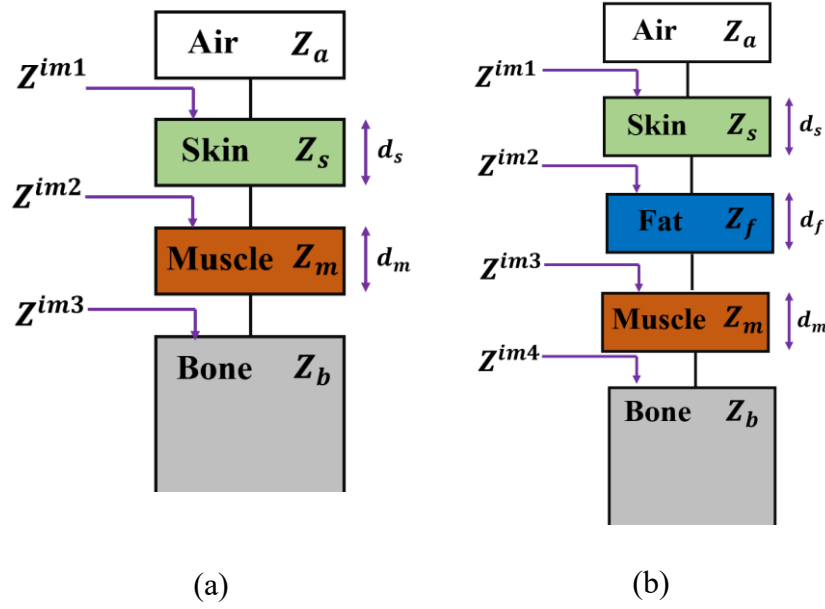
Figure 39. Knee tissues as a multi-section transmission line for a) Position 2,3 and 4 b) Position 1 and 5

$$Z^{im2} = Z_m \frac{Z^{im3} + Z_m \tanh(\gamma_m d_m)}{Z_m + Z^{im3} \tanh(\gamma_m d_m)} \tag{3.3}$$

$$Z^{im3} = Z_b = \frac{377}{\sqrt{\varepsilon_b}} \tag{3.4}$$

$$\gamma_s = j\frac{2\pi f \sqrt{\varepsilon_s}}{c}, \quad \gamma_m = j\frac{2\pi f \sqrt{\varepsilon_m}}{c} \tag{3.5}$$

where Z^{im1}, Z^{im2} and Z^{im3} are the input impedance of the skin, muscle, and bone layer. γ_s, d_s, Z_s and ε_s are the propagation constant, length, characteristic impedance, and the complex permittivity of the skin layer, respectively, whereas γ_m, d_m, Z_m and ε_m corresponds to the muscle layer properties. ε_b is the complex permittivity of the bone layer, and Z_b is the characteristic impedance of the bone layer, which is considered infinitely extended, so it is equivalent to Z^{im3}. c is the speed of light in a vacuum, f is the frequency of operation, Z_a is the characteristic impedance of air, and Γ_R is the complex reflection coefficient of the three-layer knee tissues. The

aim is to minimize the absolute difference between the measured frequency-dependent reflection coefficient and the corresponding theoretical value [109] and can be written as follows:

$$Q_0 = minimize\{||\Gamma_R (U)| - |\Gamma_{measured}||\} \qquad (3.6)$$

$$U = [\, d_s, \ \varepsilon_s, d_m\ , \varepsilon_m, \varepsilon_b\,] \qquad (3.7)$$

In Eq. (3.1), the complex reflection coefficient is a function of Z^{im1}, which is a function of $d_s, \ \varepsilon_s, d_m\ , \varepsilon_m, \varepsilon_b$. After achieving measurements and theoretical reflection coefficients, a genetic algorithm is applied to minimize Q_0 and to find unknowns in vector U. The genetic algorithm is coded with a maximum generation value of 10000, a cross-over rate of 50%, a population size of 400, and a migration rate of 20. The averaged complex permittivity, depth, and gap between the bones are computed over the frequency span of 4-9 GHz and shown in tables discussed further in this section. The same can be derived and computed for positions 1 and 5, where the fat layer is also present.

The proposed technique is tested for all three knee models: a) Voxel knee (osteoarthritis), b) knee (osteoarthritis), and c) normal knee. Fig. 40 (a) and Fig.41 (b) represent the antenna scanning scenario from positions 1 to 5 for normal knee and knee with osteoarthritis, respectively. As discussed in Table 24, the skin, fat, bone, and muscle complex permittivity for normal and voxel knee models are assigned with actual average human tissue properties.
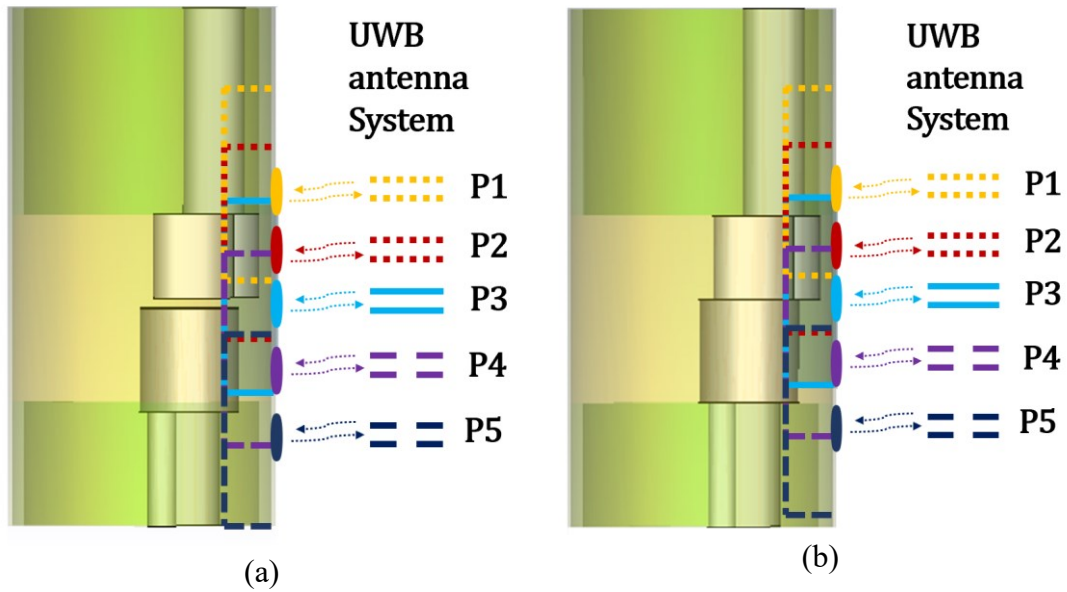
Figure 40. Representation of antenna scanning on a) Normal knee and b) Knee with osteoarthritis from position 1- 5 to compute the permittivity and depth

Table 25. Estimated average relative permittivity using the proposed technique and error calculations

Case	(True) ε_r	(Est) ε_r	Error
Voxel knee(Osteoarthritis)	82-0.13i	83.06-0.2i	1.29%
Knee(Osteoarthritis)	82-0.13i	84.40-0.25i	2.92%
Normal Knee	34.45-0.01i	33.55-0.12i	2.68%

The estimated average permittivity with error calculations of muscle and ligament/tendon tissue around the knee joint is summarized in Table 25. The error values for voxel knee (osteoarthritis) and knee (osteoarthritis) are 1.29% and 2.92%, respectively, showing promising results.
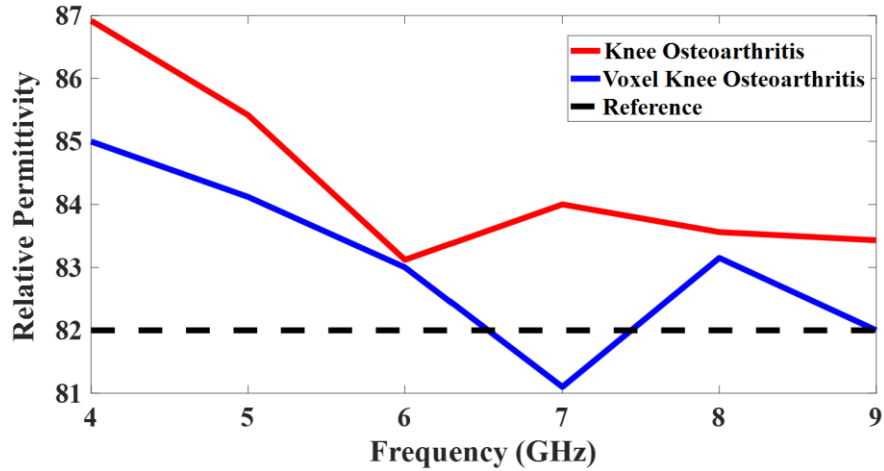
Figure 41. The plot of relative permittivity vs. frequency for simplified and voxel knee with osteoarthritis

Fig.41 shows the plot of relative permittivity variation with frequency for simplified and voxel knee models with osteoarthritis. In the normal knee case, when the permittivity is close to actual muscle permittivity, the error is estimated to be 2.68%. The plot of relative permittivity with respect to frequency is shown in Fig.42.
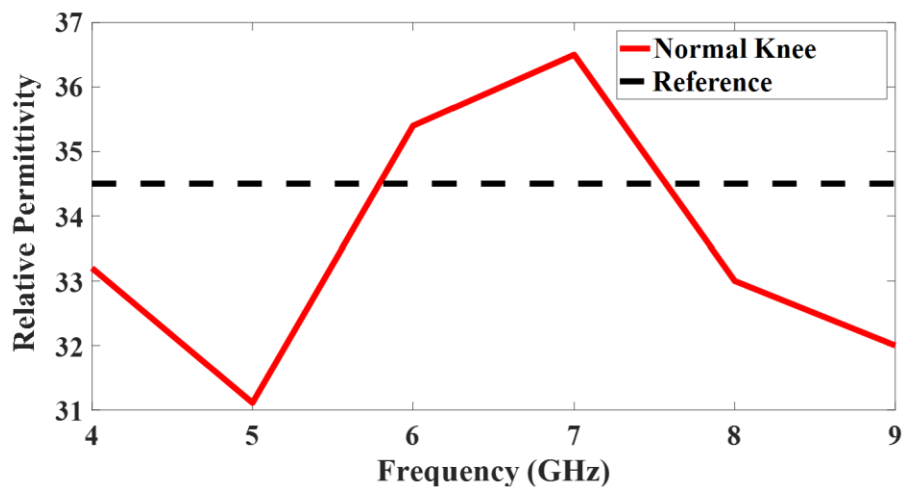
Figure 42. The plot of relative permittivity vs. frequency for normal knee joint

The depth from the skin to the bone and the gap between the thigh bone and shinbone is computed at five different positions (1-5). In the simulation model, there is no gap between the thigh bone and shinbone for the voxel knee (osteoarthritis) and knee model (osteoarthritis), and the distance from the skin to the bone is calculated as 14 mm and 18 mm, respectively.

Table 26. Estimated Depth using proposed technique and error calculations for voxel knee having osteoarthritis

Position	(True) (mm) d_1	(Est) (mm) d_3	Error	(True) (mm) d_1	(Est) (mm) d_3	Error
P1	21	19	9.52%	15	14.5	3.33%
P2	10.5	11.1	5.71%	8	7	12.5%
P3	14	13.5	3.57%	18	17	5.55%
P4	13	13	0%	18	17.5	2.77%
P5	27	25	7.40%	27	25	7.40%
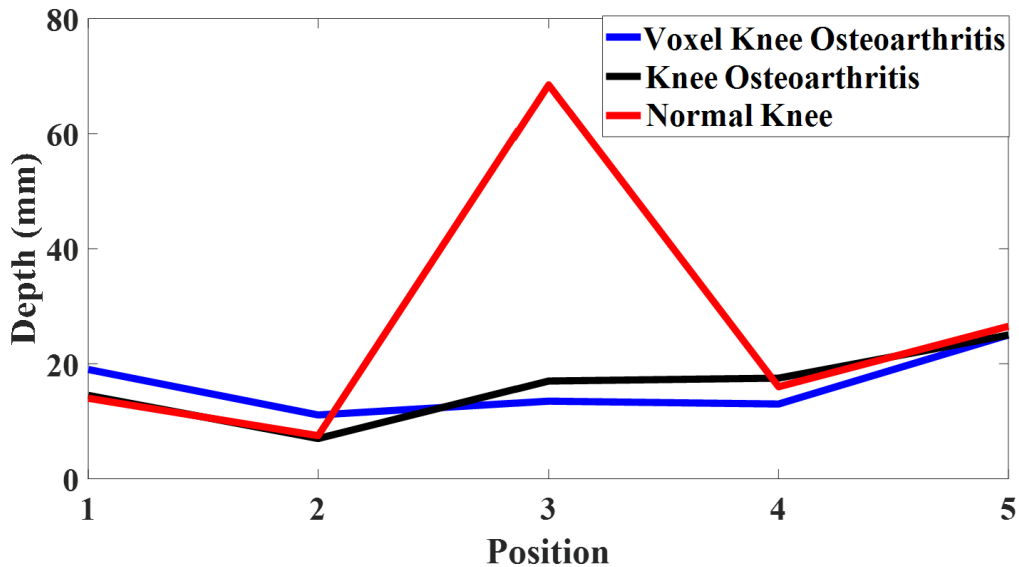
Figure 43. The plot of depth vs. position for all simplified and voxel knee cases

After scanning the antenna and applying the proposed technique, the estimated depth (in mm) for both osteoarthritis cases is illustrated in Table 26. The error for position 3 (knee joint) is around 3.57% and 5.55 % for the voxel and simplified knee model with osteoarthritis. The total depth is the addition of the unknown vectors d_s and d_m found using the proposed technique for positions 2,3 and 4, where it is the addition of unknown vectors d_s , d_f and d_m for positions 1 and 5. In a normal knee case, when there is a gap between the thigh bone and shinbone, the measured signal received is the reflection from the skin and muscle layer only. The signal enters the skin layer, then the muscle layer, and goes through the gap between the bones to reflect again from the muscle-skin interface. As a result, in the case of the normal knee, a spike of a value of 68.5 mm is achieved. Fig.43 shows the depth (in mm) for all the knee cases at positions 1-5. It can be concluded that when the patient is healthy, there is some gap between the thigh and shinbone at the knee joint, and the permittivity of muscle around the knee is close to actual muscle permittivity.

The analysis of permittivity and depth computation for all three cases concludes that the UWB radar technique equipped with a genetic algorithm can uncover the additional aspects of osteoarthritis. Hence, combined results of microwave imaging, permittivity, and depth calculation can provide vital information about the knee osteoarthritis of the patient.

3.6 Conclusion

This chapter proposes a non-invasive ultra-wideband microwave imaging technique to study knee osteoarthritis. The proposed method was validated using full-wave simulations CST software. First, simplified knee models are created in simulation software and studied. Then, the same setup

is also used to study the voxel knee model. The image obtained using SAR-focused microwave reflection tomography was comparable to the actual cross-section image of the voxel knee joint. Subsequently, the permittivity and depth computation for all the models are evaluated and analyzed. The results agree with the reference values of electrical properties and depth from skin to bone within 10 % for all the cases. In the case of osteoarthritis, the dielectric constant of muscle is close to 82 due to the accumulation of synovial fluid, and there is no gap between the thigh bone and shinbone. By analyzing combined results of microwave imaging, permittivity, and depth calculation, it is possible to conclude the knee osteoarthritis problem in the person. Hence, this study showed the feasibility of the proposed technique to determine knee osteoarthritis in the human body.

Chapter 4

Conclusion and Future work

4.1 Conclusion

In this thesis, the feasibility of the UWB radar technique to analyze obesity and knee osteoarthritis is established and studied. The capability of the UWB radar system to determine the brown and white fat in the body depending on their percentage is investigated through several simulations and experimental measurements. The knee osteoarthritis study using a UWB microwave imaging system based on the change in muscle permittivity and the gap between the thigh bone and shinbone is scrutinized. It was shown that the UWB radars are safe, cost-effective, and non-invasive techniques for biomedical applications.

4.2 Future Work

The techniques discussed in this thesis provide an alternative approach for determining obesity and knee osteoarthritis through permittivity and imaging data. In the future, the fat analysis can be

improved by imaging the white and brown adipose tissues as they have permittivity differences. In case of osteoarthritis, multiple images at different locations along the knee joint can be reconstructed to obtain a 3D tomographic image that can effectively analyze the gap between the thigh bone and shinbone. The resolution of the images obtained can be improved further if a 30 picosecond pulse is used in the simulation. The two techniques can be clinically tested on humans worldwide to evaluate the practicality of the UWB radar system for biomedical applications.

References

[1]   DA. Zieba, W. Biernat, J. Barć, "Roles of leptin and resistin in metabolism, reproduction, and leptin resistance," *Domest Anim Endocrinol,* vol. 73:106472, 2020.

[2]   H. Tilg, A. Moschen, "Adipocytokines: mediators linking adipose tissue, inflammation and immunity," *Nat Rev Immunol,* vol. 6, no. 10, p. 772–783, 2006.

[3]   M. C. Leoni, C. Valsecchi, M. Mantelli, L. Marastoni, C. Tinelli, A. Marchi, & A. Castellazzi, "Impact of child obesity on adipose tissue physiology: assessment of adipocytokines and inflammatory cytokines as biomarkers of obesity," *Pediatric reports,* vol. 2, no. 2, pp. 62-66, 2010.

[4]   A. M. Cypess, & C. R. Kahn, "Brown fat as a therapy for obesity and diabetes," *Current opinion in endocrinology, diabetes, and obesity,* vol. 17, no. 2, pp. 143-149, 2010.

[5]   V. Ouellet, S. M. Labbé, D. P. Blondin, S. Phoenix, B. Guérin, F. Haman, E. E. Turcotte, D. Richard, & A. C. Carpentier, "Brown adipose tissue oxidative metabolism contributes to energy expenditure during acute cold exposure in humans," *The Journal of Clinical Investigation,* vol. 122, no. 2, pp. 545-552, 2012.

[6]   B. Cannon, J. Nedergaard, "Yes, even human brown fat is on fire!," *The Journal of Clinical Investigation,* vol. 122, no. 2, pp. 486-489, 2012.

[7]   J. van der Kruk *et al*., "GPR full-waveform inversion, recent developments, and future opportunities," , 2018, pp. 1-6, doi: 10.1109/ICGPR.2018.8441667.," in *17th International Conference on Ground Penetrating Radar (GPR)*, Rapperswil, 2018.

[8]   J. H. Bradford, J. T. Harper , and J. Brown , "Complex Dielectric Permittivity Measurements from Ground-penetrating Radar Data to Estimate Snow Liquid Water Content in the Pendular Regime," *Water Resources Research ,* vol. 46, no. 2, 2010.

[9]   B. Mohammed, K. Bialkowski, and A. Abbosh, "Radar-based time-domain head imaging using database of effective dielectric constant," *Electron. Lett.,* vol. 51, no. 20, pp. 1574-1576, 2015.

[10]   J.D. Redman, et al., "Field studies of GPR air launched surface reflectivity measurements of soil water content," *Proceedings of the Society of Photo Optical Instrumentation Engineers (SPIE),* vol. 4758, pp. 156-161, 2002.

[11]   L. Weihermüller, et al., "Mapping the spatial variation of soil water content at the field scale with different ground penetrating radar techniques," *Journal of Hydrology,* vol. 340, no. 3, pp. 205-216, 2007.

[12]   E. Alipoor, M.J. Hosseinzadeh-Attar, M. Rezaei, S. Jazayeri, & M. Chapman, "White adipose tissue browning in critical illness: A review of the evidence, mechanisms and future perspectives," *Obesity Reviews,* vol. 21, no. 12, 2020.

[13]   . Yiallourides and P. A. Naylor, "Time-Frequency Analysis and Parameterisation of Knee Sounds for Non-Invasive Detection of Osteoarthritis," *IEEE Transactions on Biomedical Engineering,* vol. 68, no. 4, pp. 1250-1261, 2021.

[14]   R. A. Bloomfield, M. C. Fennema, K. A. McIsaac and M. G. Teeter, "Proposal and Validation of a Knee Measurement System for Patients With Osteoarthritis," *IEEE Transactions on Biomedical Engineering,* vol. 66, no. 2, pp. 319-326, 2019.

[15]   Y. Wang et al., "Learning From Highly Confident Samples for Automatic Knee Osteoarthritis Severity Assessment: Data From the Osteoarthritis Initiative," *IEEE Journal of Biomedical and Health Informatics,* vol. 26, no. 3, pp. 1239-1250, 2022.

[16]   S. Y. Nam et al., "Imaging strategies for tissue engineering applications," *Tissue engineering. Part B, Reviews,* vol. 21, no. 1, pp. 88-102, 2015.

[17] D. O'Loughlin, M. O'Halloran, B. M. Moloney, M. Glavin, E. Jones and M. A. Elahi, "Microwave Breast Imaging: Clinical Advances and Remaining Challenges," *IEEE Transactions on Biomedical Engineering,* vol. 65, no. 11, pp. 2580-2590, Nov. 2018.

[18] W. Shao, A. Edalati, T. R. McCollough and W. J. McCollough, "A Phase Confocal Method for Near-Field Microwave Imaging," *IEEE Transactions on Microwave Theory and Techniques,* vol. 65, no. 7, pp. 2508-2515, July 2017.

[19] D. Oloumi, J. Ting and K. Rambabu, "Design of Pulse Characteristics for Near-Field UWB-SAR Imaging," *IEEE Transactions on Microwave Theory and Techniques,* vol. 64, no. 8, pp. 2684-2693, Aug. 2016.

[20] Z. Liu, N. Bayat and P. Mojabi, "On the Use of Absorbing Metasurfaces in Microwave Imaging," *IEEE Transactions on Antennas and Propagation,* vol. 69, no. 12, pp. 9026-9031, Dec. 2021.

[21] M. T. Bevacqua and R. Scapaticci, "A Compressive Sensing Approach for 3D Breast Cancer Microwave Imaging With Magnetic Nanoparticles as Contrast Agent," *IEEE Transactions on Medical Imaging,* vol. 35, no. 2, pp. 665-673, Feb. 2016.

[22] T. Tarvainen, A. Pulkkinen, B. T. Cox, J. P. Kaipio and S. R. Arridge, "Bayesian Image Reconstruction in Quantitative Photoacoustic Tomography," *IEEE Transactions on Medical Imaging,* vol. 32, no. 12, pp. 2287-2298, Dec. 2013.

[23] S. Zhang, Y. Liu, X. Li and G. Bi, "Bayesian High Resolution Range Profile Reconstruction of High-Speed Moving Target From Under-Sampled Data," *IEEE Transactions on Image Processing,* vol. 29, pp. 5110-5120, 2020.

[24] J. Xiang, Z. Chen, Y. Dong and Y. Yang, "Image Reconstruction for Multi-frequency Electromagnetic Tomography based on Multiple Measurement Vector Model," in *2020 IEEE International Instrumentation and Measurement Technology Conference (I2MTC)*, 2020.

[25] V. T. Vu, T. K. Sjogren and M. I. Pettersson, "On Synthetic Aperture Radar Azimuth and Range Resolution Equations," *IEEE Transactions on Aerospace and Electronic Systems,* vol. 48, no. 2, pp. 1764-1769, April 2012.

[26] S. Kim, S. Ostlund, and G. Yu, "Fourier analysis of multi-frequency dynamical systems," *Physica D Nonlinear Phenomena,* vol. 31, no. 1, p. 117–126, 1988.

[27] S. Romanenko, R. Begley, AR. Harvey, L. Hool, VP. Wallace, "The interaction between electromagnetic fields at megahertz, gigahertz and terahertz frequencies with cells, tissues and organisms: risks and potential," *J R Soc Interface,* vol. 14, no. 137, Dec. 2017.

[28] S. Mukherjee, L. Udpa, S. Udpa, E. J. Rothwell and Y. Deng, "A Time Reversal-Based Microwave Imaging System for Detection of Breast Tumors," *IEEE Transactions on Microwave Theory and Techniques,* vol. 67, no. 5, pp. 2062-2075, 2019.

[29] M. Ostadrahimi, P. Mojabi, A. Zakaria, J. LoVetri and L. Shafai, "Enhancement of Gauss–Newton Inversion Method for Biological Tissue Imaging," *IEEE Trans. Microw. Theory Techn.,* vol. 61, no. 9, pp. 3424-3434, 2013.

[30] Xu Li, E. J. Bond, B. D. Van Veen and S. C. Hagness, "An overview of ultra-wideband microwave imaging via space-time beamforming for early-stage breast-cancer detection," *IEEE Antennas and Propagation Magazine,* vol. 47, no. 1, pp. 19-34, 2005.

[31] H. Song et al., "Detectability of Breast Tumors in Excised Breast Tissues of Total Mastectomy by IR-UWB-Radar-Based Breast Cancer Detector," *IEEE Transactions on Biomedical Engineering,* vol. 66, no. 8, pp. 2296-2305, 2019.

[32] . Kurrant, J. Bourqui, C. Curtis and E. Fear, "Evaluation of 3-D Acquisition Surfaces for Radar-Based Microwave Breast Imaging," *IEEE Transactions on Antennas and Propagation,* vol. 63, no. 11, pp. 4910-4920, Nov. 2015.

[33] E. C. Fear, J. Bourqui, C. Curtis, D. Mew, B. Docktor and C. Romano, "Microwave Breast Imaging With a Monostatic Radar-Based System: A Study of Application to Patients,"

IEEE Transactions on Microwave Theory and Techniques, vol. 61, no. 5, pp. 2119-2128, May 2013.

[34] O. Mahdiyar, M. A. Pourmina, A. H. Mazinan, M. N. Moghaddasi, "A New Concept of High-Resolution UWB Microwave Imaging System (UWB-MIS) Using Waveform-Diversity for Breast Cancer Applications," *Radar,* vol. 8, no. 2, pp. 121-129, 2020.

[35] M.T.Islam , M.Z. Mahmud, M.T. Islam *et al.*, "A Low Cost and Portable Microwave Imaging System for Breast Tumor Detection Using UWB Directional Antenna array," *Sci Rep,* vol. 9: 15491, 2019.

[36] D. Oloumi, R. S. C. Winter, A. Kordzadeh, P. Boulanger and K. Rambabu, "Microwave Imaging of Breast Tumor Using Time-Domain UWB Circular-SAR Technique," *IEEE Transactions on Medical Imaging,* vol. 39, no. 4, pp. 934-943, April 2020.

[37] J.-H. Zhang, "Artificial synovial fluid," in *Encyclopedia of Tribology,Q. J. Wang and Y.-W. Chung Eds.*, Boston, MA, USA, Springer, 2013, p. 110–113.

[38] "IT'IS. Human models. [Online]. Available: itis.swiss/virtual-population/ virtual-population/overview/".

[39] M. Hämäläinen, L. Mucchi, S. Caputo, L. Biotti, L. Ciani, D. Marabissi and G. Patrizi, "Ultra-Wideband Radar-Based Indoor Activity Monitoring for Elderly Care Sensors," Vols. 21,3158, 2021.

[40] A. Bhattacharjee, A. Bhawal, A. Karmakar, A. Saha, and D.Bhattacharya, "Vivaldi antennas: A historical review and current state of art," *International Journal of Microwave and Wireless Technologies,* vol. 13, no. 8, pp. 833-850, 2021.

[41] S. Singh, Q. Liang , D. Chen et al., "Sense through wall human detection using UWB radar," *J Wireless Com Network,* vol. 20, 2011.

[42] C. H. Lee, Y. J. Kang, J. Bae, S. W. Lee, J. Shin and J. W. Jung, "Moving object classifier based on UWB radar signal," in *2013 International Conference on Wireless Information Networks and Systems (WINSYS)*, 2013.

[43] X. Liang, J. Deng, H. Zhang, and T. A. Gulliver, "Ultra-Wideband Impulse Radar Through-Wall Detection of Vital Signs," *Sci Rep.,* vol. 8, no. 1, Sep. 2018.

[44] E. Zaikov, J. Sachs, M. Aftanas, and R. Jana, "Detection of trapped people by UWB radar," in *German Microwave Conference (GeMIC)*, 2008.

[45] D. Y. Cho, and S. H., "Indoor Positioning and Body Direction Measurement System Using IR-UWB Radar," in *2018 19th International Radar Symposium (IRS)*, 2018.

[46] M. Džunda, P. Dzurovčin, P. Kaľavský, P. Korba, Z. Cséfalvay, M. Hovanec, "The UWB Radar Application in the Aviation Security Systems," *Applied Sciences,* vol. 11, no. 10, pp. 45-56, 2021.

[47] B. Gupta, D. Valente, E. Cianca and R. Prasad, "FM-UWB for radar and communications in medical applications," in *2008 First International Symposium on Applied Sciences on Biomedical and Communication Technologies*, 2008.

[48] D. Oloumi, A. Bevilacqua and M. Bassi, "UWB Radar for High Resolution Breast Cancer Scanning: System, Architectures, and Challenges," in *2019 IEEE International Conference on Microwaves, Antennas, Communications and Electronic Systems (COMCAS)*, 2019.

[49] J.L. Prince and J.M. Links, Medical Imaging Signals and Systems, Pearson Education, 2014.

[50] H. Su et al., "Fiber-Optic Force Sensors for MRI-Guided Interventions and Rehabilitation: A Review," *IEEE Sensors Journal,* vol. 17, no. 7, pp. 1952-1963, April 2017.

[51] S. Kathiravan, and J. Kanakaraj, "A Review on Potential Issues and Challenges in MR Imaging," *The Scientific World Journal,* vol. 10, 2013.

[52] B. Ihnatsenka, and A. P. Boezaart, "Ultrasound: Basic understanding and learning the language," *International journal of shoulder surgery,* vol. 4, no. 3, pp. 55-62, 2010.

[53] G. Wang, A. Rahmim and R. N. Gunn, "PET Parametric Imaging: Past, Present, and Future," *IEEE Transactions on Radiation and Plasma Medical Sciences,* vol. 4, no. 6, pp. 663-675, Nov. 2020.

[54] M. Sabel, and H. Aichinger, "Recent developments in breast imaging," *Phys. Med. Biol.,* vol. 41, p. 315–336, 1996.

[55] A. T. Kessler, and A. A. Bhatt, "Brain tumour post-treatment imaging and treatment-related complications," *Insights into imaging,* vol. 9, no. 6, p. 1057–1075, 2018.

[56] A. C. Kak, and M. Slaney, Principles of Computerized Tomographic Imaging, Ch. 8, IEEE Press, 1988.

[57] P. Störchle, W. Müller, M. Sengeis. et al., "Measurement of mean subcutaneous fat thickness: eight standardised ultrasound sites compared to 216 randomly selected sites," *Sci Rep,* vol. 8, no. 1, pp. 162-168, 2018.

[58] D. A. Pollacco, L. Farina, P. S. Wismayer, L. Farrugia and C. V. Sammut, "Characterization of the dielectric properties of biological tissues and their correlation to tissue hydration," *IEEE Transactions on Dielectrics and Electrical Insulation,* vol. 25, no. 6, pp. 2191-2197, Dec. 2018.

[59] M. Savazzi, J. M. Felício, J. R. Costa, C. A. Fernandes, and R. C. Conceição, "Study of Freezing and Defrosting Effects on Complex Permittivity of Biological Tissues," *IEEE Antennas and Wireless Propagation Letters,* vol. 20, no. 12, pp. 2210-2214, Dec. 2021.

[60] S. Sarjoghian, Y. Alfadhl, X. Chen, and C. G. Parini, "A 3-D-Printed High-Dielectric Materials-Filled Pyramidal Double-Ridged Horn Antenna for Abdominal Fat Measurement System," *IEEE Transactions on Antennas and Propagation,* vol. 69, no. 1, pp. 64-73, Jan. 2021.

[61] E. Porter, A. L. Gioia, A. Santorelli, and M. O'Halloran, "Modeling of the dielectric properties of biological tissues within the histology region," *IEEE Transactions on Dielectrics and Electrical Insulation,* vol. 24, no. 5, pp. 3290-3301, Oct. 2017.

[62] Z. Peng, J. Hwang, and M. Andriese, "Maximum Sample Volume for Permittivity Measurements by Cavity Perturbation Technique," *IEEE Transactions on Instrumentation and Measurement,* vol. 63, no. 2, pp. 450-455, Feb. 2014.

[63] F.G. Awan, N.A. Sheikh, S.A. Qureshi & N.M. Sheikh, "Implementation of Cavity Perturbation Method for Determining Relative Permittivity of Non Magnetic Materials," *Mehran University Research Journal of Engineering and Technology,* vol. 36, no. 2, pp. 289-298, 2017.

[64] B. Karki, H. Wi, A. McEwan, H. Kwon, T. I. Oh, E. J. Woo and J. K. Seo, "Evaluation of a multi-electrode bioimpedance spectroscopy tensor probe to detect the anisotropic conductivity spectra of biological tissues," *Measurement Science and Technology,* vol. 25, no. 7, 2014.

[65] A. Ramos, and P. Bertemes-Filho, "Numerical sensitivity modeling for the detection of skin tumors by using tetrapolar probe," *Electromagn Biol Med.,* vol. 30, no. 4, pp. 235-245, 2011.

[66] H. Elmajid, J. Terhzaz, H. Ammor,M. Chaibi, & A.M. Sánchez, "A new method to determine the complex permittivity and complex permeability of dielectric materials at X-band frequencies," *International journal of microwave and optical technology,* vol. 10, no. 1, pp. 34-39, 2015.

[67] J. Roelvink, S. Trabelsi, and S. O. Nelson, "Measuring the Complex Permittivity Tensor of Uniaxial Biological Materials With Coplanar Waveguide Transmission Line," *IEEE Microwave and Wireless Components Letters,* vol. 24, no. 11, pp. 811-813, Nov. 2014.

[68] R A. Mirbeik-Sabzevari, R. Ashinoff, and N. Tavassolian, "Ultra-Wideband Millimeter-Wave Dielectric Characteristics of Freshly Excised Normal and Malignant Human Skin Tissues," *IEEE Trans Biomed Eng.,* vol. 65, no. 6, pp. 1320-1329, 2018.

[69] T. Karacolak, R. Cooper, E. S. Unlu, and E. Topsakal, "Dielectric Properties of Porcine Skin Tissue and In Vivo Testing of Implantable Antennas Using Pigs as Model Animals," *IEEE Antennas and Wireless Propagation Letters,* vol. 11, pp. 1686-1689, 2012.

[70] V.N. Tran & S.S. Stuchly, "Dielectric Properties of Beet, Beer Liver, Chicken and Salmon at Frequencies from 100 to 2500 MHz," *Journal of Microwave Power and Electromagnetic Energy,* vol. 22, no. 1, pp. 29-33, 1987.

[71] A. Rashidian, M. T. Aligodarz, and D. M. Klymyshyn, "Dielectric characterization of materials using a modified microstrip ring resonator technique," *IEEE Transactions on Dielectrics and Electrical Insulation,* vol. 19, no. 4, pp. 1392-1399, August 2012.

[72] M. Tlili, F. Deshours, G. Alquié, H. Kokabi, S. Hardinata, F. Koskas, "Microwave Resonant Sensor for Noninvasive Characterization of Biological Tissues," *IRBM,* vol. 39, no. 6, pp. 445-450, 2018.

[73] E. Alipoor, M.J. Hosseinzadeh-Attar, M. Rezaei, S. Jazayeri, & M. Chapman, "White adipose tissue browning in critical illness: A review of the evidence, mechanisms and future perspectives," *Obesity reviews : an official journal of the International Association for the Study of Obesity,* vol. 21, no. 12,e13085.

[74] C. Gabriel, S. Gabriel, and E. Corthout, "The dielectric properties of biological tissues: I. Literature survey," *Phys. Med. Biol.,* vol. 41, no. 11, p. 2231–2249, 1996.

[75] K. Sasaki, K. Wake, and S. Watanabe, "Measurement of the dielectric properties of the epidermis and dermis at frequencies from 0.5 GHz to 110 GHz," *Phys Med Biol,* vol. 59, no. 16, pp. 4739-4747, 2014.

[76] T. Lahtinen , J. Nuutinen,and E. Alanen, "Dielectric properties of the skin," *Phys Med Biol.,* vol. 42, no. 7, pp. 1471-1472, 1997.

[77] T.M. Cortázar, M. Guzmán-Alonso, H. Novoa, and M. Riaño, "Comparative study of temporary effect on the water content at different depths of the skin by hot and cold moisturizing formulations," *Skin Res Technol,* vol. 21, no. 3, pp. 265-271, 2015.

[78] Y. Feldman, A. Puzenko, P. Ben Ishai, A. Caduff, I. Davidovich, F. Sakran, AJ. Agranat, "The electromagnetic response of human skin in the millimetre and submillimetre wave range," *Phys Med Biol.,* vol. 54, no. 11, pp. 3341-3363, 2009.

[79] Z. A. Deneris, D. E. Pe'a, and C. M. Furse, "A Layered Pork Model for Subdermal Antenna Tests at 433 MHz," *IEEE Journal of Electromagnetics, RF and Microwaves in Medicine and Biology,* vol. 3, no. 3, pp. 171-176, Sept. 2019.

[80] S. Gabriel, R. Lau, and C. Gabriel, "The dielectric properties of biological tissues: II. Measurements on the frequency range 10 Hz to 20 GHz," *Phys. Med. Biol.,* vol. 41, no. 11, p. 2251–2269, 1996.

[81] M. M. Lowery, N. S. Stoykov, A. Taflove, and T. A. Kuiken, "A multiple-layer finite-element model of the surface EMG signal," *IEEE Transactions on Biomedical Engineering,* vol. 49, no. 5, pp. 446-454, May 2002.

[82] S. Cinti, "The adipose organ at a glance," *Dis Model Mech.,* vol. 5, no. 5, pp. 588-594, Sept. 2012.

[83] H.H. Hu, T.G. Perkins, J.M. Chia, V. Gilsanz, "Characterization of human brown adipose tissue by chemical-shift water-fat MRI," *AJR Am J Roentgenol,* vol. 200, no. 1, pp. 177-183, Jan. 2013.

[84] D.B. Rodrigues, P. R. Stauffer, E. Colebeck,A. Z. Hood, S. Salahi, P. F. Maccarini,and E. Topsakal, "Dielectric properties measurements of brown and white adipose tissue in rats from 0.5 to 10 GHz," *Biomed Phys Eng Express,* vol. 2, no. 2, 20162.

[85] F.M. Fisher, S. Kleiner,N. Douris, E. C. Fox, R. J. Mepani, F. Verdeguer ,J. Wu, A. Kharitonenkov , J. S. Flier, E. Maratos-Flier, and B. M. Spiegelman, "FGF21 regulates PGC-1α and browning of white adipose tissues in adaptive thermogenesis," *Genes Dev.,* vol. 26, no. 3, pp. 271-281, Feb. 2012.

[86] D. C. Garrett, B. A. Besler, J. Bourqui and E. C. Fear, "Estimating bulk dielectric properties of biological tissues at microwave frequencies," in *2016 17th International Symposium on Antenna Technology and Applied Electromagnetics (ANTEM)*, 2016.

[87] S.M. Jain, K. Pandey, A. Lahoti, and P.K. Rao, "Evaluation of skin and subcutaneous tissue thickness at insulin injection sites in Indian, insulin naïve, type-2 diabetic adult population," *Indian J Endocrinol Metab.,* vol. 17, no. 5, pp. 864-870, Sept. 2013.

[88] N. Tahan, et al., "Measurement of superficial and deep abdominal muscle thickness: an ultrasonography study," *Journal of physiological anthropology,* vol. 35, no. 1, 2016.

[89] L. Li, A. E. -C. Tan, K. Jhamb and K. Rambabu, "Buried Object Characterization Using Ultra-Wideband Ground Penetrating Radar," *IEEE Transactions on Microwave Theory and Techniques,* vol. 60, no. 8, pp. 2654-2664, Aug. 2012.

[90] M.R. Iqbal-Faruque, N. Aisyah-Husni, Md. Ikbal-Hossain, M. Tariqul-Islam, and N. Misran, "Effects of Mobile Phone Radiation onto Human Head with Variation of Holding Cheek and Tilt Positions," *Journal of Applied Research and Technology,* vol. 12, no. 5, pp. 871-876, 2014.

[91] W. D. Hurt, J. M. Ziriax and P. A. Mason, "Variability in EMF permittivity values: implications for SAR calculations," *IEEE Transactions on Biomedical Engineering,* vol. 47, no. 3, pp. 396-401, March 2000.

[92] B. Mohammed, J. Jin, A. M. Abbosh, K. S. Bialkowski, M. Manoufali and S. Crozier, "Evaluation of Children's Exposure to Electromagnetic Fields of Mobile Phones Using Age-Specific Head Models With Age-Dependent Dielectric Properties," *IEEE Access,* vol. 5, pp. 27345-27353, 2017.

[93] S. Kashyap, H. Zhang, K. Rao, and M. Sonka, "Learning-Based Cost Functions for 3-D and 4-D Multi-Surface Multi-Object Segmentation of Knee MRI: Data From the Osteoarthritis Initiative," *IEEE Transactions on Medical Imaging,* vol. 37, no. 5, pp. 1103-1113, May 2018.

[94] H. H. Nguyen, S. Saarakkala, M. B. Blaschko, and A. Tiulpin, "Semixup: In- and Out-of-Manifold Regularization for Deep Semi-Supervised Knee Osteoarthritis Severity Grading From Plain Radiographs," *IEEE Transactions on Medical Imaging,* vol. 39, no. 12, pp. 4346-4356, Dec. 2020.

[95] Y. Nasser, R. Jennane, A. Chetouani, E. Lespessailles, and M. E. Hassouni, "Discriminative Regularized Auto-Encoder for Early Detection of Knee OsteoArthritis: Data from the Osteoarthritis Initiative," *IEEE Transactions on Medical Imaging,* vol. 39, no. 9, pp. 2976-2984, Sept. 2020.

[96] M. J. Turunen, J. Töyräs, H. T. Kokkonen, and J. S. Jurvelin, "Quantitative Evaluation of Knee Subchondral Bone Mineral Density Using Cone Beam Computed Tomography," *IEEE Transactions on Medical Imaging,* vol. 34, no. 10, pp. 2186-2190, Oct. 2015.

[97] A. Al-Zaghal, C. Ayubcha, E. Kothekar, and A. Alavi, "Clinical Applications of Positron Emission Tomography in the Evaluation of Spine and Joint Disorders," *PET Clinics,* vol. 14, no. 1, pp. 61-69, 2019.

[98] A. Sorriento *et al*.,, "Design, Development and Validation of a Knee Brace to Standardize the US Imaging Evaluation of Knee Osteoarthritis," *IEEE Journal of Translational Engineering in Health and Medicine,* Vols. 10, Art no. 1800308, pp. 1-8, 2022.

[99] K. Sasaki, K. Wake, and S. Watanabe, "Measurement of the dielectric properties of the epidermis and dermis at frequencies from 0.5 GHz to 110 GHz," *Phys Med Biol,* vol. 59, no. 16, pp. 4739-4747, 2014.

[100] S. Gabriel, R. Lau, and C. Gabriel, "The dielectric properties of biological tissues: II. Measurements on the frequency range 10 Hz to 20 GHz," *Phys. Med. Biol.,* vol. 41, no. 11, p. 2251–2269, 1996.

[101] T.A Blackburn, and E. Craig, "Knee anatomy: a brief review," *Physical therapy,* vol. 60, no. 12, pp. 1556-1560, 1980.

[102] C. Gabriel., "Compilation of the Dielectric Properties of Body Tissues at RF and Microwave Frequencies," *Report N.AL/OE-TR- 1996-0037, Occupational and environmental health directorate, Radiofrequency Radiation Division, Brooks Air Force Base, Texas (USA),* 1996.

[103] Y. G. a. S. X. C. Liu, "Circularly Polarized Helical Antenna for ISM-Band Ingestible Capsule Endoscope Systems," *IEEE Transactions on Antennas and Propagation,* vol. 62, no. 12, pp. 6027-6039, Dec. 2014.

[104] D. Oloumi, P. Boulanger, A. Kordzadeh, & K. Rambabu, "Breast tumor detection using UWB circular-SAR tomographic microwave imaging," in *Annual International Conference of the IEEE Engineering in Medicine and Biology Society*, 2015.

[105] G. Jia and W. Chang, "Modified back projection reconstruction for circular FMCW SAR," in *2014 International Radar Conference*, 2014.

[106] J. van der Kruk *et al*., "GPR full-waveform inversion, recent developments, and future opportunities," in *2018 17th International Conference on Ground Penetrating Radar (GPR)*, Rapperswil, 2018.

[107] J. D. Redman, et al., "Field studies of GPR air launched surface reflectivity measurements of soil water content," in *Proceedings of the Society of Photo Optical Instrumentation Engineers (SPIE)*, 2002.

[108] L. Weihermüller, et al., "Mapping the spatial variation of soil water content at the field scale with different ground penetrating radar techniques," *Journal of Hydrology,* vol. 340, no. 3, pp. 205-216, 2007.

[109] L. Li, A. E. -C. Tan, K. Jhamb, and K. Rambabu, "Buried Object Characterization Using Ultra-Wideband Ground Penetrating Radar," *IEEE Transactions on Microwave Theory and Techniques,* vol. 60, no. 8, pp. 2654-2664, Aug. 2012.